

12-2016

Infrasound Propagation in Terrestrial Planetary Atmospheres

Lynsey B. Schroeder

Follow this and additional works at: <https://commons.erau.edu/edt>



Part of the [Atmospheric Sciences Commons](#), and the [Engineering Physics Commons](#)

This Thesis - Open Access is brought to you for free and open access by Scholarly Commons. It has been accepted for inclusion in PhD Dissertations and Master's Theses by an authorized administrator of Scholarly Commons. For more information, please contact commons@erau.edu.

INFRASOUND PROPAGATION IN TERRESTRIAL PLANETARY ATMOSPHERES

BY
LYNSEY B. SCHROEDER

A Thesis

Submitted to the Department of Physical Sciences
and the Committee on Graduate Studies
In partial fulfillment of the requirements
for the degree of
Master of Science in Engineering Physics

12/2016

Embry-Riddle Aeronautical University
Daytona Beach, Florida

© Copyright by Lynsey B. Schroeder 2016
All Rights Reserved

INFRA-SOUND PROPAGATION IN
TERRESTRIAL PLANETARY ATMOSPHERES

by

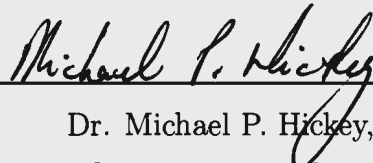
Lynsey B. Schroeder

This thesis was prepared under the direction of the candidate's Thesis Committee Chair, Dr. Jonathan B. Snively, Associate Professor of Engineering Physics, and Thesis Committee members Dr. Michael P. Hickey, Professor of Physics, Dr. Jeremy A. Rioussset, Assistant Professor of Engineering Physics, and Dr. Christopher J. Heale, Research Scientist, and has been approved by the Thesis Committee. It was submitted to the Department of Physical Sciences in partial fulfillment of the requirements of the degree of
Master of Science in Engineering Physics

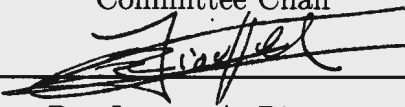
THESIS COMMITTEE:



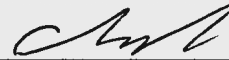
Dr. Jonathan B. Snively,
Committee Chair



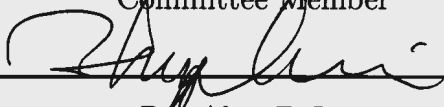
Dr. Michael P. Hickey,
Committee Member



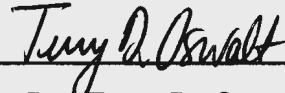
Dr. Jeremy A. Rioussset,
Committee Member



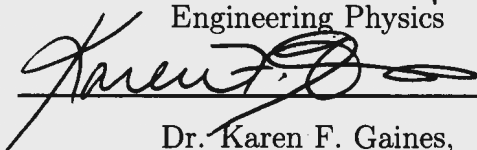
Dr. Christopher J. Heale,
Committee Member



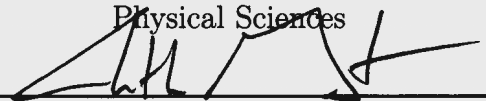
Dr. Alan Z. Liu,
Graduate Program Chair,
Engineering Physics



Dr. Terry D. Oswald,
Department Chair,
Physical Sciences



Dr. Karen F. Gaines,
Dean, College of Arts and Sciences



Dr. Christopher D. Grant,
Vice Chancellor, Academic Support

Abstract

Acoustic waves in the infrasonic frequency range, that is below 10 Hertz, have been observed to propagate to high altitudes in Earth's atmosphere. These waves have many sources, both natural and artificial, such as seismic events, convective storm systems, and nuclear explosions. Here, we seek to better understand the characteristics of atmospheric infrasound—below 0.1 Hz in particular—so as to improve the ability to detect their presence and sources. It is well-known that ambient attributes of an atmosphere, such as temperature, density, and composition, directly affect the propagation and growth of waves, and therefore it is likely that these dynamic phenomena are present (and may be detected) on other terrestrial planets with similar atmospheric structures.

Using a one-dimensional, nonlinear, compressible atmospheric acoustics model, this thesis seeks to investigate the propagation and dissipation of atmospheric acoustic waves in different terrestrial planetary atmospheres. The model, which includes gravity, molecular viscosity, and thermal conduction, has been developed using numerical solutions in Fortran, and is validated for the atmospheric conditions of Earth, Mars, and Venus. Empirical profiles for these planets are provided by the NASA Global Reference Atmospheric Model (GRAM) packages developed by Marshall Spaceflight Center. The terrestrial planets selected for investigation in this thesis exhibit similar atmospheric structures with very different temperatures, pressures, and compositions, which makes them ideal for a comparative study.

The model is used to determine the maximum achieved wave amplitude and propagation time to several altitudes of note as they vary with atmospheric conditions and

wave parameters; sensitivity to these parameters on the three planets under investigation are determined. Furthermore, by establishing these sensitivities we may identify conditions that are favorable for detection of infrasound in the upper atmospheres of Earth, Mars, and Venus.

By performing large model run sweeps of parameters such as latitude and longitude, time of day, and solar activity, we have drawn correlations between the atmospheric profile of each planet and the maximum achieved amplitude of propagating infrasound. The variations of temperature and gas composition due to ambient conditions directly affect damping of waves by viscosity and thermal conduction, and thus affect the growth of infrasonic wave packets. Venusian waves were found to be the most sensitive to ambient conditions, while waves on Earth were found to be the least sensitive. Results indicate that upward-propagating atmospheric acoustic waves are readily detectible from the middle and upper atmospheres of Earth and Venus, however those on Mars may only be detectible if they have energetic sources.

Acknowledgments

I am extremely grateful to my advisor, Dr. Jonathan Snively, for his continuing support and guidance during the last five years. Since my first semester at Embry-Riddle he has had an enormous impact on my academic and professional career. I would also like to thank my thesis committee, Dr. Mike Hickey, Dr. Jeremy Rioussset, and Dr. Chris Heale, for their support of my research and valuable feedback.

I would like to thank my alma mater, Embry-Riddle, for the amazing opportunities that I've had in my time as a student. Having completed my Bachelor's and Master's degrees, I am enormously proud to be forever an Eagle.

I would like to thank my parents, Yvette and Craig Johnson and Bill Schroeder, for always supporting me in my endeavors, inspiring me to do my best, and shaping me into the person who I am today, as well as my aunts, Michelle and Nicky, for being my second set of parents. I can't imagine my life without you. I would also like to thank Arth for his love and support, for always pushing me to do my best, and for reassuring me when I felt like I couldn't succeed.

Finally, I would like to thank Jason, Brett, and Lesley for their constant support of my educational endeavors, and for their leadership and guidance as I begin the next stage of my career.

This research was partially supported by the National Science Foundation under grant AGS-1151746 to Embry-Riddle Aeronautical University.

Contents

Abstract	iv
Acknowledgments	vi
List of Tables	ix
List of Figures	xiv
List of Symbols	xv
1 SCIENTIFIC BACKGROUND	1
1.1 Comparative Aeronomy of Terrestrial Planets	1
1.1.1 Hydrostatic Equilibrium	4
1.1.2 Stability of the Atmosphere	6
1.1.3 Thermal Structure of Atmospheric Regions	8
1.1.4 Planetary Profiles	14
1.2 Atmospheric Infrasound	17
1.2.1 Speed of Sound	18
1.2.2 Acoustic Attenuation	19
1.3 Review of Past Work	22
1.3.1 Sources of Infrasound	22
1.3.2 Planetary Infrasound	25
1.4 Problem Formulation	29
1.4.1 Organization of this Thesis	30

2	PHYSICAL AND MATHEMATICAL BASIS	31
2.1	The Euler Equations	31
2.2	Linear Dispersion Relation	32
2.3	Diffusion Equations	40
2.3.1	Viscosity	40
2.3.2	Thermal Conduction	41
2.4	Chapter Summary	42
3	MODEL DEVELOPMENT AND VALIDATION	43
3.1	Numerical Model	43
3.1.1	Lax-Wendroff Implementation	43
3.1.2	Euler Diffusion	47
3.1.3	Wave Forcing	51
3.2	Model Validation	51
3.2.1	Wavelength and Velocity	51
3.2.2	Attenuation	53
3.3	Ray-Tracing Model Predictions	55
3.4	Chapter Summary	57
4	INVESTIGATIONS OF PARAMETER EFFECTS	58
4.1	Variation of the Atmosphere	59
4.2	Variation of the Wave	78
4.3	Chapter Summary	82
5	SUMMARY AND SUGGESTIONS FOR FUTURE WORK	83
5.1	Wave Detectability	84
5.2	Potential Future Investigations	85
5.2.1	Further Model Development	86
5.3	Conclusions	87
	Bibliography	89
	Appendix A SIMULATION STRUCTURE	A-1

List of Tables

1.1	Planetary parameters at surface altitude [e.g., <i>Bougher et al.</i> , 2002; <i>Petculescu and Lueptow</i> , 2006].	4
4.1	Model input parameters for the diurnal variation run set.	61
4.2	Results of the time-of-day sweep.	64
4.3	Model input parameters for the geospatial run set.	65
4.4	Results of the latitude and longitude sweep.	70
4.5	Model input parameters for the solar sensitivity run set.	73
4.6	Results of the solar activity sweep.	74
4.7	Model input parameters for the random draw set.	76
4.8	Results of the random draw set.	77
4.9	Model input parameters for the frequency sweep.	79
4.10	Model input parameters for the amplitude sweep.	81

List of Figures

1.1	Not to scale. <i>Left:</i> Earth as photographed by the Apollo 17 mission. Obtained from the <i>National Aeronautics and Space Administration</i> [1972]. <i>Center:</i> Mars as photographed by the Hubble Space Telescope. Obtained from the <i>National Aeronautics and Space Administration</i> [2003]. <i>Right:</i> Venus as photographed by the Pioneer Venus Orbiter. Obtained from the <i>National Space Science Data Center</i> [1979].	2
1.2	Global mean profiles of temperature, density, and pressure on Earth, Mars, and Venus generated by NASA Marshall Spaceflight Center's EarthGRAM 2010, MarsGRAM 2010, and VenusGRAM 2005 [<i>Justh et al.</i> , 2006; <i>Leslie and Justus</i> , 2011; <i>Justh and Burns</i> , 2013].	3
1.3	Mean molecular weight of each atmosphere and main constituent species.	3
1.4	The specific gas constant, ratio of specific heats, and scale height. . .	5
1.5	Stability parameters for Earth, Mars, and Venus. Brunt-Väisälä frequency calculated from Equation (1.10) for a non-isothermal atmosphere.	8
1.6	Atmospheric layers of each of the three planets to be investigated, as defined by <i>Lissauer and de Pater</i> [2013, pp. 111]. Note that Mars' atmosphere is virtually isothermal so the layers are not as well-defined.	9
1.7	Diurnal variations of planetary thermosphere temperatures.	12
1.8	Diurnal variation of CO ₂ on Mars at 100 km and 200 km. Note the cyclical pattern that suggests that CO ₂ rises with dawn heating, falls in the afternoon, and then rises again in the evening, bringing with it warmer temperatures.	12

1.9	Exobase heights based on ratio of mean-free path and scale height for global mean profiles.	14
1.10	Frequency/period domains of different atmospheric waves. Obtained from <i>Blanc</i> [1985].	18
1.11	The speed of sound as it varies with altitude on Earth, Mars, and Venus.	19
1.12	Diffusion coefficients and Prandtl number for Earth, Mars, and Venus.	21
1.13	Acoustic attenuation coefficient (in Np/m) by frequency and altitude on Earth, Mars, and Venus.	22
1.14	Number of Google Scholar search results by year for publications containing the terms “atmosphere”, “infrasound”, “acoustic”, and “waves”, as well as those containing additionally “Mars” or “Venus”. Data were obtained October 2016, and this year’s number has been extrapolated to estimate total year results.	23
1.15	Nonlinear propagation of acoustic shock waves generated by a 4 kilotonne explosion. Obtained from <i>Besset and Blanc</i> [1994].	25
1.16	Validation of classical absorption in Martian acoustic waves. Obtained from <i>Hanford and Long</i> [2009].	27
1.17	Predictions of acoustic attenuation, obtained from <i>Petculescu and Lueptow</i> [2006]. Note that these results agree with those presented in Figure 1.13.	28
2.1	Procedure for determining the dispersion relation of a wave. Obtained from <i>Blackstock</i> [2000, pp. 299].	33
2.2	Density scaling factor versus altitude for Earth, Mars, and Venus. . .	35
2.3	Acoustic cut-off and Brunt-Väisälä periods on Earth, Mars, and Venus.	37
2.4	Diagnostic diagrams, as discussed by <i>Gossard and Hooke</i> [1975, pp. 113–118], illustrate the domains of acoustic and gravity waves based on the linear dispersion relation for $k_z = 0$ at ground-level (assuming the isothermal approximation).	38

2.5	Propagation of a continuously forced wave at the acoustic cut-off frequency (at ground) on Earth, Mars, and Venus. Note that the wave is nearly evanescent at low altitudes, consistent with propagation near the cut-off frequency, however it transitions away from evanescence at high altitudes as the cut-off frequency changes with speed of sound. The velocity amplitude is scaled with density via $(\rho_j/\rho_0)^{1/2}$	39
2.6	Propagation of a continuously forced wave with a period of 120s (0.0524 rad/s), a frequency firmly within the acoustic wave boundary of the diagnostic diagrams (Figure 2.4). Note that the wave shows vertical propagation through the domain, until dissipated or, on Earth, reflected at high altitudes. The velocity amplitude is scaled with density via $(\rho_j/\rho_0)^{1/2}$	39
3.1	Diagram depicting the two steps of the Lax-Wendroff method. Obtained from <i>Potter</i> [1973, pp. 68].	44
3.2	Validity of the Lax-Wendroff method on Earth, Mars, and Venus for several different time steps with a Δx of 500 meters and 1 kilometer, where green indicates stability and red indicates instability.	45
3.3	Model gravity validated against Newtonian gravity calculation.	46
3.4	Validity of the explicit Euler method on Earth, Mars, and Venus for several different time steps with a Δx of 500 meters and 1 kilometer, where green indicates stability and red indicates instability. Note that none of the values produce a valid CFL number on Mars and Venus to the desired simulation range of 200 kilometers.	48
3.5	Propagation of a sixty-second wave on Earth, using explicit diffusion and implicit diffusion. The results agree reasonably to 10^{-6} m/s. Note that the velocity amplitude is scaled with density via $(\rho_j/\rho_0)^{1/2}$, as discussed previously in Section 2.2.	50
3.6	One-minute period wave propagating upward over time on Earth, Mars, and Venus.	52

3.7	Wavelength validation for acoustic waves propagating horizontally at the surface of each planet.	53
3.8	Attenuation validation for an acoustic wave with a period of one minute propagating horizontally at 150 km on Earth. The coefficient of attenuation at this altitude is about $\alpha_c = 4.5 \times 10^{-7}$ Np/m.	54
3.9	Attenuation validation for an acoustic wave with a period of one minute propagating horizontally at 120 km on Mars. The coefficient of attenuation at this altitude is about $\alpha_c = 3.5 \times 10^{-6}$ Np/m.	54
3.10	Attenuation validation for an acoustic wave with a period of one minute propagating horizontally at 130 km on Venus. The coefficient of attenuation at this altitude is about $\alpha_c = 5.1 \times 10^{-7}$ Np/m.	55
3.11	The one-dimensional acoustics model is validated using the Runge-Kutta ray-tracing model.	57
4.1	Temperature variation at different times of day.	60
4.2	Atmospheric composition variation at different times of day.	60
4.3	Results of the time-of-day sweep for Earth.	63
4.4	Results of the time-of-day sweep for Mars.	63
4.5	Results of the time-of-day sweep for Venus.	64
4.6	Axial tilt of Earth, Mars, and Venus.	65
4.7	Temperature profiles at the equators and poles during the second month.	66
4.8	Variation of composition at the equators and poles during the second month.	66
4.9	Results of the latitude and longitude sweep for Earth.	69
4.10	Results of the latitude and longitude sweep for Mars.	69
4.11	Results of the latitude and longitude sweep for Venus.	70
4.12	Historical values for F10.7 emissions at 1 AU show high, low, and nominal values. Obtained from <i>NASA Goddard Spaceflight Center</i> [2016].	71

4.13	Variation of thermospheric temperature on Earth and Mars with solar activity. VenusGRAM 2005 does not account for solar effects, so Venus is excluded from this particular investigation.	72
4.14	Variation of composition on Earth and Mars at nominal, maximum, and minimum solar activity. Venus is excluded.	72
4.15	Results of the solar activity sweep for Earth.	75
4.16	Results of the solar activity sweep for Mars.	75
4.17	Distribution of maximum amplitude over a series of 250 random draws.	77
4.18	Distribution of time of arrival to 150 km over a series of 250 random draws.	78
4.19	Maximum wave amplitude on Earth, Mars, and Venus for a wide span of wave periods.	80
4.20	Maximum wave amplitude on Earth, Mars, and Venus for a wide span of source amplitudes.	82
5.1	Propagation of a sixty-second wave on each of the planets at night during nominal solar conditions, with source amplitudes selected to produce a wave around the hypothesized lower limit of detectability.	85
A.1	Command line output from building the model.	A-1
A.2	Model input file.	A-2
A.3	Example queue.csv file, which sets up a batch of 24 runs varying month and Local Standard Time. This batch does not specify any random draws.	A-3
A.4	Example model run, in which runs 4 and 5 from the <i>queueGlobe.csv</i> batch file are executed on Earth and output to a directory called <i>Example</i> . In this example terminal output is disabled with the <i>-q</i> flag.	A-5
A.5	Example model run, in which a wave is continuously forced for twenty seconds on Mars.	A-5
A.6	MATLAB [®] function loading data from the runs generated in Figure A.4. The output directory is specified along with the first and last runs and planet: 0 for Earth, 1 for Mars, and 2 for Venus.	A-6

List of Symbols

A	Diffusion matrix [-]
a	Amplitude [m/s]
a_{max}	Maximum amplitude [m/s]
a_0	Source amplitude [m/s]
c_p	Specific heat (constant pressure) [J/(kg·K)]
c_v	Specific heat (constant volume) [J/(kg·K)]
c_s	Speed of sound [m/s]
CFL	Courant-Friedrichs-Lewy stability condition [-]
d	Molecular diameter [m]
E	Energy density [J/m ³]
f	Frequency [Hz]
g	Acceleration due to gravity [m/s ²]
H	Scale height [m]
H_c	Heat flux [W/m ²]
i	The imaginary unit ($i^2 = -1$)
K	Diffusion constant [m ² /s]
k_x	Horizontal wave number [1/m]
k_z	Vertical wave number [1/m]
k_B	Boltzmann's constant [J/K]
ℓ	Mean-free path [m]

L_s	Celestial longitude angle of the sun from Mars [deg]
M	Molecular weight [kg/kmol]
n	Number density of particles [m ⁻³]
p	Pressure [Pa]
Pr	Prandtl Number [-]
Q	Heat density [J/m ³]
q	Parameter to be numerically calculated [-]
r	Radial distance [m]
R	Specific gas constant [J/(kg·K)]
R^*	Universal gas constant [J/(kmol·K)]
T	Temperature [K]
t	Time [s]
Δt	Temporal step size [s]
t_{center}	Gaussian wave packet center [s]
v	Wave velocity [m/s]
v_ϕ	Horizontal phase velocity [m/s]
v_r	Radial velocity [m/s]
v_x	Wave velocity in the horizontal direction [m/s]
v_z	Wave velocity in the vertical direction [m/s]
w	Enthalpy per unit mass [J/kg]
x	Horizontal distance [m]
Δx	Spatial step size in the horizontal direction [m]
z	Vertical distance (altitude) [m]
Δz	Spatial step size in the vertical direction [m]
α	Thermal diffusivity [m ² /s]
α_c	Classical absorption coefficient [Np/m]
δ	Unspecified heat sources and/or sinks [J/kg]

ϵ	Internal energy per unit mass [J/kg]
Γ	Temperature lapse rate [K/km]
Γ_d	Dry adiabatic lapse rate [K/km]
γ	Ratio of specific heats [-]
κ	Coefficient of thermal conduction [W/(m·K)]
λ	Wavelength [m]
μ	Coefficient of molecular viscosity [kg/(m·s)]
ν	Coefficient of kinematic viscosity [m ² /s]
ξ	Runge-Kutta coefficient [-]
θ	Potential temperature [K]
ρ	Mass density [kg/m ³]
σ	Gaussian wave packet width [s]
σ_x	Molecular cross-sectional area [m ²]
τ	Wave period [s]
τ_A	Acoustic cut-off period [s]
τ_N	Brunt-Väisälä period [s]
ω	Frequency [rad/s]
ω_o	Acoustic cut-off frequency [rad/s]
ω_N	Brunt-Väisälä frequency [rad/s]
χ	Some parameter (placeholder variable)
$\tilde{\chi}$	Small perturbation on some parameter
χ_0	Background value of some parameter

Chapter 1

SCIENTIFIC BACKGROUND

This chapter introduces topics to be considered in this thesis, acquainting the reader with the planets to be investigated and the physics of atmospheric infrasound. Additionally, a review of previous results will be presented in order to provide context to this work. While there has been significant study of infrasonic acoustic waves in Earth's atmosphere, few studies have been performed that compare infrasound propagation effects on other terrestrial planets. Chapter 1 concludes with a brief discussion of the goals of this thesis and outlines the organization of the remaining chapters.

Comparative plots throughout this thesis will be presented with **Earth in blue**, **Mars in red**, and **Venus in gold**, unless otherwise noted.

1.1 Comparative Aeronomy of Terrestrial Planets

The atmospheres of Venus, Earth, and Mars—the planets selected for investigation in this thesis—have undergone varying degrees of study in the last several decades. Each of these terrestrial planets possesses a similarly stratified atmosphere and layered thermal structure [e.g., *Taylor*, 2010, pp. 27], which makes them prime candidates for comparison, particularly due to the wide spectrum of atmospheric conditions seen from planet to planet. Table 1.1 describes atmospheric surface conditions for the three planets in question; Venus is hot and dense, while Mars is cold and sparse, and Earth is moderate by both metrics [e.g., *Prinn and Fegley*, 1987]. Furthermore, the

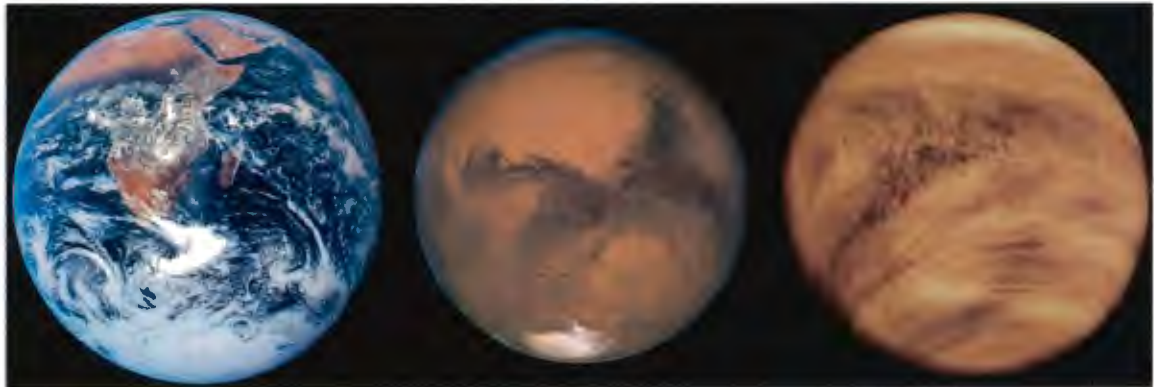


Figure 1.1: Not to scale.

Left: Earth as photographed by the Apollo 17 mission. Obtained from the *National Aeronautics and Space Administration* [1972].

Center: Mars as photographed by the Hubble Space Telescope. Obtained from the *National Aeronautics and Space Administration* [2003].

Right: Venus as photographed by the Pioneer Venus Orbiter. Obtained from the *National Space Science Data Center* [1979].

gaseous compositions of Venus and Mars are much different than Earth, raising several questions about how well their atmospheres support the propagation of compressional waves [Hanford and Long, 2009].

While a tabulation of surface parameters provides insight into the basic characteristics of each atmosphere, there is significant variation with altitude that cannot be neglected. Figure 1.2 shows temperature, density, and pressure as they vary with altitude on each planet, related by the ideal gas equation of state [e.g., Salby, 1996, p. 5; Lissauer and de Pater, 2013, p. 69]:

$$p = \rho RT \tag{1.1}$$

where p is the atmospheric pressure in Pascals, ρ is the mean air density in kilograms per cubic meter, R is the specific gas constant ($R = \frac{R^*}{M}$), and T is the air temperature in Kelvin. Figure 1.3 shows the mean molecular weight in each planet's atmosphere relative to those of the major gases present in order to illustrate the transition between different species with altitude.

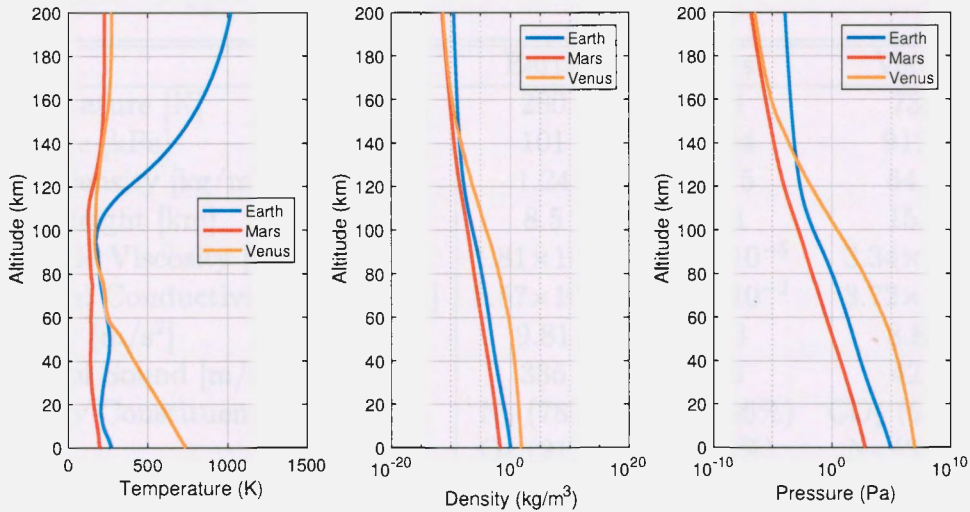


Figure 1.2: Global mean profiles of temperature, density, and pressure on Earth, Mars, and Venus generated by NASA Marshall Spaceflight Center’s EarthGRAM 2010, MarsGRAM 2010, and VenusGRAM 2005 [Justh et al., 2006; Leslie and Justus, 2011; Justh and Burns, 2013].

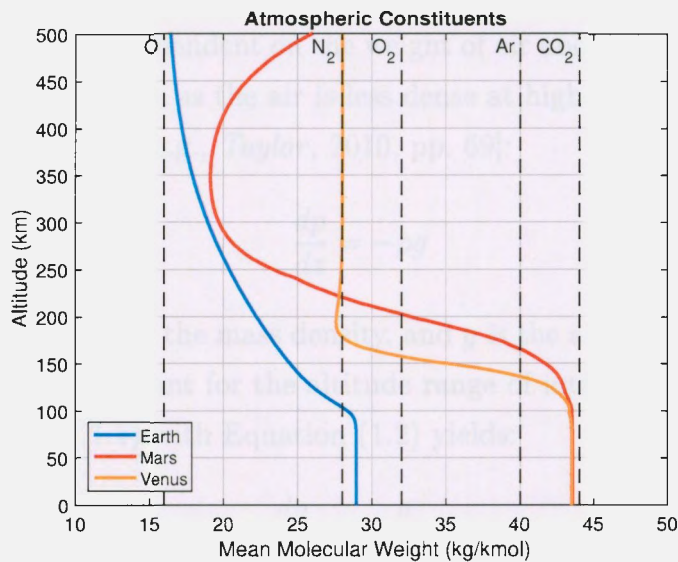


Figure 1.3: Mean molecular weight of each atmosphere and main constituent species.

Table 1.1: Planetary parameters at surface altitude [e.g., *Bougher et al.*, 2002; *Petculescu and Lueptow*, 2006].

	Earth	Mars	Venus
Temperature [K]	280	208	735
Pressure [kPa]	101	0.594	9120
Mass Density [kg/m ³]	1.24	0.015	64.8
Scale Height [km]	8.5	11.1	15.9
Dynamic Viscosity [kg/(m·s)]	1.81×10^{-5}	1.08×10^{-5}	3.34×10^{-5}
Thermal Conductivity [W/(m·K)]	2.57×10^{-2}	1.21×10^{-2}	3.72×10^{-2}
Gravity [m/s ²]	9.81	3.73	8.88
Speed of Sound [m/s]	336	246	427
Primary Constituents	N ₂ (78%)	CO ₂ (96%)	CO ₂ (96.5%)
	O ₂ (21%)	N ₂ (2%)	N ₂ (3.5%)
	Ar (<1%)	Ar (2%)	CO (<1%)

1.1.1 Hydrostatic Equilibrium

A planet's atmospheric mass is, by definition, vertically stratified due to the compressibility of air [e.g., *Salby*, 1996, pp. 2]. Gases in the atmosphere are generally modeled with consideration of hydrostatic equilibrium, which assumes the system to be a “fluid at rest,” as described by *Jacobson* [2005, pp. 12]. This suggests that atmospheric pressure is solely dependent on the weight of air above, meaning that pressure also decreases with altitude, as the air is less dense at higher altitudes. This relation is given by the expression [e.g., *Taylor*, 2010, pp. 69]:

$$\frac{dp}{dz} = -\rho g \quad (1.2)$$

where p is the pressure, ρ is the mass density, and g is the acceleration due to gravity. Note that g is nearly constant for the altitude range of interest to this investigation. Combining Equation (1.1) with Equation (1.2) yields:

$$\frac{dp}{dz} = -\frac{g}{RT}p \quad (1.3)$$

and the atmospheric pressure scale height may be defined as [e.g., *Salby*, 1996, pp. 9]:

$$H = \frac{RT}{g} = \frac{c_s^2}{\gamma g} \quad (1.4)$$

where γ is the ratio of specific heats: $\gamma = c_p/c_v$ [e.g., *Salby*, 1996, pp. 68]. This quantitatively describes atmospheric stratification and how atmospheric pressure and density decrease with altitude. Naturally, this varies with altitude due to changes in temperature and species density fractions. It essentially measures the “thickness” of the atmosphere by describing the distance over which the pressure/density of the atmosphere changes by a factor of e^{-1} (as a function of temperature) [e.g., *Kalkofen et al.*, 1994]. From Equations (1.3) and (1.4) we obtain the constitutive relation:

$$\frac{dp}{dz} = -\frac{p}{H}$$

which, when separated and integrated, yields the hydrostatic pressure equation for an isothermal atmosphere [e.g., *Lissauer and de Pater*, 2013, pp. 69]:

$$p(z) = p_0 e^{-z/H} \quad (1.5)$$

Both pressure and density may be modeled as exponential decay, via Equation (1.5), in an ideally isothermal, compressible atmosphere, such that H remains constant.

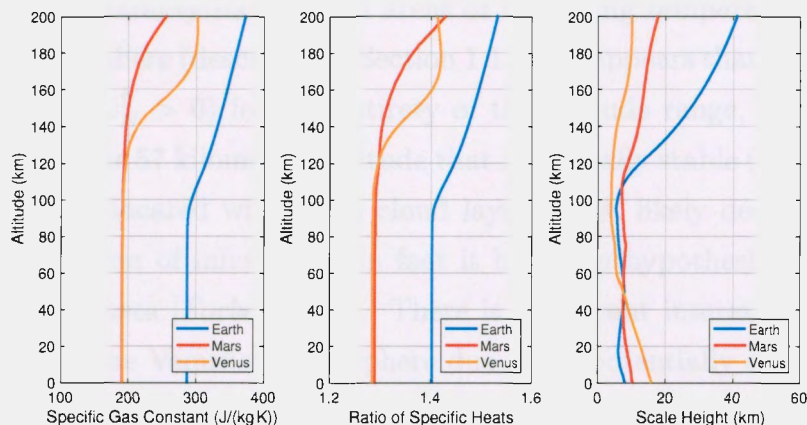


Figure 1.4: The specific gas constant, ratio of specific heats, and scale height.

1.1.2 Stability of the Atmosphere

Because the atmosphere is assumed to be in hydrostatic equilibrium, the stratification is directly related to the thermal structure; this is why atmospheric layers may be defined by changes in temperature gradient [Salby, 1996, pp. 16] as shown later in Figure 1.6. We define the environmental temperature lapse rate:

$$\Gamma = -\frac{dT}{dz} \quad (1.6)$$

which describes the gradient of temperature, and the dry adiabatic lapse rate:

$$\Gamma_d = -\frac{dT'}{dz'} = \frac{g}{c_p} \quad (1.7)$$

which describes the temperature gradient for a single air parcel during adiabatic displacement [Salby, 1996, pp. 74]. The relationship of these quantities is used to assess the static stability of a stratified atmosphere, where:

$$\Gamma \begin{cases} < \Gamma_d & \text{Stable} \\ = \Gamma_d & \text{Neutrally Stable} \\ > \Gamma_d & \text{Unstable} \end{cases}$$

Figure 1.5 plots these quantities and confirms that each atmosphere is hydrostatically stable. Note that stability increases in areas of increasing temperature, such as the base of the thermosphere (described in Section 1.1.3). It appears that each atmosphere is stable ($\Gamma < \Gamma_d$, $\omega_N^2 > 0$) for the entirety of the altitude range, aside from a few meters on Venus near 57 kilometers altitude that is neutrally stable ($\Gamma = \Gamma_d$, $\omega_N^2 = 0$). This small region—located within the cloud layer—most likely does not negatively affect the propagation of infrasound; in fact it has been hypothesized as a possible source of gravity waves [Forbes, 2002]. There is significant interest in studying the unstable region of the Venusian atmosphere due to its potentially significant impact on convective processes, such as the formation of Venus' thick CO₂ clouds [Bullock and Grinspoon, 2013].

Another important parameter and measure of stability, the potential temperature,

describes the temperature that an air parcel would reach if it were moved adiabatically from its altitude to a reference point, usually the ground. The first law of thermodynamics for adiabatic processes [Jacobson, 2005, pp. 50] describes the relation:

$$\frac{dT}{T} = \left(\frac{R}{c_p}\right) \frac{dp}{p}$$

Integrating from T , the temperature at the starting location, to θ , the potential temperature, and from p , the pressure at the starting location, to p_0 , the reference pressure, this expression yields [e.g., Salby, 1996, pp. 71]:

$$\theta = T \left(\frac{p_0}{p}\right)^{R/c_p} \quad (1.8)$$

The change in potential temperature may also be used to assess the stability of the atmosphere, and is related to the lapse rate as such:

$$\frac{d\theta}{dz} = \frac{\theta}{T}(\Gamma_d - \Gamma) \quad (1.9)$$

We thus expect that for a neutrally buoyant atmosphere (i.e., the environmental lapse rate equals the dry adiabatic lapse rate, as discussed previously) the potential temperature will be constant.

Following from potential temperature, we define the Brunt-Väisälä (buoyancy) frequency—another measure of stratification and stability in the atmosphere—given by [e.g., Jacobson, 2005, pp. 57]:

$$\omega_N^2 = \frac{g}{\theta} \frac{d\theta}{dz} = \frac{g}{T}(\Gamma_d - \Gamma) \quad (1.10)$$

which represents the frequency of vertical oscillation of a fluid parcel about its equilibrium level of buoyancy [Salby, 1996, pp. 175]. Stability is also defined by:

$$\omega_N^2 \begin{cases} > 0 & \text{Stable} \\ = 0 & \text{Neutrally Stable} \\ < 0 & \text{Unstable} \end{cases}$$

Figure 1.5 confirms stability via this parameter as well.

For an ideally isothermal, compressible atmosphere, the Brunt-Väisälä frequency may be approximated to [e.g., *de Larquier, 2010*]:

$$\omega_N \simeq \frac{g}{c_s} \sqrt{\gamma - 1} \quad (1.11)$$

The Brunt-Väisälä frequency is discussed further in Chapter 2, as it represents a significant boundary between regimes for propagating atmospheric waves, where waves with frequencies lower than ω_N are dominated by buoyant effects (gravity waves).

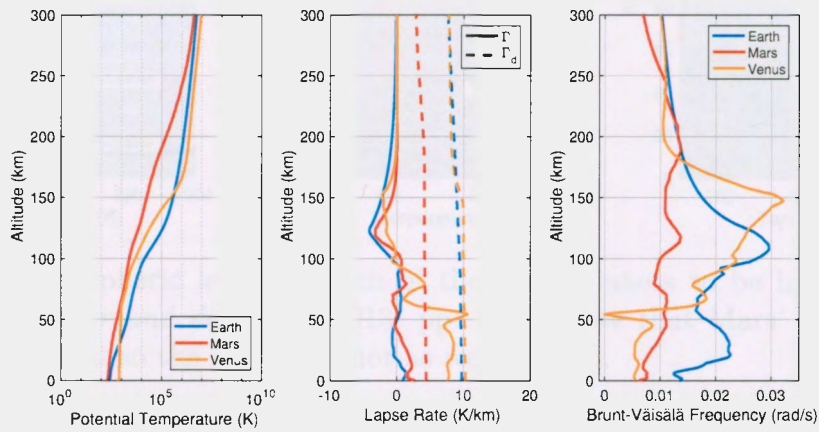


Figure 1.5: Stability parameters for Earth, Mars, and Venus. Brunt-Väisälä frequency calculated from Equation (1.10) for a non-isothermal atmosphere.

1.1.3 Thermal Structure of Atmospheric Regions

A planet's thermal structure, dT/dz , is primarily defined by its gravity, pressure, and energy transport. Energy sources and sinks such as solar heating, chemical processes, and cloud and weather layers are responsible for the defined stratified layers that make up the thermal structure [e.g., *Lissauer and de Pater, 2013, pp. 111*].

Most stratified atmospheres contain three or four main layers, the troposphere, stratosphere (not present on all terrestrial planets), mesosphere, and thermosphere, as defined by the variation of temperature with altitude. While chemical composition and energy transport processes vary drastically from planet to planet, the thermal

structure for many worlds is qualitatively similar. Most planetary thermal regions are analogous to one another, allowing for the universal application of the terms originally used to identify regions in our own atmosphere [Mueller-Wodarg *et al.*, 2008].

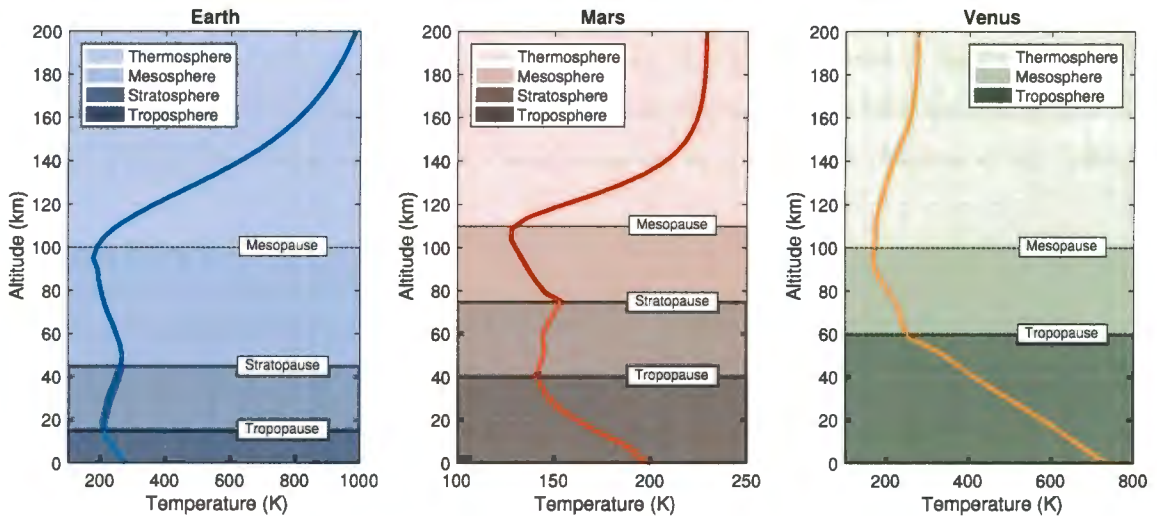


Figure 1.6: Atmospheric layers of each of the three planets to be investigated, as defined by *Lissauer and de Pater* [2013, pp. 111]. Note that Mars’ atmosphere is virtually isothermal so the layers are not as well-defined.

Troposphere

The troposphere of a planet is its lowest region, extending from ground to the lower or middle atmosphere. A planet’s troposphere is characterized by a region of steady cooling that varies in gradient magnitude from 2 K/km on Mars to 8 K/km on Venus (with Earth in between); nonetheless, these are all extremely gradual [Strobel, 2002]. As the closest region to the surface, the troposphere is the densest region of the atmosphere, containing 90% or more of the atmosphere by mass [e.g., Nave, 2008; Salby, 1996, pp. 9]. This region is also home to extremely variable convective weather processes and winds, particularly on Earth, and the majority of a planet’s cloud cover.

Stratosphere

The stratosphere is a region of gradual heating in the lower-middle atmosphere of some planets due to changes in chemical composition at these altitudes and the absorption of heat (solar energy) by these species; for example, Earth's stratosphere is characterized by the introduction of ozone. Furthermore, the stratosphere is characterized by an increase in stability as the environmental temperature lapse rate decreases and the Brunt-Väisälä frequency increases, clearly shown in Figure 1.5 [Holton *et al.*, 1995].

Mesosphere

Above the stratosphere is the mesosphere, in which the temperature continues to fall with altitude. The density in the mesosphere is considerably lower than the layer(s) below, and is generally home to the planet's coldest temperatures near the mesopause—the transition from the upper-mesosphere to the lower-thermosphere. Defined as the middle-upper atmosphere, the mesosphere indicates the beginning of significant changes in constituent species (such as the appearance of atomic oxygen), as seen earlier in Figure 1.3, contributing to heating and cooling processes [Strobel, 2002]. It is also where propagating acoustic and gravity waves forced from the troposphere begin to grow to prominent amplitude such that they may be observed [e.g., Fritts and Alexander, 2003; Medvedev and Yiğit, 2012].

Thermosphere

At the top of the atmosphere is a rarified region called the thermosphere, where temperature increases with altitude. Solar heating is primarily responsible for this temperature increase, which varies from rapid growth on the order of 10-20 K/km on Earth to the gradual heating of the Martian and Venusian thermospheres [Strobel, 2002]. At the topside of the thermosphere, temperatures generally approach an asymptotic value, where the atmosphere remains nearly isothermal until the density becomes excessively tenuous (i.e., the transition to the exosphere, to be discussed in the next section). The top of the thermosphere serves as the diffuse boundary between the atmosphere and the exosphere—the region of outer space encircling the

planet [e.g., *Bougher et al.*, 2002]. Thermospheric temperatures of terrestrial planets tend to reach, if not exceed, surface temperatures. The exception to this rule would be the case of Venus, the surface temperature of which cannot be attained other than by its drastic greenhouse effect found at low-altitudes. Venus' dayside thermosphere achieves temperatures of 300-400 K, while the nightside thermosphere is the coldest region of the planet, reaching temperatures of only 100 K, often leading to the region to be called a *cryosphere* rather than a thermosphere [*Pätzold et al.*, 2007].

Due to its relatively low density (thus inability to retain heat) and greater sensitivity to the impacts of solar radiation, the thermosphere sees a great difference in temperature between day and night. Figure 1.7 depicts the diurnal variations of the planets' thermospheric temperatures for four key times: night (0:00 Local Solar Time), dawn (6:00 Local Solar Time), day (12:00 Local Solar Time), and dusk (18:00 Local Solar Time). The results, for the most part, follow expectations, with the coolest temperatures at night and dawn and the warmest temperatures at high-noon and dusk. However the exception is that on Mars and Venus we see warmer temperatures at dawn—on Mars even more so than during the day. One theory to explain this could be that the heating of the atmosphere with sunrise causes heavy CO₂ to rise from lower, cooler altitudes [*Bougher et al.*, 2002], bringing down the average temperature of the thermosphere and leading to a cyclical temperature. Figure 1.8 shows the density of CO₂ over time as it rises and falls—the highest densities of CO₂ in the upper-thermosphere exactly coincide with the warmest temperatures, with the hottest at 6:00, second at 18:00, third at 12:00, and coldest at 0:00.

The Venusian thermosphere shows the greatest sensitivity to time of day; this is likely due to its long diurnal cycle. A day on Venus is equal to roughly 243 Earth days [e.g., *Williams*, 2016] so the nightside of the planet spends significantly more time facing away from the sun than it does on other planets (for reference, a Martian day is roughly 24.5 Earth hours), which allows for longer periods of cooling.

The thermosphere is also coupled with the planet's ionosphere, due to the ionization effects of the solar heating and neutral drag on the ions. However this thesis focuses on dynamics of the neutral atmosphere, and will not discuss the ionized species present at high altitudes.

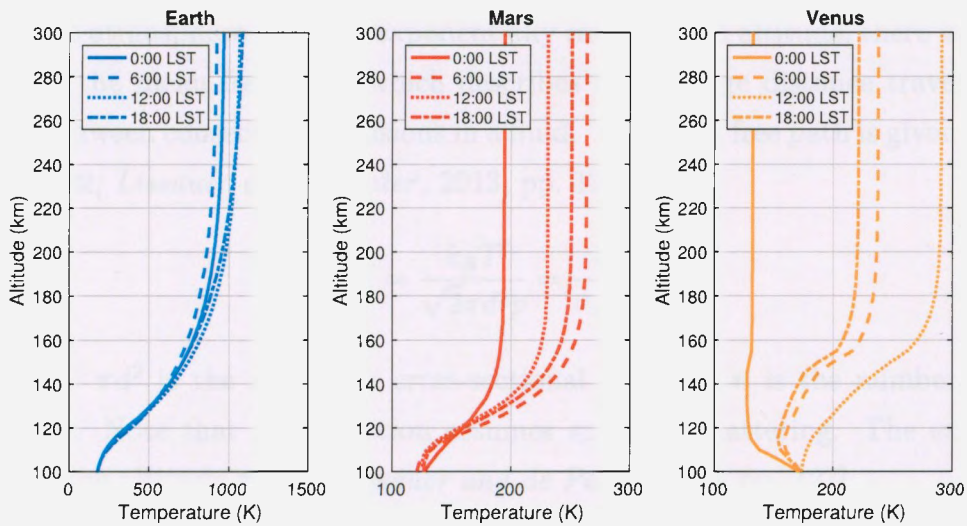


Figure 1.7: Diurnal variations of planetary thermosphere temperatures.

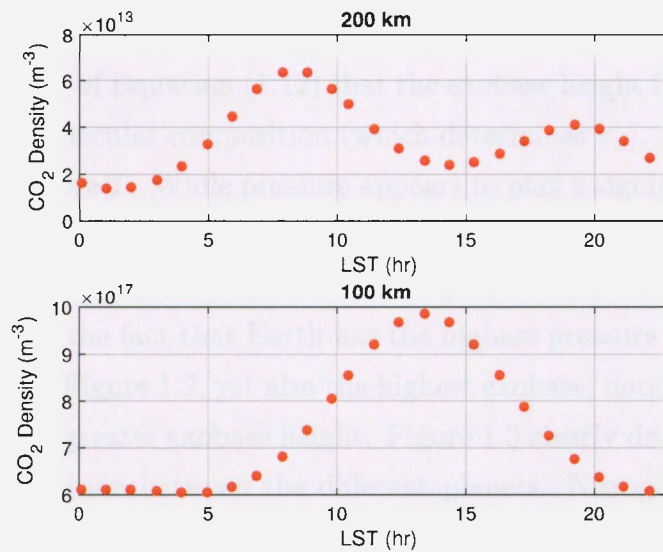


Figure 1.8: Diurnal variation of CO_2 on Mars at 100 km and 200 km. Note the cyclical pattern that suggests that CO_2 rises with dawn heating, falls in the afternoon, and then rises again in the evening, bringing with it warmer temperatures.

Exobase Height

Because the atmosphere becomes exponentially rarified with altitude, there is a direct increase of the mean free path, which describes the average distance traveled by a molecule between consecutive collisions in a fluid. The mean free path is given by [e.g., *Strobel*, 2002; *Lissauer and de Pater*, 2013, pp. 127]:

$$\ell = \frac{k_B T}{\sqrt{2} \pi d^2 p} = \frac{1}{\sigma_x n} \quad (1.12)$$

where $\sigma_x = \pi d^2$ is the molecular cross-sectional area and n is the number density of particles. Note that this equation assumes spherical scattering. The exobase is located at the altitude where [*Lissauer and de Pater*, 2013, pp. 127]:

$$\int_{z_{ex}}^{\infty} \sigma_x n(z) dz \approx \sigma_x n(z_{ex}) H = 1 \quad (1.13)$$

The altitude at which this ratio is unity is essentially the point where the atmosphere becomes quasi-collisionless, and, thus, the border between atmosphere and outer space [*Strobel*, 2002]. This parameter is plotted for each planet in Figure 1.9. It is clear by inspection of Equation (1.12) that the exobase height is most dependent on the atmosphere's molecular composition (which determines σ_x), pressure p , and thermospheric temperature T . While pressure appears to play a significant role in exobase height (not surprising due to the fact that pressure is due to molecular collisions), the majority of dependency actually falls on the temperature and composition. This may be confirmed due to the fact that Earth has the highest pressure at high altitudes, as shown previously in Figure 1.2, yet also the highest exobase; note that higher temperature also leads to a greater exobase height. Figure 1.3 clearly depicts the variation in atmospheric composition between the different planets. Nitrogen-rich atmospheres, such as Earth or Titan (not discussed in this thesis), have high exobase heights due to their much lower mean molecular weight, which becomes especially relevant with the transition to lighter atomic oxygen at high altitudes. Conversely, carbon-dioxide-based atmospheres, such as Venus and Mars, have lower exobase heights due to the fact that their heavier atmospheres are condensed closer to the surface [*Strobel*, 2002].

It is worth mentioning that these values are variable with solar activity and time of day, as heating by the sun has significant effects on the chemistry of the upper-atmosphere, as discussed previously, thus altering the energy and therefore frequency of collisions. The heights shown in Figure 1.9 are calculated via the profiles used throughout this thesis, which use standard, default values for solar activity.

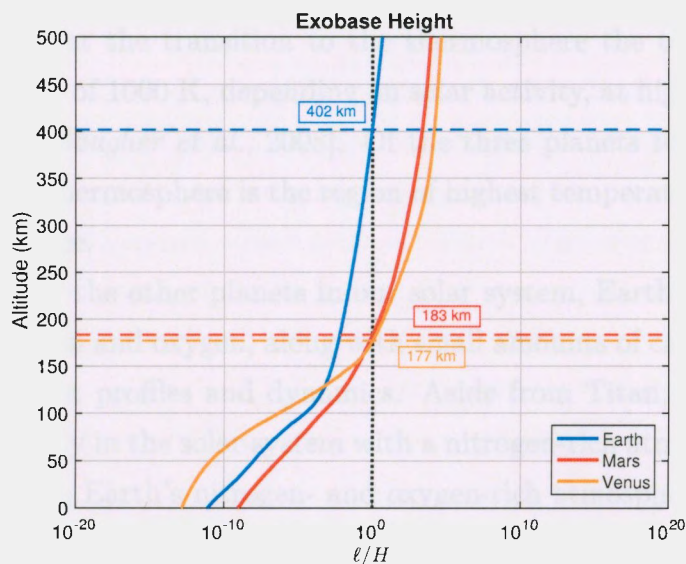


Figure 1.9: Exobase heights based on ratio of mean-free path and scale height for global mean profiles.

1.1.4 Planetary Profiles

Earth

Earth’s atmosphere consists of distinct regions in which the temperature and constituents vary with altitude. Surface conditions, as shown in Table 1.1, are median for the selected planets, with temperature around 300 Kelvin and pressure at 10^5 Pascals (the definition of an “atmosphere”—1 atm—in terms of units of pressure). Below about 100 kilometers (the mesopause), the atmosphere is dominated by nitrogen and oxygen, with these beginning to taper off at higher altitudes to be replaced by atomic oxygen, as shown in Figure 1.3. Furthermore, the drop in both density and pressure

becomes steeper at the mesopause, and there is a significant change in temperature where thermospheric warming goes into effect. Until the mesopause (around 100 km), the temperature hovers between 200 and 300 K with increases and decreases throughout the different regions but remaining more or less consistent. The region below 100 km is aptly named the *homosphere*, as the atmosphere is well-mixed and essentially isothermal, and may be approximated as such with reasonable accuracy for many purposes. However at the transition to the thermosphere the temperature rapidly increases to upwards of 1000 K, depending on solar activity, at high altitudes, as seen in Figure 1.2 [e.g., *Bougher et al.*, 2008]. Of the three planets to be investigated in this thesis, Earth's thermosphere is the region of highest temperature, exceeding even that at Venus' surface.

In comparison to the other planets in our solar system, Earth is unique. Its high abundance of nitrogen and oxygen, along with small amounts of carbon-dioxide, leads to extremely different profiles and dynamics. Aside from Titan, a moon of Saturn, Earth is the only body in the solar system with a nitrogen-rich atmosphere. As can be seen from Figure 1.1, Earth's nitrogen- and oxygen-rich atmosphere gives the planet a deep marble blue color, as opposed to the hues of red, orange, and yellow of Mars and Venus. Of course Earth is also unique in that its atmosphere has the ability to support life due to its mild temperature, which allows for liquid water at the surface. The troposphere of Earth is home to highly variable, localized weather processes, such as liquid water rain storms, and winds that vary due to geographical location.

Mars

The Martian atmosphere is largely composed of carbon dioxide (95%), along with nitrogen, argon, and oxygen. Unlike Earth, the atmospheric constituents remain relatively consistent in their ratios with increasing altitudes, and the temperature profile is essentially isothermal, with temperatures varying only by about 100 K. As shown in Table 1.1, the surface temperature is much colder than that of Earth, and Mars' atmosphere is significantly less dense than Earth's (only 12% density) throughout, with a lower pressure as a result (about 7%). While Mars is incredibly dry, the low temperatures allow the small amount of water vapor to nearly saturate

the air, and clouds do occur [Taylor, 2010, pp. 15]. The presence of weather systems on Mars is essentially limited to massive dust storms, which engulf the planet on global scales; these storms occur relatively infrequently, generally at perihelion every two (Earth) years, and last for a few (Earth) months. These storms are caused by solar heating, which imparts energy to the air and lifts dust off the ground; they drastically affect atmospheric dynamics and the planet's meteorological conditions [Coffey, 2008].

Mars' atmosphere may be divided into three regions: the warm lower atmosphere, a cooler mesosphere, and a thermosphere with some slight heating. Unlike on Earth, there is no ozone present in the atmosphere to produce stratospheric heating. However there is a strong presence of dust in the upper-troposphere that causes Martian stratospheric heating [González-Galindo *et al.*, 2008]. The thermospheric heating is also much weaker than that of Earth, falling just shy of surface temperature at its maximum. The quasi-isothermal profile of Mars is due in part to the high thermal conduction in its atmosphere, which is responsible for suppressing temperature gradients. Its warm surface is due to a small greenhouse effect by its carbon-dioxide composition, however due to its thin atmosphere this effect is minimal, thus contributing to its nearly isothermal nature.

Venus

Often called the Earth's sister, Venus is similar in size and geology, however its atmosphere is drastically different. Perhaps more like Mars than Earth, its composition is 93-97% carbon dioxide, 2-5% nitrogen, and about 1% sulfur dioxide, atomic oxygen, carbon monoxide, and other gases [e.g., Prinn and Fegley, 1987; Mueller-Wodarg *et al.*, 2008]. The surface of Venus is characterized by a temperature of 730 Kelvin and a pressure of 90 atm, which makes it an ideal example of a high pressure atmosphere for validation of the model [e.g., Fjeldbo *et al.*, 1971]. Perhaps the best known feature of Venus is its thick sulfuric acid cloud layer, which is completely impenetrable in the visible spectrum. This cloud cover paired with its carbon dioxide atmosphere results in a runaway greenhouse effect that contributes upwards of 500 Kelvin to its surface temperature [Taylor, 2010, pp. 11].

Venus is of particular interest due to the fact that its atmosphere is essentially

broken into two very different regions: below the clouds and above the clouds. Below an altitude of about 100 km, the point at which the clouds have completely subsided, the atmosphere is incredibly hot and dense. The Venusian troposphere contains 99% of its atmosphere by mass, with 90% found below 30 km. At the surface, temperatures exceed the melting point of many metals, which, paired with the extreme pressures one hundred times greater than the surface of Earth, has made it incredibly difficult to land spacecraft [Nave, 2008]. The composition of Venus changes drastically above 100-150 km as well, as seen in Figure 1.3, with nitrogen abundance surpassing that of carbon dioxide above the clouds. While the troposphere is incredibly hot at the surface, the temperature has decreased by 500 K by tropopause altitudes at 60 km, with temperatures continuing to drop, albeit more slowly, in the mesosphere. Above 100 km, the Venusian thermosphere, there is a slight warming effect, however by this point temperatures have reached nearly Martian levels of 200-300 K—colder than the surface of the Earth, and much colder than the Earth’s thermosphere. Density and pressure also make a dramatic drop above the cloud layer; these profiles, shown in Figure 1.2, are by far the steepest and least consistent of the three planets being studied. There has also been discussion of the possibility of intracloud lightning on Venus [Fischer *et al.*, 2011], which is especially interesting as a potential source of acoustic waves.

1.2 Atmospheric Infrasonic

Periodic disturbances in the atmosphere at frequencies greater than the acoustic cut-off frequency produce short-period acoustic waves that move through the upper-atmosphere. These waves cause large compressions in the atmosphere at infrasonic (< 10 Hz) frequencies as they propagate upward, grow in amplitude, and eventually dissipate at high altitudes [e.g., Drob *et al.*, 2003].

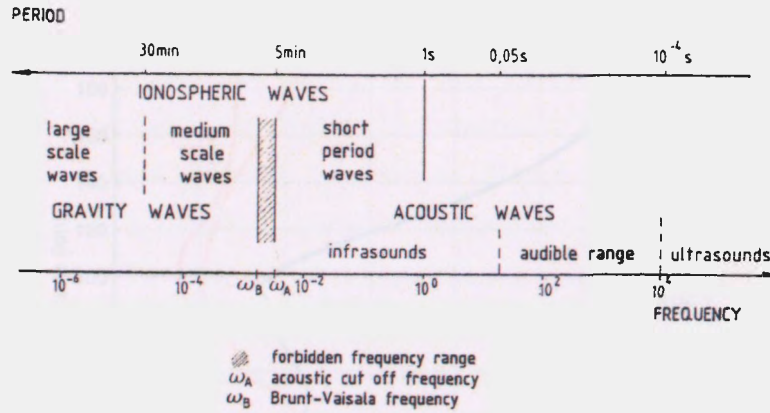


Figure 1.10: Frequency/period domains of different atmospheric waves. Obtained from *Blanc* [1985].

1.2.1 Speed of Sound

The propagation and dissipation of infrasonic acoustic waves is directly related to atmospheric properties, such as temperature, density, pressure, viscosity, etc. that affect major parameters, such as the speed of sound: the speed at which sound can travel through a specific medium, given by [e.g., *Kinsler et al.*, 2000, pp. 121]:

$$c_s^2 = \gamma RT = \gamma \frac{p}{\rho} \quad (1.14)$$

where γ is the ratio of specific heats, R is the specific gas constant, and T is the ambient temperature in Kelvin. These three parameters all vary with altitude, which indicates that acoustic waves move through varying speeds of sound as they propagate upward, determining their velocities, refraction or reflection, and eventual dissipation. Figure 1.11 depicts the speed of sound on the three planets of interest as it varies with atmosphere; note that it has essentially the same shape as the variation of temperature, as γ and R are more or less constant with altitude.

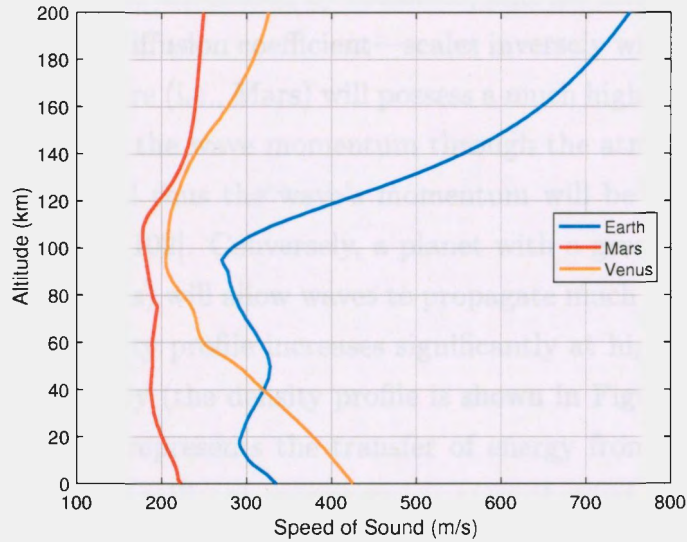


Figure 1.11: The speed of sound as it varies with altitude on Earth, Mars, and Venus.

1.2.2 Acoustic Attenuation

As acoustic waves travel through the atmosphere they are damped by two dominant diffusion processes: viscosity and thermal conduction. While dynamic viscosity and thermal conductivity are properties of the gases that make up the atmosphere, the diffusive terms, kinematic viscosity (also called molecular diffusivity) and thermal diffusivity, vary with altitude due to changes in density. These are given, respectively, by:

$$\nu = \frac{\mu}{\rho} \quad (1.15)$$

where μ is the dynamic viscosity, which varies with temperature, and:

$$\alpha = \frac{\kappa}{\rho c_p} \quad (1.16)$$

where κ is the thermal conductivity, which is based essentially on molecular composition of the atmosphere. Note that the model used in this thesis assumes constant μ and κ with altitude; the variation of μ is minimal and the variation of κ is gradual and smooth, thus it is reasonable to neglect derivative terms.

Viscous effects in a gas are caused by collisions, and the kinematic viscosity—also known as the molecular diffusion coefficient—scales inversely with density. Therefore, a more tenuous atmosphere (i.e., Mars) will possess a much higher kinematic viscosity, as collisions to transport the wave momentum through the atmosphere will be fewer and farther between, and thus the wave’s momentum will be diffused quickly [e.g., *Jacobson*, 2005, pp. 101–102]. Conversely, a planet with a greater neutral density in its atmosphere (i.e., Venus) will allow waves to propagate much farther. This explains why the Venusian viscosity profile increases significantly at high altitudes, where its density drops considerably (the density profile is shown in Figure 1.2).

Thermal conduction represents the transfer of energy from one molecule to the next in a gas, which is a significant energy exchange mechanism throughout the atmosphere. As shown in Equation (1.16), the thermal diffusivity is a function of thermal conductivity, density, and the specific heat capacity of the air; this quantity represents the rate of heat transfer, and dictates how quickly temperature gradients in the atmosphere are diffused. High thermal diffusivity in the thermosphere is partially responsible for its isothermal nature at high altitudes [*Schlatter*, 2009]. Similarly to damping by viscosity, the inverse relationship between thermal diffusivity and density indicates fewer molecular collisions and, therefore, transfer of energy by conduction occurs over longer mean free paths. As a result, the waves lose energy as they propagate and, eventually, dissipate.

These two quantities are related by the Prandtl number $\text{Pr} = \frac{\nu}{\alpha}$, which is roughly a constant 0.7–0.8 for an atmosphere, depending on composition [e.g., *Jacobson*, 2005, pp. 242]. Kinematic viscosity, thermal diffusivity, and Prandtl number for each planet are plotted in Figure 1.12.

The absorption of acoustic waves due to viscosity and thermal conduction is given by the classical absorption coefficient in Nepers per meter—a natural logarithmic unit for ratios of measurement [e.g., *Bass and Chambers*, 2001; *Kinsler et al.*, 2000, pp. 217–218]:

$$\alpha_c = \frac{\omega^2}{2\rho c_s^3} \left(\frac{4}{3}\mu + \frac{(\gamma - 1)}{c_p}\kappa \right) \quad (1.17)$$

where μ and κ are the coefficients of molecular viscosity in $\text{kg}/(\text{m}\cdot\text{s})$ and thermal

conductivity in $\text{W}/(\text{m}\cdot\text{K})$ respectively, $\omega = 2\pi f$ with frequency f in Hz, and c_p is the specific heat at constant pressure in $\text{J}/(\text{kg}\cdot\text{K})$.

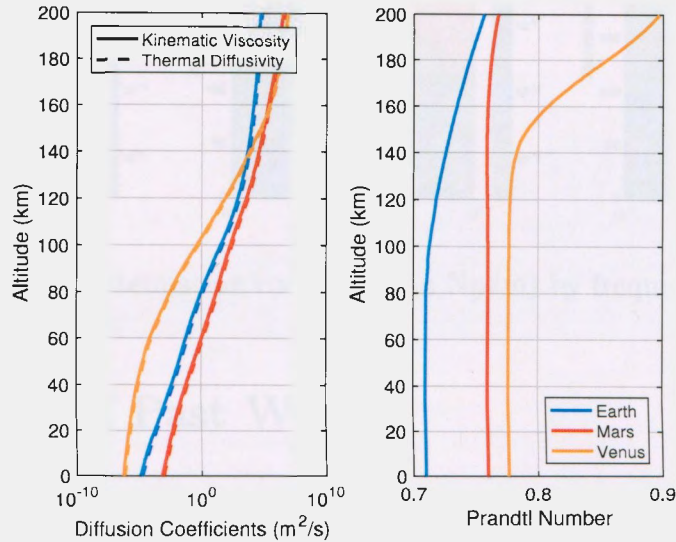


Figure 1.12: Diffusion coefficients and Prandtl number for Earth, Mars, and Venus.

Acoustic attenuation for each planet calculated by Equation (1.17) is plotted in Figure 1.13. Upon inspection it is apparent that the contour lines for each planet are representative of general trends in its temperature profile (Figure 1.2). It is also worth noting that the attenuation profile for Mars plotted here agrees with the results obtained by *Bass and Chambers* [2001] and *Petculescu and Lueptow* [2006]. Each follows the trends expected based on Figure 1.12: Mars has high attenuation, Venus has low attenuation below the cloud layer and high above, and Earth is moderate. Because absorption clearly increases with increasing frequency, infrasound propagates much farther through the atmosphere than audible acoustics—sometimes on the order of thousands of kilometers [*Drob et al.*, 2003]. Waves with extremely long periods (i.e., minutes) may propagate with minimal attenuation to high altitudes.

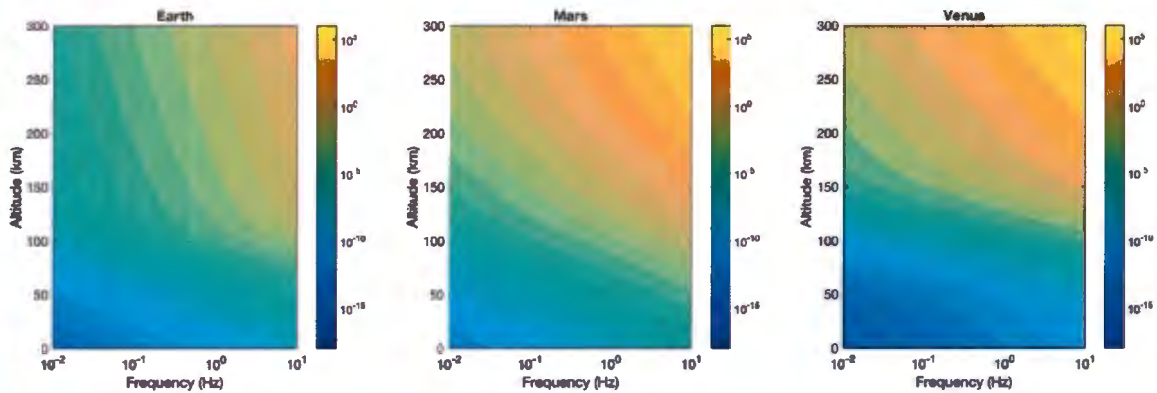


Figure 1.13: Acoustic attenuation coefficient (in Np/m) by frequency and altitude on Earth, Mars, and Venus.

1.3 Review of Past Work

In order to provide appropriate context for the work presented in this thesis, previous studies are first explored. There has been limited study of the propagation of atmospheric acoustic waves on other planets, with the majority of work in this field devoted specifically to Earth. The study of atmospheric infrasound is a significant topic in the field of geosciences, with Google Scholar [<http://scholar.google.com>] searches returning hundreds of publication results within a single year. Figure 1.14 depicts the clear upward trend of atmospheric acoustic wave research over the last twenty-five years, including the growing prominence of studies of other planets. Note that these are simply total numbers of results returned, and all articles may not be completely relevant; nonetheless this method does provide a worthwhile trend for comparison purposes.

1.3.1 Sources of Infrasound

One significant field of study regarding infrasonic acoustic waves has been their sources, which are numerous. Many natural sources (e.g., storms, seismic events) as well as man-made sources (e.g., nuclear detonation, sonic booms) have been investigated theoretically, modeled, and observed over the course of the last century. While it is well-known that storms produce acoustic compressions at the lower end

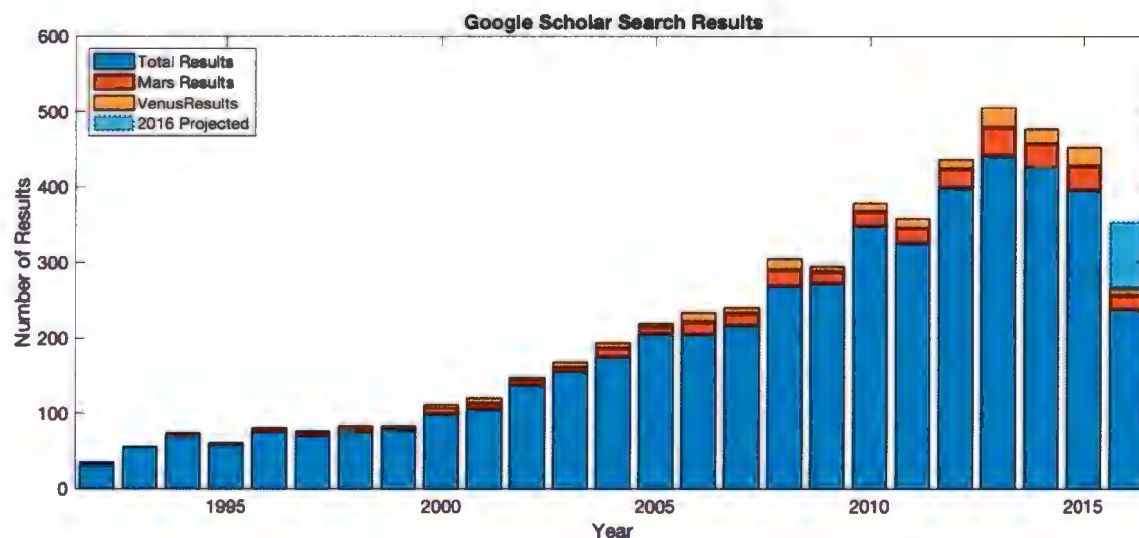


Figure 1.14: Number of Google Scholar search results by year for publications containing the terms “atmosphere”, “infrasound”, “acoustic”, and “waves”, as well as those containing additionally “Mars” or “Venus”. Data were obtained October 2016, and this year’s number has been extrapolated to estimate total year results.

of the audible range—commonly known as thunder—there has been significant study into the formation of additional infrasonic frequencies developed during storms. Recently, *Pasko* [2009] investigated the presence of infrasound signatures due to lightning discharge, and determined that waves on the order of 0.1-1 Hz are produced by electrostatic storm clouds; his work develops a model to confirm experimental observations by *Balachandran* [1979]. Additional measurements of infrasound due to thunderstorms have been made by *Farges and Blanc* [2010], who confirm the presence of 0.1-1 Hz acoustic waves generated by lightning discharge. Furthermore, *Walterscheid et al.* [2003] show, through a time-dependent, nonlinear model, that tropical convective storms produce long period (~ 3 -4 minutes) acoustic waves that are able to propagate to thermospheric heights. These waves are found to cause thermospheric heating (in contrast to gravity waves, which can cool the upper-atmosphere) due to their dissipation at high altitudes. *Hickey et al.* [2001] have modeled these phenomena, and determined that acoustic waves deposit energy at F-region altitudes and may be responsible for observed hot spots.

Seismic sources, such as earthquakes and volcanoes, are notable sources of acoustic waves. *Mutschlecner and Whitaker* [2005] discuss observations of infrasonic signals caused by thirty-one earthquakes, while *Johnson* [2003] considers infrasonic pressure waves generated by active volcanoes. Studies of this nature are key to understanding the dynamics of potentially devastating natural disasters, and there is a large amount of research being devoted to sensing infrasound generated by these events [e.g., *Tanaka et al.*, 1984; *Li et al.*, 2003]. *Zettergren and Snively* [2015] modeled the propagation of infrasonic acoustic waves generated by such sources through the coupling of a neutral atmospheric dynamics model [*Snively and Pasko*, 2008] and a comprehensive ionospheric model [*Zettergren and Semeter*, 2012], and were able to investigate potential detection of these waves by ionospheric disturbances. Furthermore, the European Space Agency's Gravity field and steady-state Ocean Circulation Explorer (GOCE) mission is able to measure seismically induced infrasound, such as that generated by the 2011 Tohoku earthquake, from low-Earth orbit, presenting a new method of detecting and measuring seismic events, as described by *Garcia et al.* [2013].

Shock waves are another example of infrasound in the atmosphere. Impulsive events such as meteor strikes, sonic booms, and detonations can cause immense motions, both in the ground and the atmosphere, which can generate propagating acoustic waves. *Langston* [2004] discusses a 2003 bolide (an extremely bright meteor that often explodes in the atmosphere) event that was observed to produce a sonic boom and seismic response similar to that of a small earthquake. The trajectory of the induced wave was modeled and compared with observed results, which are found to be consistent. However as stated by *Lin and Langston* [2007], large impulsive events are infrequent; they seek to model infrasonic waves generated by thunder and compare them with seismically forced waves in order to draw parallels, a study that achieves comparable results with those for the bolide event. *Besset and Blanc* [1994] perform modeling experiments of acoustic wave propagation induced by shock waves and note nonlinear results, as shown in the figure reproduced as Figure 1.15. Furthermore, mid-twentieth century research was heavily focused on a much more dangerous impulsive event: nuclear detonation. An early report by *Knabe* [1969] details the generation and propagation of internal gravity and acoustic waves by nuclear sources,

and finds that explosions at ground-level are much more likely to produce gravity waves than acoustic waves, but that explosions in the upper-atmosphere are likely to induce detectible infrasonic acoustic waves. Infrasonics is now used to monitor compliance with the Comprehensive Nuclear-Test Ban Treaty [Beddard and Georges, 2000].

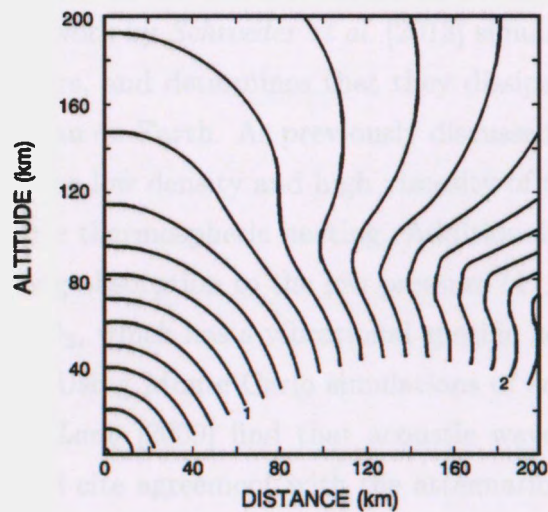


Figure 1.15: Nonlinear propagation of acoustic shock waves generated by a 4 kilotonne explosion. Obtained from *Beset and Blanc* [1994].

1.3.2 Planetary Infrasonics

It is well established that the upward propagation of acoustic waves is incredibly sensitive to the structure of a planetary atmosphere (i.e., composition, pressure, density, and temperature) due to the dependence of the speed of sound on these quantities [Petculescu and Lueptow, 2006]; therefore, it is reasonable to assume that planets with very different atmospheres will have very different acoustic environments. While studies involving the modeling and detection of infrasonics on other planets are comparatively sparse, there have been a fair number of investigations within the last two decades that have begun to shine a light on these phenomena. Recent investigations by *Bass and Chambers* [2001] and *Williams* [2001] have explored the propagation

and absorption of sound in the atmosphere of Mars, and have found that the Martian atmosphere greatly attenuates acoustic waves, particularly in the audible range (i.e., 20–20,000 Hz). *Williams* [2001] notes that waves at 20 Hz dissipate at a rate of 0.419 dB/m on Mars versus 9×10^{-4} dB/m on Earth, while attenuation of sounds in the infrasonic range resembles that of the terrestrial environment more closely. This therefore allows for propagation over greater distances but still not to the extent possible on Earth. Previous work by *Schroeder et al.* [2013] simulates infrasonic acoustic waves of 0.016 Hz on Mars, and determines that they dissipate much more rapidly, and at lower altitudes, than on Earth. As previously discussed, the great attenuation on Mars is likely due to the low density and high viscosity of the atmosphere, as well as the lack of comparative thermospheric heating. Additionally, *Bass and Chambers* [2001] attribute the strong absorption to the low pressure (1/150 atm) and the dominant concentration of CO₂, which has a vibrational specific heat about twenty times greater than that of N₂. Using Monte Carlo simulations of acoustic waves on Earth and Mars, *Hanford and Long* [2009] find that acoustic waves on Mars have lower amplitude and speed, and cite agreement with the attenuation findings of *Bass and Chambers* [2001] in a figure reprinted here as Figure 1.16.

While the majority of non-Earth terrestrial planetary acoustic research is dedicated to Mars, there has been some investigation of Venus, as well as Titan—a moon of Saturn with a significant atmosphere. *Hanford and Long* [2009] include Titan in their study, and *Petculescu and Lueptow* [2006] discuss all four worlds. In the latter, they model predictions of acoustic attenuation similar to those presented in Section 1.2.2 of this thesis, and their results are reprinted here as Figure 1.17.

In addition to modeling, acoustic sensors have been deployed on several planetary missions in order to gather valuable data about the properties of sound on other worlds. As discussed by *Leighton and Petculescu* [2008], four missions have carried microphones: the Venera missions to Venus, the Cassini-Huygens mission to Titan, and the Mars Polar Lander, however the latter lost contact before data could be received. *Petculescu and Lueptow* [2006] also devote a section of their publication to the discussion of passive sensing on other worlds, and present modeled results that seek to predict some of the data that could be obtained in future sensing missions.

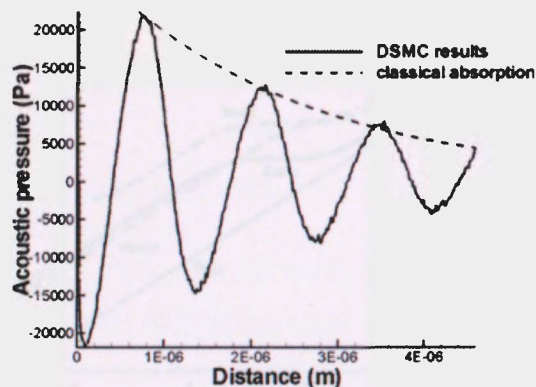


Figure 1.16: Validation of classical absorption in Martian acoustic waves. Obtained from *Hanford and Long* [2009].

In a publication by *Farrelly et al.* [2004], the Environmental Acoustic Reconnaissance and Sounding experiment (EARS) is proposed, which has the goal of characterizing the acoustic environment and propagation of acoustic waves on Mars. Furthermore, *Garcia et al.* [2009] discuss the observation of gravity waves in the Venusian atmosphere by the Visible and Infrared Thermal Imaging Spectrometer Mapper (VIRTIS-M) onboard Venus Express, which they believe to have originated at or near the South Pole due to polar vortex turbulence. The authors also discuss the likelihood of the presence of acoustic waves in the Venusian atmosphere in addition to its ability to support gravity waves.

Understanding how these waves behave on other planets is important, however there is also a need to investigate potential sources. An early study by *Pickhershill and Hunt* [1981] discusses the formation of atmospheric waves by Martian volcanoes, which are significantly larger than those on Earth. They discuss observations of wave-like clouds in the vicinity of Olympus Mons and Ascraeus Mons (two of Mars' largest volcanoes) by Viking Orbiter imagery, and perform some modeling experiments to determine how flow over these massive volcanoes generates mountain lee waves (a type of internal gravity waves); while this study does not specifically mention infrasound, it has been established by *Walterscheid and Hickey* [2005] that gusty flow over hilly terrain can also produce atmospheric acoustic waves. Another potential source of Martian infrasound could be its massive dust storms and dust devils, which grow

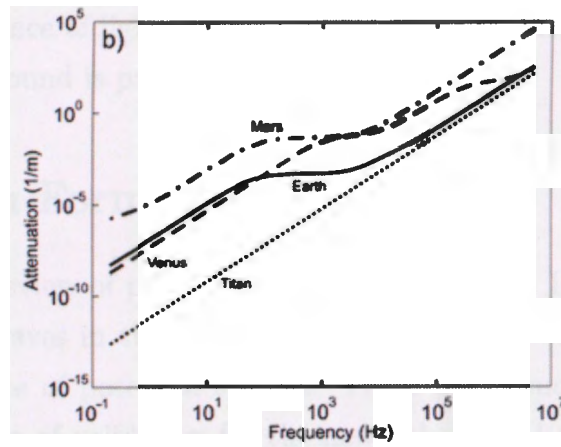


Figure 1.17: Predictions of acoustic attenuation, obtained from *Petculescu and Lueptow* [2006]. Note that these results agree with those presented in Figure 1.13.

considerably larger than those on Earth [e.g., *Tratt et al.*, 2003]; one consideration, however, is that due to Mars' lower density and pressure it takes much greater winds to perturb the air than on Earth. A publication by *Schecter* [2012] discusses the generation of infrasonic acoustic waves by tornadoes on Earth, therefore it is reasonable to consider the possibility of infrasound induced by dust devils on Mars; *Williams* [2001] mentions this hypothesis as well.

Venus, like Earth, has a well-developed tectonic rift system, although the faults likely require greater stress to generate seismic activity [*Foster and Nimmo*, 1996]. Nonetheless, *Garcia et al.* [2005] note that while Venus' seismic activity is weaker than that of Earth, this weakness is counterbalanced by stronger atmospheric coupling. As a result, they hypothesize that Venusian earthquakes of comparable magnitude would produce waves with amplitudes roughly 600 times greater than those produced on Earth at the same pressure level. This study models the vertical propagation of seismically induced infrasound, and concludes that induced temperature perturbations due to the dissipation of these waves is likely large enough to be detected by remote sensing instruments. A publication by *Lorenz* [2012] proposes the inclusion of a seismometer on a future Venus lander mission in order to measure the amplitude and frequency of earthquakes on Venus. Additionally, several publications in the 1980s and 1990s [e.g., *Borucki*, 1982; *Borucki et al.*, 1985; *Russell et al.*, 1993] hypothesize

and model the existence of lightning within the clouds on Venus, and it is likely that storm-induced infrasound is present in its atmosphere.

1.4 Problem Formulation

It is clear from the review of published literature in Section 1.3 that the existence of infrasonic acoustic waves in the atmospheres of Mars and Venus is extremely likely due to the abundance of potential sources. These prior studies provide a basis for comparison and point of validation for the newly-developed model discussed in this thesis. Having provided an in-depth understanding of the atmospheres of the planets to be investigated and the physics of atmospheric infrasound, as well as a review of historical work, this thesis comparatively discusses the propagation, growth, and dissipation of acoustic waves on different terrestrial planets. Furthermore, we perform parametric studies in order to investigate the extent to which background parameters affect infrasonic wave dynamics, and consider which conditions may produce potentially detectible waves on each planet—as well as the limits at which such waves may be detectible on different planets.

In order to achieve these goals, a one-dimensional, nonlinear, compressible, atmospheric acoustics model has been developed, which allows the user to specify any terrestrial planetary parameters. The model does not make assumptions that are only valid on Earth (e.g., predefined values for constituents, etc.) and operates on a basis of generalization throughout its routines. This thesis describes, in detail, the development and validation of this model.

The overarching goal of this thesis is to provide a comprehensive comparison of the atmospheres of the three major terrestrial planets in our solar system—Earth, Mars, and Venus—and examine, in depth, the dynamics of vertical acoustic wave propagation at very low frequencies within them.

1.4.1 Organization of this Thesis

Chapter 1 has provided a breadth of scientific background information relating to the atmospheres of the planets to be studied, introduced atmospheric infrasound from a physical perspective, and provided a detailed review of previously published literature on the subject. Chapter 2 will give a detailed account of the mathematics to be utilized in the modeling performed in this thesis, along with brief derivations of some key parameters. Chapter 3 will extend the mathematics into numerical modeling techniques and provide a detailed discussion of the validation performed on the newly developed model. With the model sufficiently described, Chapter 4 lists the parametric studies performed and interpretations of their outcomes, and Chapter 5 concludes the thesis with key summarizing points and proposes future endeavors that follow naturally from this work.

Chapter 2

PHYSICAL AND MATHEMATICAL BASIS

Before we can introduce the model and investigations performed in this thesis, we review the physics and mathematics used for our problems. This chapter discusses the systems of equations being solved by the model and provides some brief derivations of key parameters. It also provides an explanation of the mathematical description of the waves to be modeled, which will be shown comparatively between the three planets being studied.

2.1 The Euler Equations

The nonlinear, compressible Euler equations describe the conservation of mass, momentum, and energy density of an ideal gas, such as a stratified atmosphere that exists on the planets discussed in this thesis. These equations, derived from the Navier-Stokes equations [*LeVeque*, 2002, pp. 293], are expressed in a generalized form as [*Snively*, 2003]:

$$\frac{\partial \rho}{\partial t} + \nabla \cdot (\rho \vec{v}) = 0 \quad (2.1)$$

$$\frac{\partial(\rho \vec{v})}{\partial t} + \nabla \cdot (\rho \vec{v} \vec{v}) = -\nabla p - \rho \vec{g} \quad (2.2)$$

$$\frac{\partial E}{\partial t} + \nabla \cdot ((E + p)\vec{v}) = -\rho \vec{g} \cdot \vec{v} \quad (2.3)$$

where the equation of state is defined by:

$$E = \frac{p}{(\gamma - 1)} + \frac{1}{2}\rho(\vec{v} \cdot \vec{v}) \quad (2.4)$$

The acoustics model used in this thesis is one-dimensional, so the equations become:

$$\frac{\partial \rho}{\partial t} + \frac{\partial(\rho v_z)}{\partial z} = 0 \quad (2.5)$$

$$\frac{\partial(\rho v_z)}{\partial t} + \frac{\partial(\rho v_z^2)}{\partial z} = -\frac{\partial p}{\partial z} - \rho g \quad (2.6)$$

$$\frac{\partial E}{\partial t} + \frac{\partial(v_z(E + p))}{\partial z} = -\rho g v \quad (2.7)$$

$$E = \frac{p}{(\gamma - 1)} + \frac{1}{2}\rho v_z^2 \quad (2.8)$$

While the Navier-Stokes equations are a parabolic system containing several more terms (namely for diffusion and conduction, discussed later in Section 2.3), for analytical solutions we neglect dissipation to yield this hyperbolic system [LeVeque, 2002, pp. 293], which provides a reasonable approximation for infrasonic acoustic propagation at lower altitudes.

2.2 Linear Dispersion Relation

Dispersion is the phenomenon that describes the dependence of phase speed on a wave's frequency [e.g., *Kinsler et al.*, 2000, pp. 82], and, for acoustics, it is necessary to determine a dispersion relation for the problem at hand. This relation provides a functional description of how wave speed varies with frequency, and is derived from

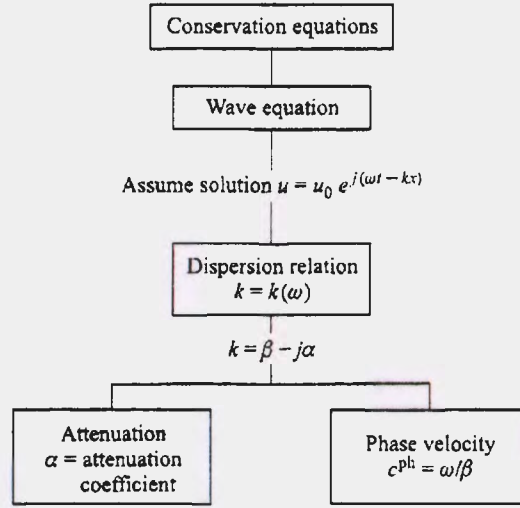


Figure 2.1: Procedure for determining the dispersion relation of a wave. Obtained from *Blackstock* [2000, pp. 299].

the conservation equations by forming a wave equation with an assumed harmonic solution [*Blackstock*, 2000, pp. 300].

Adhering to the algorithm presented by *Blackstock* [2000, pp. 299], reproduced as Figure 2.1, we must first determine our conservation equations by reducing the Euler equations given by Equations (2.1), (2.2), and (2.3) to two dimensions and linearizing them by defining:

$$\rho = \rho_0 + \tilde{\rho} \quad p = p_0 + \tilde{p} \quad v_x = \chi_0 + \tilde{v}_x = \tilde{v}_x \quad v_z = \chi_0 + \tilde{v}_z = \tilde{v}_z$$

where each of these parameters (density, pressure, and x- and y-velocities respectively) is represented by a background value χ_0 plus a small perturbation $\tilde{\chi}$, where χ represents some parameter. Note that this derivation assumes no background wind velocity, thus u_0 and v_0 are zero. Also note that background density and pressure do not vary in the horizontal direction. Neglecting products of first-order perturbations and noting that background quantities do not change with time, we obtain the two-dimensional, linearized Euler equations of motion for a fully-compressible, stratified atmosphere [*Snively and Pasko*, 2008; *de Larquier*, 2010]:

$$\frac{\partial \tilde{\rho}}{\partial t} = -\rho_0 \frac{\partial \tilde{v}_x}{\partial x} - \rho_0 \frac{\partial \tilde{v}_z}{\partial z} - \tilde{v}_z \frac{\partial \rho_0}{\partial z} \quad (2.9)$$

$$\frac{\partial \tilde{v}_x}{\partial t} = -\frac{1}{\rho_0} \frac{\partial \tilde{p}}{\partial x} \quad (2.10)$$

$$\frac{\partial \tilde{v}_z}{\partial t} = -\frac{1}{\rho_0} \frac{\partial \tilde{p}}{\partial z} - \frac{\tilde{\rho}}{\rho_0} g \quad (2.11)$$

$$\frac{\partial \tilde{p}}{\partial t} = -\tilde{v}_z \frac{\partial p_0}{\partial z} - \gamma p_0 \left(\frac{\partial \tilde{v}_x}{\partial x} + \frac{\partial \tilde{v}_z}{\partial z} \right) \quad (2.12)$$

These are the system's conservation equations.

By combining Equations (2.9), (2.10), (2.11), and (2.12) along with the speed of sound given by Equation (1.14), the scale height given by Equation (1.4), hydrostatic equilibrium given by Equation (1.2), and assuming a plane wave (such that $v_x = 0$) solution of the form:

$$v_z = \exp i(\omega t - k_x x - k_z z)$$

we obtain the wave equation:

$$\frac{\partial^2 \tilde{v}_z}{\partial z^2} + \frac{1}{\rho_0} \frac{\partial \rho_0}{\partial z} \frac{\partial \tilde{v}_z}{\partial z} + \left(\frac{\omega^2 - \omega_A^2}{c_s^2} - \frac{\omega^2 - \omega_N^2}{v_\phi^2} \right) \tilde{v}_z = 0 \quad (2.13)$$

with the horizontal phase velocity $v_\phi = \omega/k_x$. Accounting for the density scaling and gravitational stratification of the atmosphere, we define the scaling factor $(\rho_j/\rho_0)^{1/2}$ at some altitude j , which is plotted for each planet in Figure 2.2. This amplification allows for scaling of the perturbation velocity to account for the conservation of kinetic energy as the wave propagates upward. Therefore, we obtain a normalized velocity perturbation:

$$\tilde{w} = \frac{\tilde{v}_z}{\sqrt{\rho_0/\rho_j}} \quad (2.14)$$

yielding the wave equation:

$$\frac{\partial^2 \tilde{w}}{\partial z^2} + \left(\frac{\omega^2 - \omega_A^2}{c_s^2} - \frac{\omega^2 - \omega_N^2}{v_\phi^2} \right) \tilde{w} = 0 \quad (2.15)$$

This equation is governed by the linear dispersion relation [Snively, 2003]:

$$k_z^2 = \frac{\omega^2 - \omega_A^2}{c_s^2} - \frac{\omega^2 - \omega_N^2}{v_\phi^2} \quad (2.16)$$

which can also be written as:

$$k_z^2 = \frac{\omega^2 - \omega_A^2}{c_s^2} - \left(1 - \frac{\omega_N^2}{\omega^2}\right) k_x^2$$

to more clearly indicate the second term's dependence on the horizontal wave number.

The dispersion relation is significant in that it relates wave frequency to the wave's spatial characteristics (i.e., k_x , k_z) as well as to properties of the propagation medium (atmosphere), such as the Brunt-Väisälä and acoustic cut-off frequencies (ω_N and ω_A) and speed of sound (c_s) [Fritts and Alexander, 2003].

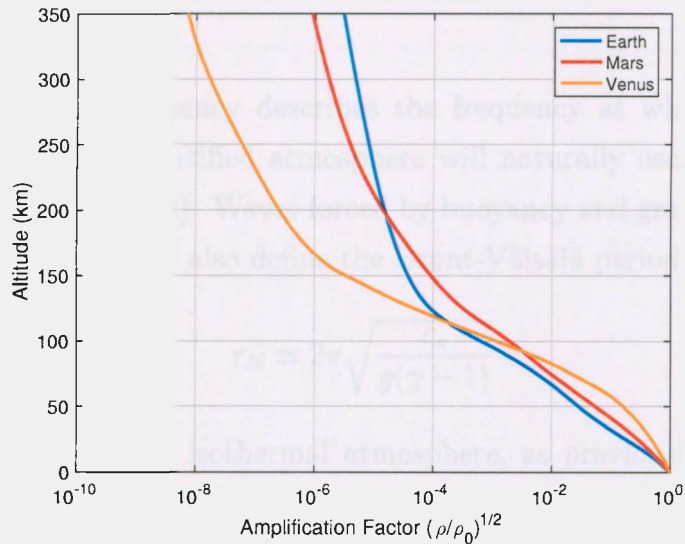


Figure 2.2: Density scaling factor versus altitude for Earth, Mars, and Venus.

Frequency Domains

Equation (2.16) contains two key frequency terms: the acoustic cut-off frequency (ω_A) and the Brunt-Väisälä frequency (ω_N); the latter was discussed previously in Section 1.1.2.

The minimum frequency of a vertically-propagating acoustic wave in a stratified atmosphere is defined by the acoustic cut-off frequency [e.g., *Gossard and Hooke*, 1975, pp. 114]:

$$\omega_A = \frac{g\gamma}{2c_s} \quad (2.17)$$

which is an angular frequency measured in radians per second (recall that $\omega = 2\pi f$). As this thesis primarily discusses waves in terms of their periods rather than their frequencies, it is beneficial to also define the acoustic cut-off period:

$$\tau_A = \frac{4\pi c_s}{g\gamma} \quad (2.18)$$

measured in seconds.

The Brunt-Väisälä frequency describes the frequency at which a parcel of air displaced vertically in a stratified atmosphere will naturally oscillate, and is given previously by Equation (1.10). Waves forced by buoyancy and gravity in this manner are called gravity waves. We also define the Brunt-Väisälä period:

$$\tau_N \simeq 2\pi \sqrt{\frac{c_s}{g(\gamma - 1)}} \quad (2.19)$$

approximated for an ideally isothermal atmosphere, as previously discussed. Note that this approximation does not affect investigations in this thesis, as the domain of propagating infrasonic acoustic waves to be studied involves frequencies well above the Brunt-Väisälä frequency, which is only provided here for reference. There are

two frequency regimes that allow for the propagation of un-trapped waves; these are defined by the two roots of the dispersion relation where $k_z = 0$ [Gossard and Hooke, 1975, pp. 113–118]. Figure 2.4 illustrates these two regions (recall Figure 1.10) by plotting the roots of Equation (2.16) via:

$$k_x^2 = \frac{(\omega^2 - \omega_A^2)\omega^2}{c_s^2(\omega^2 - \omega_N^2)} \quad (2.20)$$

The two roots that govern the domains of wave propagation are the cases where:

$$\frac{\omega^2}{k_x^2} > c_s^2, \quad \omega > \omega_N \quad (2.21)$$

which allows for the propagation of acoustic waves above the acoustic cut-off frequency ω_A , and:

$$\frac{\omega^2}{k_x^2} < c_s^2, \quad \omega < \omega_N \quad (2.22)$$

which allows for the propagation of gravity (buoyancy) waves below the Brunt-Väisälä frequency.

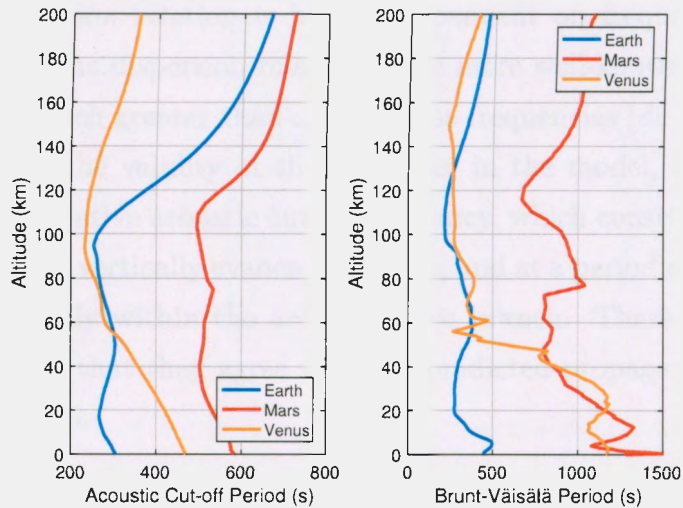


Figure 2.3: Acoustic cut-off and Brunt-Väisälä periods on Earth, Mars, and Venus.

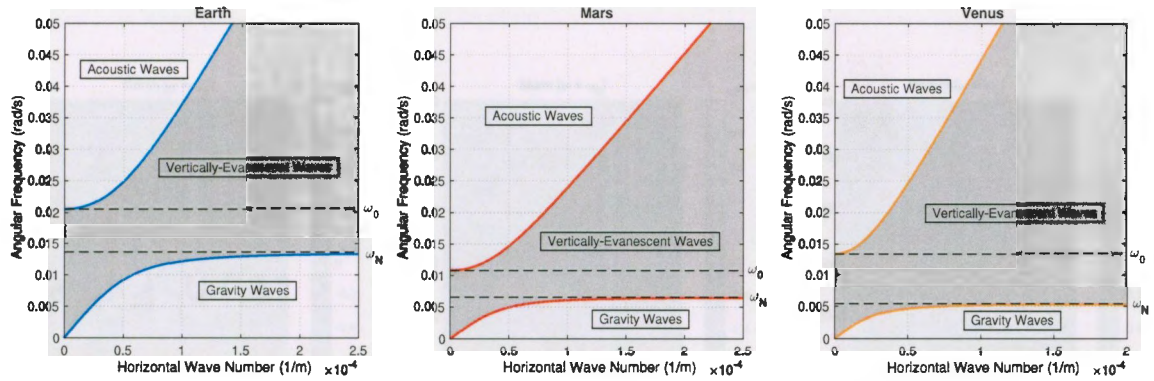


Figure 2.4: Diagnostic diagrams, as discussed by *Gossard and Hooke* [1975, pp. 113–118], illustrate the domains of acoustic and gravity waves based on the linear dispersion relation for $k_z = 0$ at ground-level (assuming the isothermal approximation).

For the one-dimensional model utilized in this thesis, the horizontal wave number k_x is always equal to zero for vertically-propagating waves (whereas for horizontally-propagating cases $k_x \neq 0$ and $k_z = 0$), therefore the dispersion relation reduces to:

$$k_z^2 = \frac{\omega^2 - \omega_A^2}{c_s^2} \quad (2.23)$$

The acoustic dispersion relation is heavily dependent on frequency; for standard, audible frequencies the dispersion relation is the more well-known $k_z^2 = \omega^2/c_s^2$ due to the fact that ω is much greater than ω_A for these frequencies [*de Larquier*, 2010].

In order to test the validity of these regimes in the model, a wave is launched at each planet's respective acoustic cut-off frequency, which constitutes the boundary between acoustic and vertically evanescent waves, and at a period of 2 minutes (0.0524 rad/s), which is firmly within the acoustic wave branch. These have been plotted over time to confirm that they agree with the predicted propagation and are shown in Figures 2.5 and 2.6.

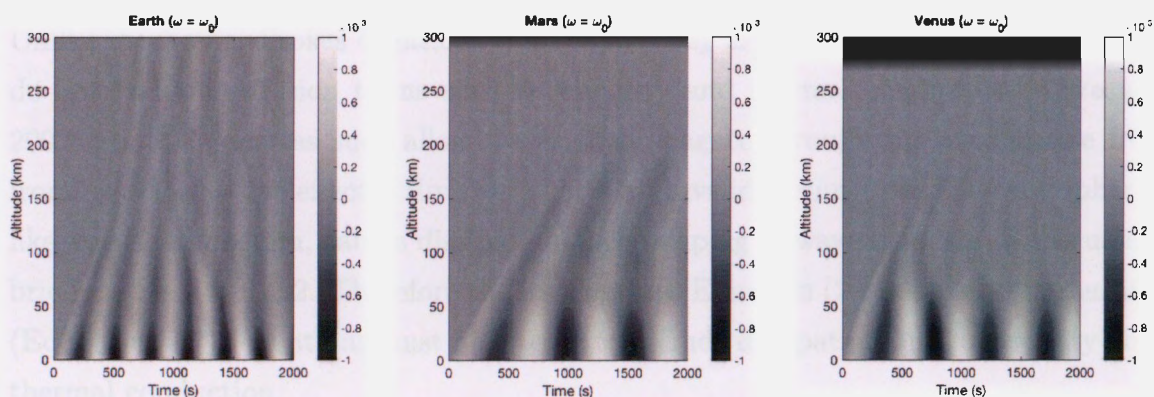


Figure 2.5: Propagation of a continuously forced wave at the acoustic cut-off frequency (at ground) on Earth, Mars, and Venus. Note that the wave is nearly evanescent at low altitudes, consistent with propagation near the cut-off frequency, however it transitions away from evanescence at high altitudes as the cut-off frequency changes with speed of sound. The velocity amplitude is scaled with density via $(\rho_j/\rho_0)^{1/2}$.

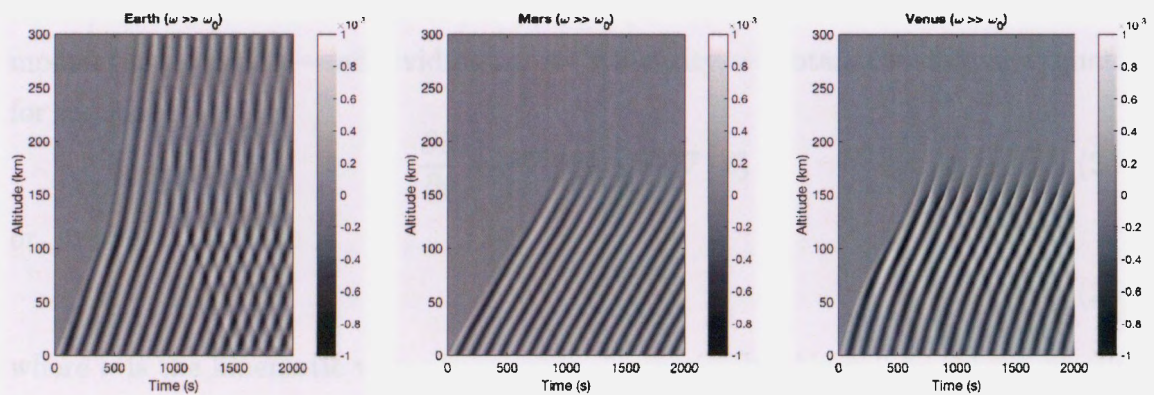


Figure 2.6: Propagation of a continuously forced wave with a period of 120s (0.0524 rad/s), a frequency firmly within the acoustic wave boundary of the diagnostic diagrams (Figure 2.4). Note that the wave shows vertical propagation through the domain, until dissipated or, on Earth, reflected at high altitudes. The velocity amplitude is scaled with density via $(\rho_j/\rho_0)^{1/2}$.

2.3 Diffusion Equations

Unlike the Navier-Stokes equations from which they are derived, the Euler equations do not include diffusion terms such as viscosity and thermal conduction [LeVeque, 2002, pp. 293], and as such allow waves to propagate through the atmosphere free from any dissipative effects. However this is an invalid assumption; the atmosphere, like any fluid medium, causes dissipation and damping of wave motions, as discussed briefly in Section 1.2.2. Therefore the momentum (Equation (2.6)) and energy density (Equation (2.7)) equations must be altered to include dissipation due to viscosity and thermal conduction.

2.3.1 Viscosity

Recall the dynamic viscosity (μ) and kinematic viscosity ($\nu = \frac{\mu}{\rho}$). The Navier-Stokes equation for the conservation of momentum is given by [Landau and Lifshitz, 1987, pp. 45]:

$$\rho \left(\frac{\partial \vec{v}}{\partial t} + \vec{v} \cdot \nabla \vec{v} \right) = -\nabla p - \rho \vec{g} + \mu \nabla^2 \vec{v} + \frac{\mu}{3} \nabla (\nabla \cdot \vec{v}) \quad (2.24)$$

By separating the viscous terms $\mu \nabla^2 \vec{v} + \frac{\mu}{3} \nabla (\nabla \cdot \vec{v})$ from Equation (2.2)—the Euler momentum equation—and dividing across by density, we obtain the diffusion equation for viscosity:

$$\frac{\partial \vec{v}}{\partial t} = \nu \nabla^2 \vec{v} + \frac{\nu}{3} \nabla (\nabla \cdot \vec{v}) \quad (2.25)$$

or, in one dimension:

$$\frac{\partial v_z}{\partial t} = \frac{4\nu}{3} \frac{\partial^2 v_z}{\partial z^2} \quad (2.26)$$

where ν is the kinematic viscosity in m^2/s . Numerically, this will be solved via time-splitting together with the Euler momentum conservation law, which will be discussed in detail in Chapter 3.

2.3.2 Thermal Conduction

The conservation of energy in an ideal fluid is expressed by [Landau and Lifshitz, 1987, pp. 192]:

$$\frac{\partial}{\partial t} \left(\frac{1}{2} \rho (\vec{v} \cdot \vec{v}) + \rho \epsilon \right) = -\nabla \cdot \left[\rho \vec{v} \left(\frac{1}{2} (\vec{v} \cdot \vec{v}) + w \right) \right] - \rho \vec{g} \vec{v} \quad (2.27)$$

where ϵ is the internal energy per unit mass given by [Salby, 1996, pp. 67]:

$$\epsilon = c_v T = \frac{P}{\rho(\gamma - 1)} \quad (2.28)$$

and w is the enthalpy, or total heat content per unit mass.

Recall the thermal conductivity (κ) and thermal diffusivity ($\alpha = \frac{\kappa}{c_p \rho}$). From Fourier's Law, the conductive heat flux equation [e.g., Jacobson, 2005, 21]:

$$\vec{H}_c = -\kappa \nabla T \quad (2.29)$$

estimates the flux of heat energy in W/m^2 through a fluid, such as the atmosphere. Applying Equation (2.4), which defines the energy density E , and considering conduction from Equation (2.29) as heat loss yields the conservation of energy equation:

$$\frac{\partial E}{\partial t} = -\nabla \cdot \left[\frac{1}{2} \rho \vec{v} (\vec{v} \cdot \vec{v}) + \rho \vec{v} \left(\epsilon + \frac{p}{\rho} \right) - \vec{H}_c \right] - \rho \vec{g} \vec{v} \quad (2.30)$$

for enthalpy defined by $w = \epsilon + p/\rho + \delta$ [Landau and Lifshitz, 1987, pp. xiii] where δ represents additional heat sources and/or sinks. This simplifies to:

$$\frac{\partial E}{\partial t} = -\nabla \cdot ((E + p)\vec{v} - \kappa \nabla T) - \rho \vec{g} \vec{v} \quad (2.31)$$

Defining heat density with a form of the heat capacity equation [e.g., Salby, 1996, pp. 65]:

$$Q = \rho c_p \Delta T \quad (2.32)$$

we note that heat Q is a form of energy density E . By separating the diffusion

term, $-\kappa\nabla T$, from Equation (2.3)—the Euler energy equation—and dividing by $c_p\rho$ we obtain the diffusion equation for thermal conduction:

$$\frac{\partial T}{\partial t} = \nabla \cdot (\alpha \nabla T) \quad (2.33)$$

or, in one dimension:

$$\frac{\partial T}{\partial t} = \alpha \frac{\partial^2 T}{\partial z^2} \quad (2.34)$$

where α is the thermal diffusivity in m^2/s . As with viscosity, this will be solved together with the energy conservation law via time-splitting (discussed in Chapter 3).

2.4 Chapter Summary

This chapter has introduced the mathematics involved in the development of the model in order to provide a physical basis for the numerical methods to be discussed in the next chapter. The system of nonlinear, compressible Euler equations with gravity has been presented along with linear diffusion equations for kinematic viscosity and thermal diffusivity derived from the Navier-Stokes conservation equations. Furthermore, the linear dispersion relation for infrasonic acoustic waves has been derived and discussed, and from it the frequency domains of atmospheric phenomena have been defined. Chapter 3 will build upon this mathematical foundation by discussing, in detail, the numerical basis of the model, as well as its validation.

Chapter 3

MODEL DEVELOPMENT AND VALIDATION

The mathematical system that describes the propagation of acoustic waves through a realistic atmosphere cannot be solved using analytical methods. In problems with nonlinearity and variable parameters, numerical methods may be used to provide a reasonable solution that gives insight into the physical system and processes. The development of an appropriate numerical model here involves a computational solution to the system of equations that evolves over time and space, solved over a certain number of temporal and spatial steps. This chapter discusses, in detail, a numerical approach to solving the system of compressible Euler equations with diffusion discussed in the previous chapter. A full description of the mathematical methods and validation efforts is provided. Importantly, this model is constructed to allow case studies for different atmospheres and conditions to be readily constructed.

3.1 Numerical Model

3.1.1 Lax-Wendroff Implementation

The Euler equations are solved using a two-step Richtmyer Lax-Wendroff method for advection. This method utilizes the standard Lax method in the first half-step

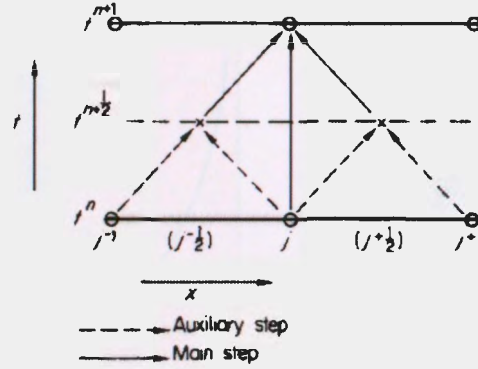


Figure 3.1: Diagram depicting the two steps of the Lax-Wendroff method. Obtained from *Potter* [1973, pp. 68].

to obtain provisional results, then uses a leapfrog method in the second half-step to obtain final values. The Lax-Wendroff method is an explicit forward-in-time-centered-in-space method [e.g. *Hoffman*, 2001, pp. 668]. For a hyperbolic advection equation of the general form [e.g. *LeVeque*, 2007, pp. 201]:

$$\frac{\partial q}{\partial t} + \frac{\partial f(q)}{\partial x} = 0$$

where q represents some quantity and x represents some spatial dimension, the method is given by [*Potter*, 1973, pp. 68]:

$$q_{j+\frac{1}{2}}^{n+\frac{1}{2}} = \frac{1}{2}(q_j^n + q_{j+1}^n) - \frac{\Delta t}{2\Delta x} \left(f(q)_{j+1}^n - f(q)_j^n \right)$$

$$q_j^{n+1} = q_j^n - \frac{\Delta t}{\Delta x} \left(f(q)_{j+\frac{1}{2}}^{n+\frac{1}{2}} - f(q)_{j-\frac{1}{2}}^{n+\frac{1}{2}} \right) \quad (3.1)$$

for each time step n with step size Δt and each spatial step j with step size Δx . Note that for most problems discussed here, the model equations are solved along the z -axis rather than the x -axis, indicating vertical propagation.

The Lax-Wendroff method is conditionally stable, provided that the Courant-Friedrichs-Lewy stability condition is met, defined as:

$$CFL = \frac{|c_s| \Delta t}{\Delta x} \leq 1 \quad (3.2)$$

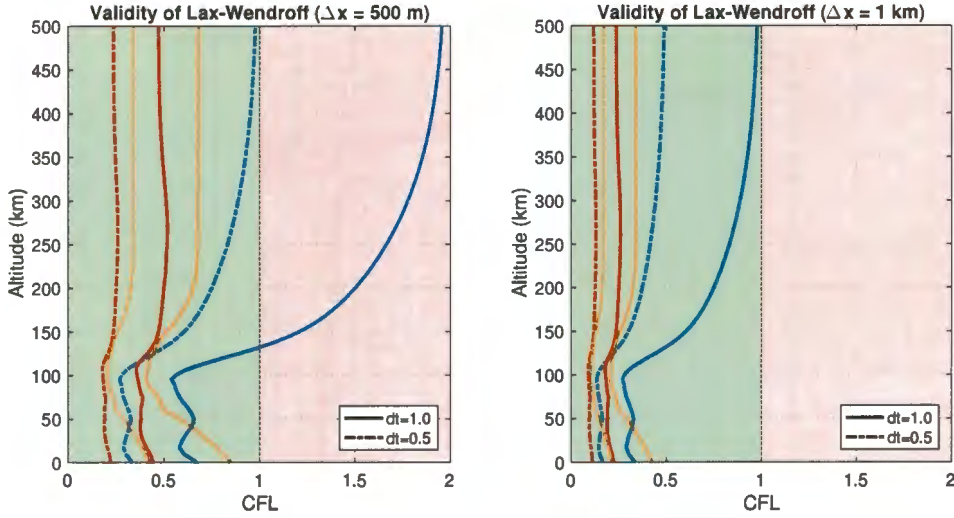


Figure 3.2: Validity of the Lax-Wendroff method on Earth, Mars, and Venus for several different time steps with a Δx of 500 meters and 1 kilometer, where green indicates stability and red indicates instability.

In order to ensure that this condition is satisfied, the model has been developed to allow the user to specify the desired CFL number in addition to the spatial step-size, and it then selects an appropriate temporal step-size to ensure stability. Figure 3.2 indicates validity of the Lax-Wendroff method for the three planets being investigated.

Gravity is calculated analytically to balance the model in a steady state based on the initial density and pressure profiles. From hydrostatic equilibrium [e.g., *Taylor*, 2010, pp. 95]:

$$dp = -\rho g dz \quad (3.3)$$

an analytic expression for gravity is given by:

$$g = -\frac{p_{j+1}^0 - p_j^0}{\frac{\Delta z}{2}(\rho_{j+1}^0 + \rho_j^0)} \quad (3.4)$$

where p^0 and ρ^0 represent the pressure and density at time $t = 0$. This expression is solved with the Lax-Wendroff method for momentum and energy as it appears in the Euler equations given by Equations (2.2) and (2.3).

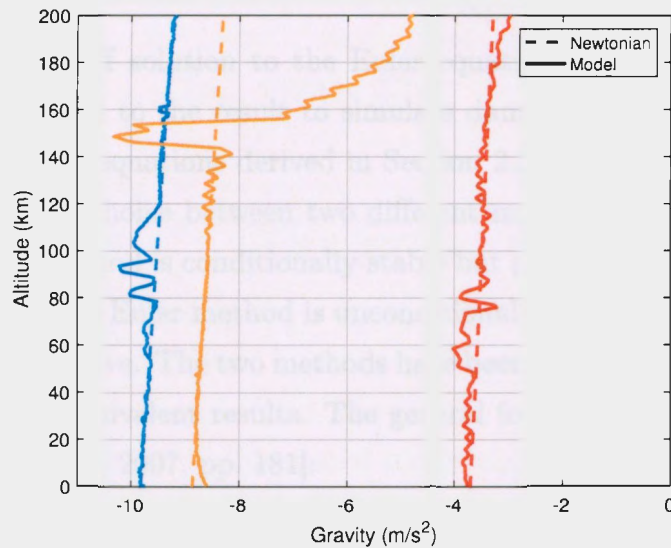


Figure 3.3: Model gravity validated against Newtonian gravity calculation.

While steady state is maintained throughout the domain, the agreement with physical gravity varies with altitude on each planet, as shown in Fig. 3.3. On Earth, the largest region of disagreement occurs between 80 and 120 kilometers, which is where the mesosphere transitions into the thermosphere, indicated by a steep temperature gradient and significant change in chemical composition (see Figure 1.6 and Figure 1.3). Mars, for the most part, agrees with the Newtonian calculation, with some small variance around 60 to 80 kilometers where there is a sharp change in temperature gradient, as shown in Figure 1.2. Finally, while Venus agrees almost perfectly for the majority of the altitude domain, the agreement seems to rapidly break down around 150 kilometers, although this is near the planet’s exobase (recall Figure 1.9) and thus waves do not propagate to this height anyway. It should also be considered that the profile output by VenusGRAM 2005 is likely of lower fidelity compared to EarthGRAM 2010 and MarsGRAM 2010. Overall, the analytic gravity approximation agrees to the extent needed to appropriately balance the model and produce a valid simulation of propagating acoustic waves in these three atmospheres.

3.1.2 Euler Diffusion

After the Lax-Wendroff solution to the Euler equations is determined, a diffusion method is then applied to the result to simulate damping by viscosity and thermal conduction (recall the equations derived in Section 2.3). The model has been developed to allow for the choice between two different numerical methods for diffusion. The explicit Euler method is conditionally stable but provides significantly faster run time, while the implicit Euler method is unconditionally stable but significantly more computationally intensive. The two methods have been validated to confirm that they produce sufficiently equivalent results. The general form of the diffusion equation is given by [e.g., *LeVeque*, 2007, pp. 181]:

$$\frac{\partial q}{\partial t} = K \frac{\partial^2 q}{\partial x^2}$$

where q represents some quantity, x represents some spatial dimension, and K is a diffusion constant.

Explicit Method

The simplest numerical scheme for solving the diffusion (heat) equation would be the explicit forward Euler method, given by [e.g., *Hoffman*, 2001, pp. 353]:

$$q^*_{j^{n+1}} = q^*_{j^n} + \frac{K \Delta t}{(\Delta x)^2} (q^*_{j+1} - 2q^*_{j^n} + q^*_{j-1}) \quad (3.5)$$

where q^* represents the result from the Lax-Wendroff method and K is the diffusion constant, equal to $4\nu/3$ for viscosity and α for thermal diffusivity, as discussed previously. These equations act, respectively, on the velocity v_z —obtained from the momentum equation simply by dividing out density—and on temperature T , which is obtained from the energy equation given that:

$$E = \rho c_v T + \frac{1}{2} \rho v_z^2 \quad (3.6)$$

However, this method is conditionally stable, requiring that:

$$\Delta t \leq \frac{\Delta x^2}{2K}$$

or:

$$CFL = \frac{\Delta x^2}{K\Delta t} \leq \frac{1}{2} \tag{3.7}$$

This makes it difficult to select a temporal step-size for the model, as it must meet the criteria in both Equation (3.2) and Equation (3.7). Due to the highly-viscous nature of the atmospheres of Mars and Venus, there is no reasonable time step that, when used in conjunction with a desirable spatial step size Δx (i.e., 1 km or less), produces a stable solution for the entire altitude domain. Figure 3.4 depicts the CFL number over the altitude domain for each planet at Δt values of 0.1 second, 0.5 seconds, and 1.0 seconds. As is evidenced by Equation (3.7) and illustrated by the figure, the altitude ceiling for validity of the explicit Euler scheme decreases with increasing Δt , and also decreases with decreasing Δx .

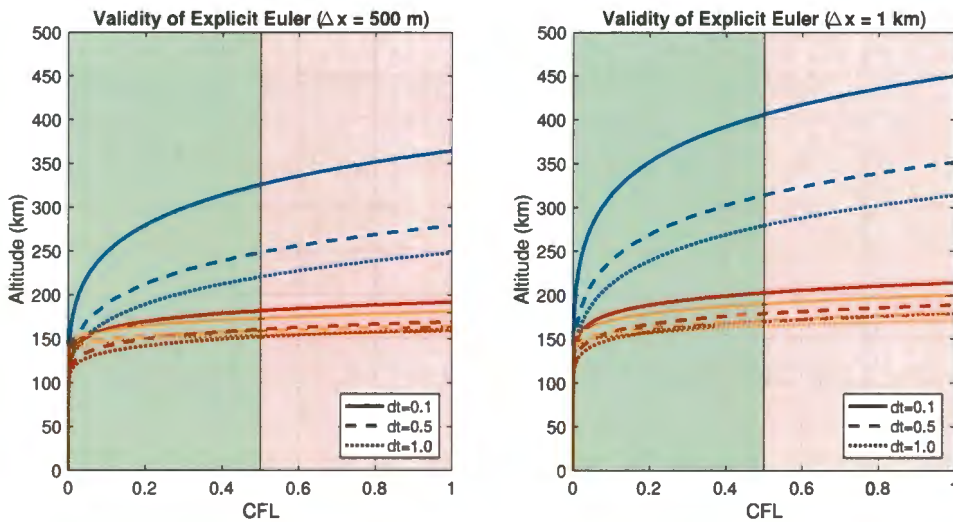


Figure 3.4: Validity of the explicit Euler method on Earth, Mars, and Venus for several different time steps with a Δx of 500 meters and 1 kilometer, where green indicates stability and red indicates instability. Note that none of the values produce a valid CFL number on Mars and Venus to the desired simulation range of 200 kilometers.

Implicit Method

To address the limited stability of the explicit method, an alternative approach is the time-split implicit backward Euler solution [e.g., *Hoffman*, 2001, pp. 356]:

$$q_j^{*n+1} = q_j^{*n} + \frac{K\Delta t}{(\Delta x)^2}(q_{j+1}^{*n+1} - 2q_j^{*n+1} + q_{j-1}^{*n+1}) \quad (3.8)$$

The method of solving this implicit method involves the use of matrix methods. Defining a constant:

$$C = \frac{K\Delta t}{(\Delta x)^2} \quad (3.9)$$

yields the backward Euler method in the form:

$$-Cq_{j+1}^{*n+1} + (2C + 1)q_j^{*n+1} - Cq_{j-1}^{*n+1} = q_j^{*n}$$

This may be written as a matrix equation:

$$\vec{q}^{*n+1} = A^{-1}\vec{q}^{*n} \quad (3.10)$$

where q^* represents the result from the Lax-Wendroff method and:

$$A = \begin{bmatrix} 2C + 1 & -C & 0 & \dots & 0 & 0 & 0 \\ -C & 2C + 1 & -C & 0 & \dots & 0 & 0 \\ \vdots & \vdots & \vdots & \vdots & \vdots & \vdots & \vdots \\ 0 & 0 & \dots & 0 & -C & 2C + 1 & -C \\ 0 & 0 & 0 & \dots & 0 & -C & 2C + 1 \end{bmatrix} \quad (3.11)$$

Equation (3.10) is solved for the vector \vec{q}^{*n+1} over all space to obtain a solution to the diffusion equation.

Note that the implicit Euler method is unconditionally stable, however it is not unconditionally accurate. The implicit Euler accuracy is validated by comparing a wave generated with each of the two methods, and ensuring that they are the same, as shown in Fig. 3.5. One caveat of the implicit scheme is that the model computation

is somewhat more time-intensive than the explicit scheme—about 10% slower—so for cases where a stable time step is easily selected, the explicit method may be preferred. The model allows for selection of the diffusion method via a command-line flag at runtime.

Validation of Diffusion

A sixty-second Gaussian wave packet (the forcing function is discussed in detail in Section 3.1.3) was simulated propagating upward on Earth using each diffusion scheme in order to ensure that both methods produce agreeable results. The output was found to be within 1×10^{-6} meters per second of each other up to an altitude of 200 kilometers and above, as shown in Figure 3.5.

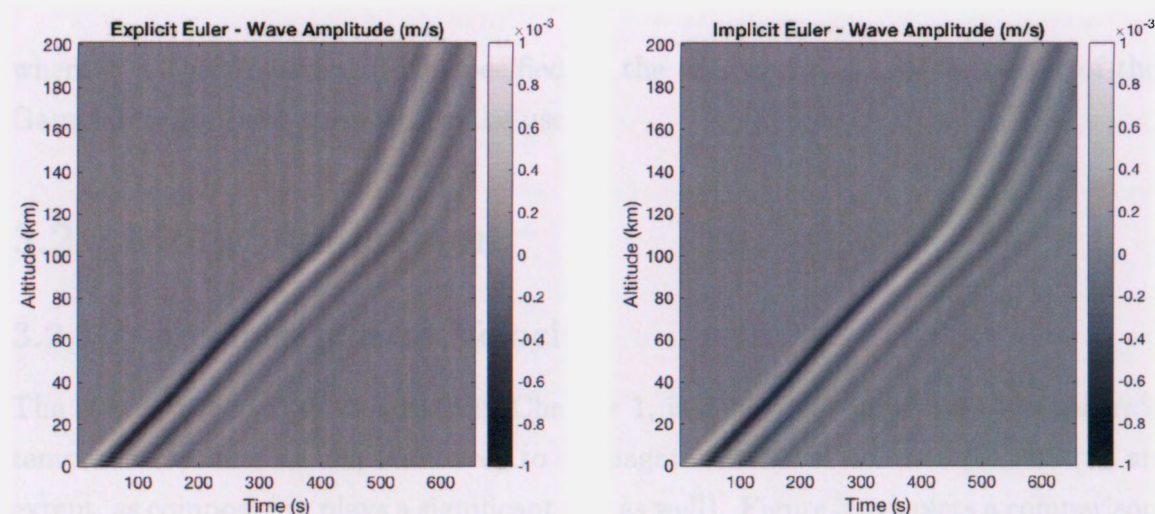


Figure 3.5: Propagation of a sixty-second wave on Earth, using explicit diffusion and implicit diffusion. The results agree reasonably to 10^{-6} m/s. Note that the velocity amplitude is scaled with density via $(\rho_j/\rho_0)^{1/2}$, as discussed previously in Section 2.2.

3.1.3 Wave Forcing

The user has the option to select continuous wave forcing that will generate a wave over the entire time domain or a packet forcing that will excite a single wave packet to propagate upward. Waves are forced at the bottom of the model via a simple forcing function:

$$v_0(t) = a \sin(\omega t) \quad (3.12)$$

with a compressional velocity amplitude a and period (used to determine frequency ω) provided by the user. For continuous forcing, this function remains as is, however for a packet a Gaussian term must be included as such:

$$v_0(t) = ae^{-(t-t_{center})^2/\sigma^2} \sin(\omega(t - t_{center})) \quad (3.13)$$

where σ is the Gaussian width specified by the user and t_{center} is the center of the Gaussian pulse (also specified by the user).

3.2 Model Validation

3.2.1 Wavelength and Velocity

The speed of sound, as discussed in Chapter 1, is dependent upon the atmosphere's temperature, thus we expect waves to propagate faster on warmer planets (to an extent, as composition plays a significant role as well). Figure 3.6 depicts a comparison of sixty-second waves propagating upward over time on each of the three planets. These waves are in agreement with speed expectations, as it is clear that, initially, Venus is moving the fastest due to its high temperature atmosphere. However at higher altitudes where Venus' atmosphere begins to cool and Earth's becomes hotter, the Venusian wave slows down while the Earthly wave gains speed; the Martian wave is the slowest throughout the domain.

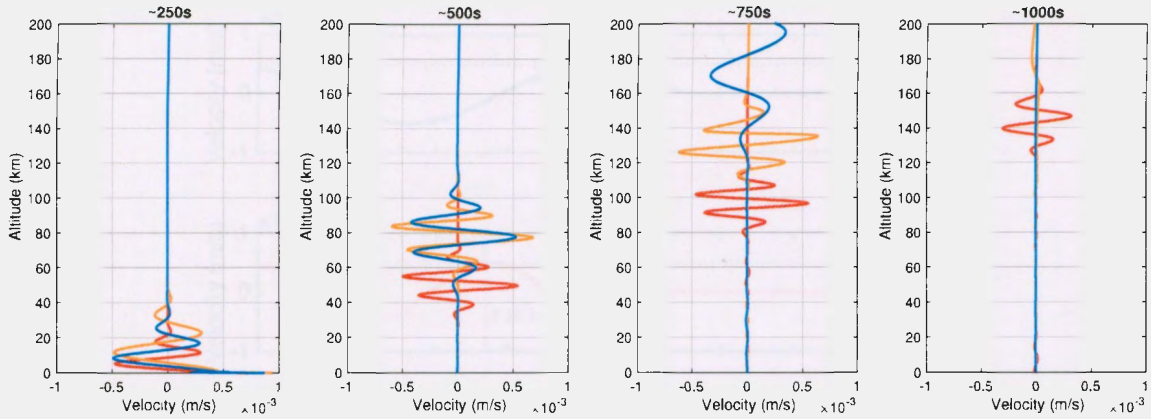


Figure 3.6: One-minute period wave propagating upward over time on Earth, Mars, and Venus.

The wavelength of an acoustic wave is dependent on its frequency and speed, such that:

$$\lambda = \frac{c_s}{f} = c_s \tau \quad (3.14)$$

where τ is the period of the wave ($\tau = 1/f$) in seconds and c_s is the speed of sound given by Equation (1.14).

For validation purposes, an alternate version of the model was developed which propagates a wave horizontally (such that $k_z = 0$ and $k_x \neq 0$) at a specified altitude using the same methods and diffusion processes as in the vertical propagation model.

In order to validate that the model produces waves of the correct scale, a thirty-second acoustic wave is propagated horizontally through each atmosphere at surface altitude. For the Earth we anticipate a wavelength of ~ 10 km, for Mars we anticipate a wavelength of ~ 7.5 km, and for Venus we anticipate a wavelength of ~ 13 km. It is worth noting that the wavelength of the propagating acoustic wave is directly related to the temperature of the atmosphere, such that as temperature declines the waves are expected to become more compressed, as is apparent in Figure 3.6. The model was successfully validated to confirm each of these three wavelengths, as shown in Figure 3.7.

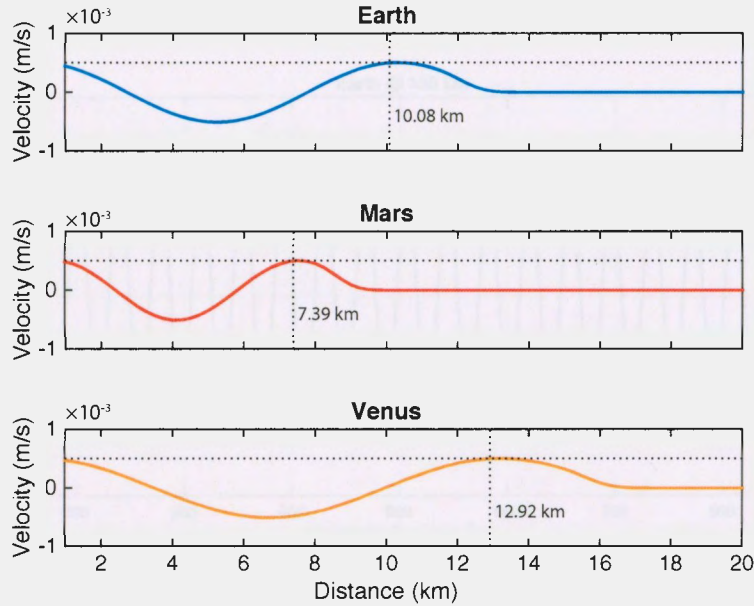


Figure 3.7: Wavelength validation for acoustic waves propagating horizontally at the surface of each planet.

3.2.2 Attenuation

Figure 1.13 depicts acoustic attenuation as a function of frequency and altitude, such as given by Equation (1.17). In this thesis we focus on infrasonic acoustic waves with periods between 10 and 90 seconds (i.e., frequency below 0.1 Hz), meaning that attenuation will be almost non-existent at altitudes below the thermosphere. While the amplitude of the wave is affected as it propagates upward, for a horizontal propagation we should see only damping by classical attenuation, due to the kinematic viscosity and thermal diffusivity at that altitude. Attenuation at infrasonic frequencies at thermospheric heights is on the order of 10^{-8} – 10^{-6} , so the waves must travel a great distance for damping to be apparent. Waves are excited and allowed to propagate horizontally at a high altitude (selected individually) on each planet, and the attenuation is observed, as shown in Figures 3.8, 3.9, and 3.10. Note that, of the three, Mars has the highest attenuation and also has the clearest downward slope of wave amplitude as it propagates horizontally. These plots also provide insight into the varied wavelengths due to speed of sound differences.

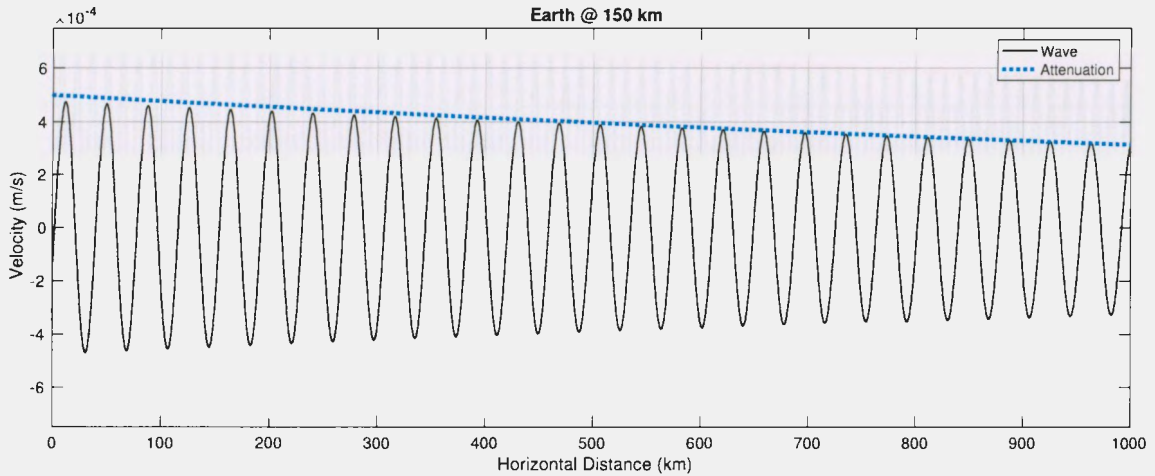


Figure 3.8: Attenuation validation for an acoustic wave with a period of one minute propagating horizontally at 150 km on Earth. The coefficient of attenuation at this altitude is about $\alpha_c = 4.5 \times 10^{-7}$ Np/m.

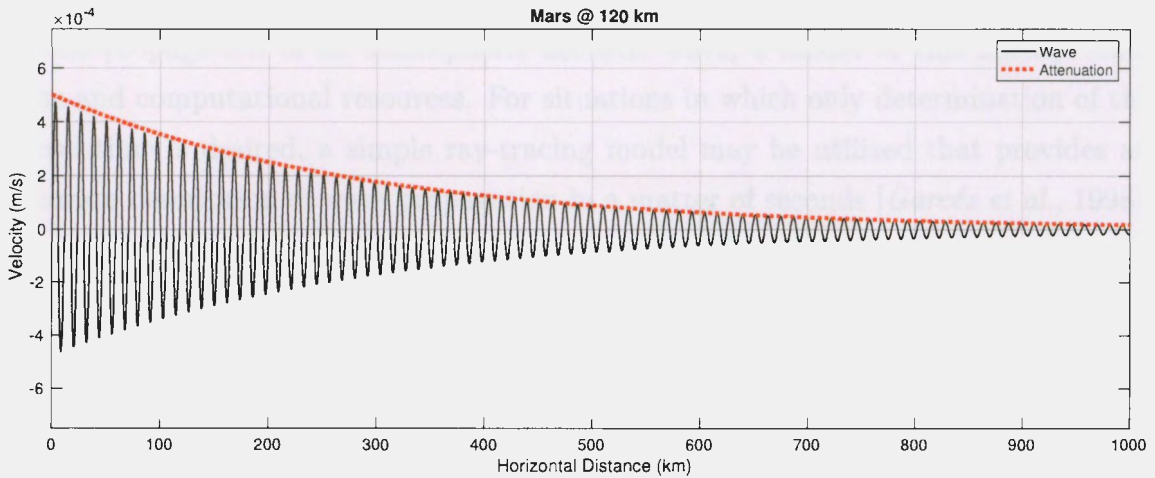


Figure 3.9: Attenuation validation for an acoustic wave with a period of one minute propagating horizontally at 120 km on Mars. The coefficient of attenuation at this altitude is about $\alpha_c = 3.5 \times 10^{-6}$ Np/m.

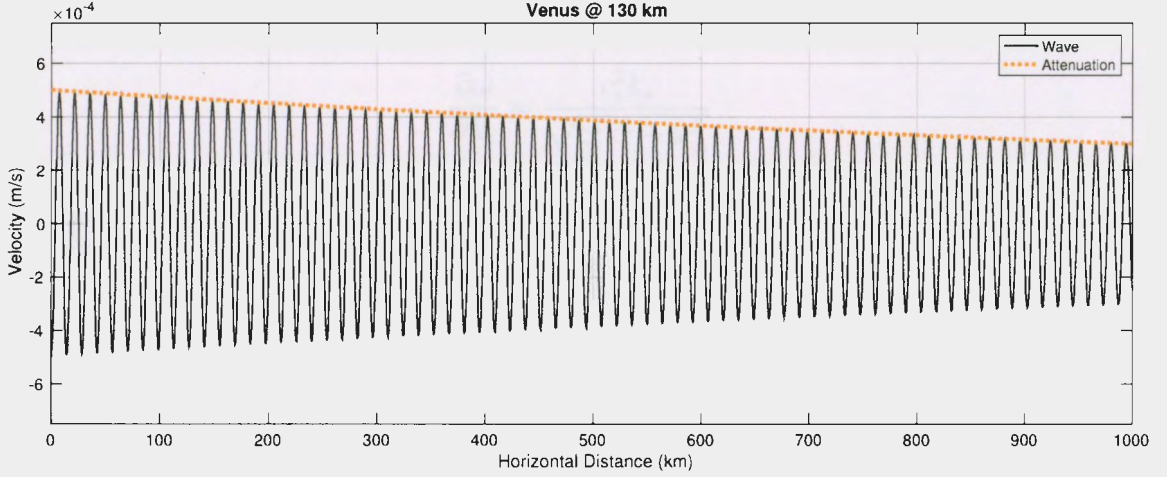


Figure 3.10: Attenuation validation for an acoustic wave with a period of one minute propagating horizontally at 130 km on Venus. The coefficient of attenuation at this altitude is about $\alpha_c = 5.1 \times 10^{-7}$ Np/m.

3.3 Ray-Tracing Model Predictions

While the one-dimensional model has been validated to provide accurate solutions to the propagation of an atmospheric acoustic wave, a model of this fidelity takes time and computational resources. For situations in which only determination of the travel time is desired, a simple ray-tracing model may be utilized that provides an accurate description of wave propagation in a matter of seconds [Garcés *et al.*, 1998]. In order to provide predictions of acoustic wave propagation over time and provide further validation of the Lax-Wendroff solution, a ray-tracing model, similar to that discussed by Heale and Snively [2015], was developed using a Runge-Kutta fourth order (RK4) solution to the dispersion relation:

$$k_z^2 = \frac{\omega^2 - \omega_A^2}{c_s^2} \quad (3.15)$$

derived in Section 2.2. This equation is rearranged and differentiated to yield:

$$\frac{\partial \omega}{\partial k_z} = \frac{c_s^2 k_z}{\sqrt{c_s^2 k_z^2 + \omega_A^2}}$$

where $\frac{\partial \omega}{\partial k_z}$ is the group velocity of the wave packet [Song et al., 2014], such that:

$$\frac{\partial \omega}{\partial k_z} = vgz = \frac{\partial z}{\partial t}$$

From Equations (2.16) and (2.17), this becomes:

$$\frac{\partial z}{\partial t} = \frac{c_s(z)}{\omega} \sqrt{\omega^2 - \left(\frac{g(z)\gamma(z)}{2c_s(z)} \right)^2} \quad (3.16)$$

Equation (3.16) is solved using an RK4 method implemented in MATLAB[®] as such:

$$z_{n+1} = z_n + \frac{\Delta t}{6} (\xi_1 + 2\xi_2 + 2\xi_3 + \xi_4)$$

$$t_{n+1} = t_n + \Delta t$$

for $n=0, 1, 2, 3, \dots$, using the terms defined by:

$$\xi_1 = f(t_n, z_n)$$

$$\xi_2 = f\left(t_n + \frac{\Delta t}{2}, z_n + \frac{\Delta t}{2}\xi_1\right)$$

$$\xi_3 = f\left(t_n + \frac{\Delta t}{2}, z_n + \frac{\Delta t}{2}\xi_2\right)$$

$$\xi_4 = f(t_n + \Delta t, z_n + \Delta t\xi_3)$$

Figure 3.11 depicts the propagation of a sixty-second wave on each of the three planets as predicted by the RK4 ray-tracing model, which agrees with expectations based on the planets' respective speeds of sound. In order to further validate propagation in the numerical acoustics model, the ray-tracing predictions are plotted against an upward-propagating wave packet on each of the planets. There is clearly agreement

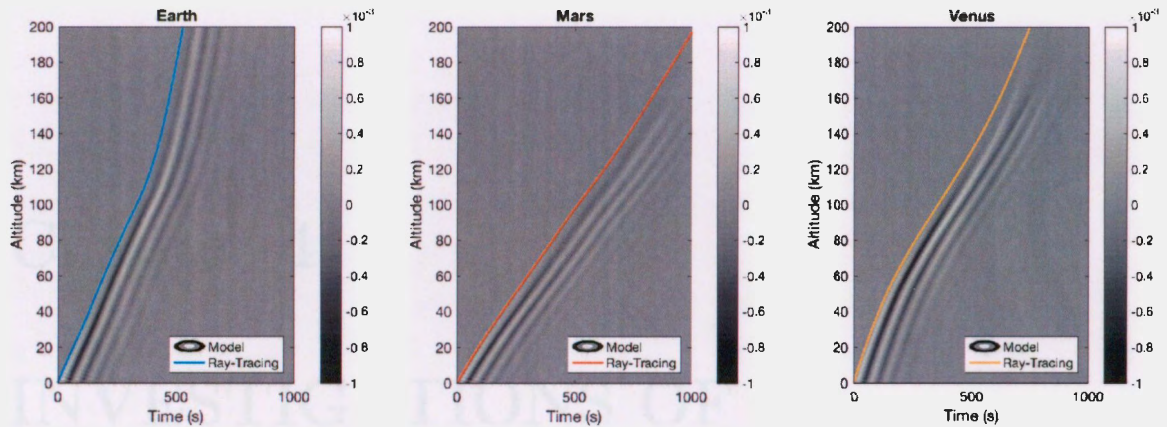


Figure 3.11: The one-dimensional acoustics model is validated using the Runge-Kutta ray-tracing model.

between the two models and our expectations, which, therefore, provides reasonable validation for each acoustics model. Note that the ray-tracing equations are inviscid, and therefore the ray-tracing solution cannot simply replace the Lax-Wendroff model. Nevertheless, they provide insight into the propagation of the waves.

3.4 Chapter Summary

Following from the mathematical background provided by Chapter 2, this chapter has presented the numerical methods used to solve the previously discussed systems of equations in order to successfully simulate the propagation and dissipation of atmospheric infrasound. The Euler equations are solved using a forward-in-time-centered-in-space Lax-Wendroff two-step method for advection, and the linear diffusion equations are solved using either a forward or backward Euler method in a time-split fashion. Additionally, several validation efforts have been introduced in order to confirm that the model operates appropriately and as expected. Wavelength, velocity, and attenuation were verified against expected, analytical values, and a simple ray-tracing model was developed for comparison to the full nonlinear, compressible model and confirmed to agree.

Chapter 4

INVESTIGATIONS OF PARAMETER EFFECTS

The goal of this thesis is to perform an extensive investigation into acoustic wave sensitivity to various parameters so as to determine optimal conditions for detection in the atmospheres of Earth, Mars, and Venus. It is well-established that the propagation and dissipation of infrasound is sensitive to ambient atmospheric profiles, such as temperature, density, and chemical composition, and there are many factors at play that may affect these quantities. For example, different times of day, seasons, and places on the globe have different temperatures both at the surface of the planet and in the thermosphere, and therefore we would expect waves to propagate and grow differently in each scenario. Furthermore, the frequency of the wave plays a significant role in the altitude to which it can propagate, particularly due to the fact that attenuation is a direct function of frequency.

This chapter provides model results for large parameter sweeps of atmospheric and wave parameters in order to determine each planet's overall sensitivity to ambient conditions.

4.1 Variation of the Atmosphere

For sweeps in which the ambient atmosphere is varied we examine differences in maximum amplitude, the altitude of maximum amplitude, and the time of propagation to 100 km—the middle of the atmosphere on all three planets—and to 200 km—the thermosphere of all three planets.

4.1.1 Diurnal

Perhaps the most obvious parameter to consider, time of day certainly affects the atmospheric profile of a planet, and thus plays a significant role in defining the propagation and dissipation of infrasonic waves. Everybody is familiar with these effects—it is hotter during the day, while the sun is out, than it is in the middle of night—but the extent of the difference goes beyond temperature at the surface. The presence of the sun, or lack thereof, is responsible for changes in thermospheric composition due to energy imparted on particles in the ionosphere. Figure 4.2 depicts variations in composition between day and night. These effects are similar to those seen due to variations in solar activity, discussed later in Section 4.1.

A fact of note for this investigation is that a day on each of the planets is not equal, as discussed briefly in Chapter 1. Compared to the 24-hour day as we know it, a Martian day (known as a *sol*) is only 40 minutes longer and a Venusian day is roughly 243 Earth days. This is determined by the rotation rates of the planets, of which Earth and Mars are fairly similar whereas Venus rotates very slowly—in fact, Venus rotates in the opposite direction, so the sun rises in the west and sets in the east, contrary to Earth. This is shown later in Figure 4.6. Recall from Chapter 1 that the length of Venus' day is likely the reason why there is such a great contrast between day and night temperatures—the atmosphere and surface have much more time to heat up and cool down than they do on Earth or Mars. Figure 4.1 depicts differences in temperature between day and night.

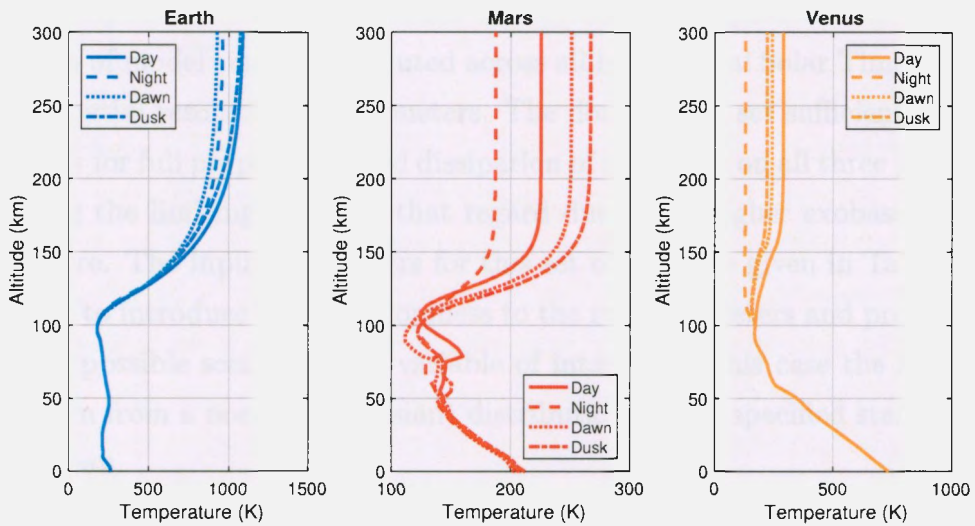


Figure 4.1: Temperature variation at different times of day.

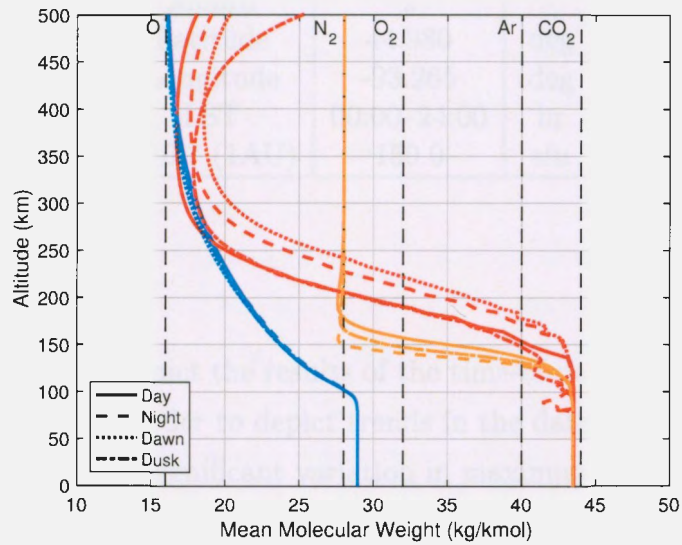


Figure 4.2: Atmospheric composition variation at different times of day.

Description

In order to explore the variation of wave travel time and amplitude with local time of day, a batch of model runs was executed across all hours Local Solar Time (LST) with a vertical spatial resolution of 250 meters. The domain was set sufficiently high (500 km) to allow for full propagation and dissipation of the waves on all three planets, with Earth being the limiting factor in that regard due to its higher exobase and denser thermosphere. The input parameters for this set of runs are given in Table 4.1.

In order to introduce some randomness to the run parameters and provide greater coverage of possible scenarios, the variable of interest (in this case the LST) is randomly drawn from a normal (Gaussian) distribution with a specified standard deviation and mean.

Table 4.1: Model input parameters for the diurnal variation run set.

Parameter	Value	Unit
τ	60	s
t_{center}	240	s
σ	60	s
Amplitude	1×10^{-3}	m/s
Month	2	-
Latitude	44.980	deg
Longitude	-93.265	deg
LST	00:00–24:00	hr
F10.7 (1AU)	150.0	sfu

Model Results

Figures 4.3, 4.4, and 4.5 depict the results of the time-of-day sweep. A polynomial of sufficient order is used in order to depict trends in the data.

Earth does not show a significant variation in maximum amplitude, as evidenced by its $< 1\%$ difference given in Table 4.2, which is supported by its lack of change in its thermospheric temperature and, to a greater extent, composition. Between the three planets studied we would certainly expect Earth waves to remain the most consistent simply based on the profiles—this is also reasonable due to the fact that its day is the

shortest of the three planets, albeit not by much. The most interesting part of the Earth results, however, is that there is a very clear trend that finds dawn and dusk wave amplitudes higher than those at noon and midnight. Furthermore, while the travel time to 100 km shows no clear correlation, the travel time to 200 km (within the thermosphere) is noticeably lower during the day, when the temperature is the highest. This is obvious due to the dependence of the speed of sound on temperature.

In contrast to Earth, Mars shows significant variation in temperature by time of day; this was discussed previously in our description of the thermosphere in Chapter 1. Martian waves show a clear trend of increasing velocity amplitude with increasing temperature with, as expected, the opposite effect on time of propagation. One explanation for this phenomenon is that, although temperatures are higher during the day, so is the concentration of heavy species (i.e., carbon dioxide and argon), therefore the atmosphere sees an increase in viscosity with the presence of these molecules. If the difference in viscosity is greater than the difference in thermal conduction this trend would be expected.

Because Venus shows the greatest difference in day versus night profiles we would expect it to also result in the greatest difference in wave growth across the time of day sweep. According to Table 4.2 this is true, as the Venusian waves show more than triple the percent difference between the highest and lowest maximum amplitude than the Earth waves. Like Mars, Venus shows a correlation between high temperatures and high amplitudes. Because Venus is also a CO₂ atmosphere, the previous explanation is supported. Furthermore, the Venusian waves, like those on Earth, show no correlation for time of propagation to 100 km. Unlike Earth, however, Venus' atmosphere below the clouds remains completely unchanged regardless of the time (or position on the globe, which will be discussed in the next section), whereas on Earth there is what appears to be random noise in the time of propagation results due to small—though uncorrelated—variations in the lower-atmosphere.

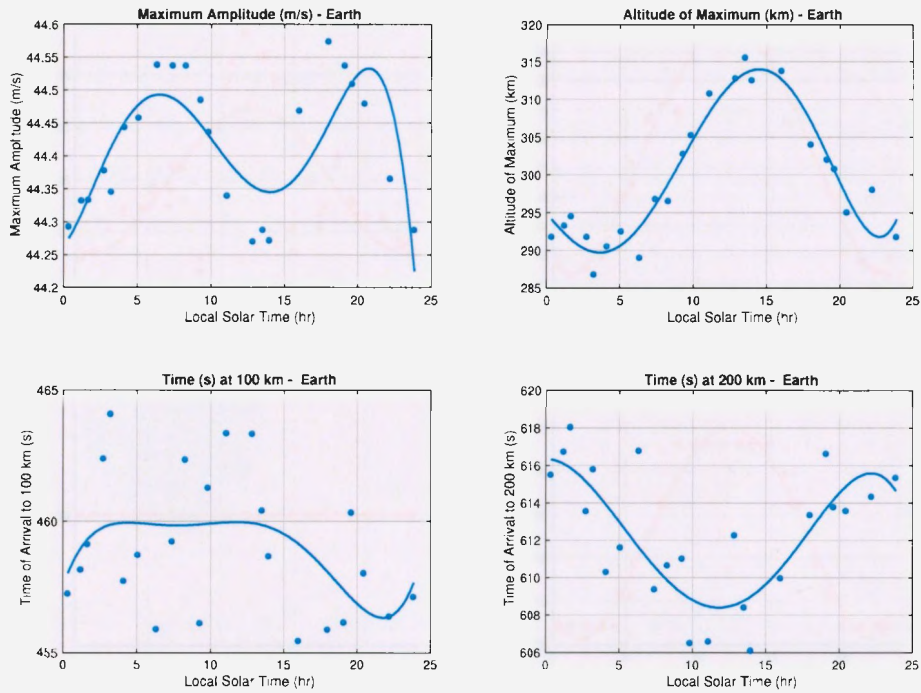


Figure 4.3: Results of the time-of-day sweep for Earth.

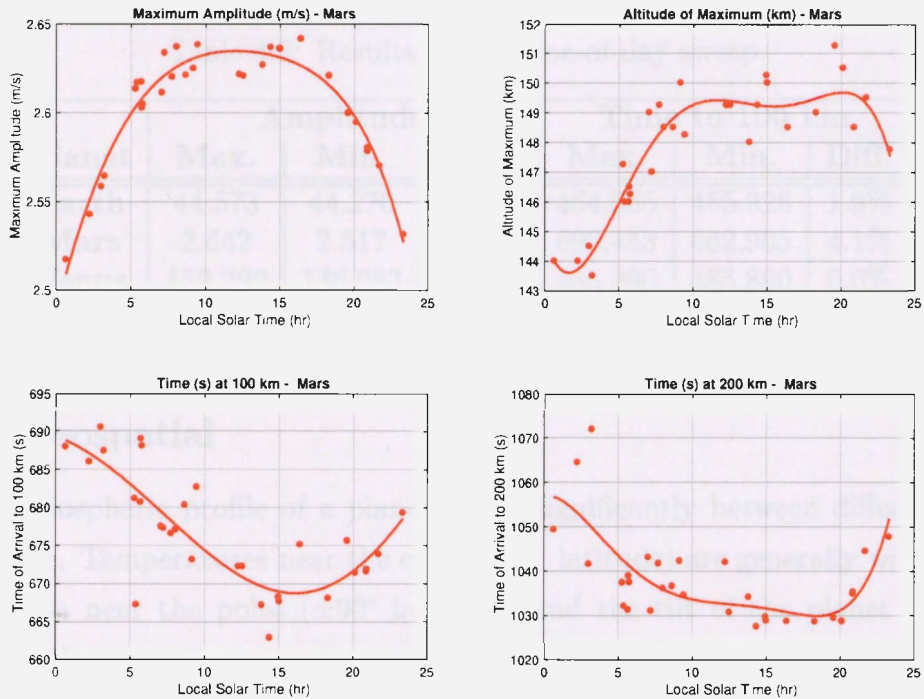


Figure 4.4: Results of the time-of-day sweep for Mars.

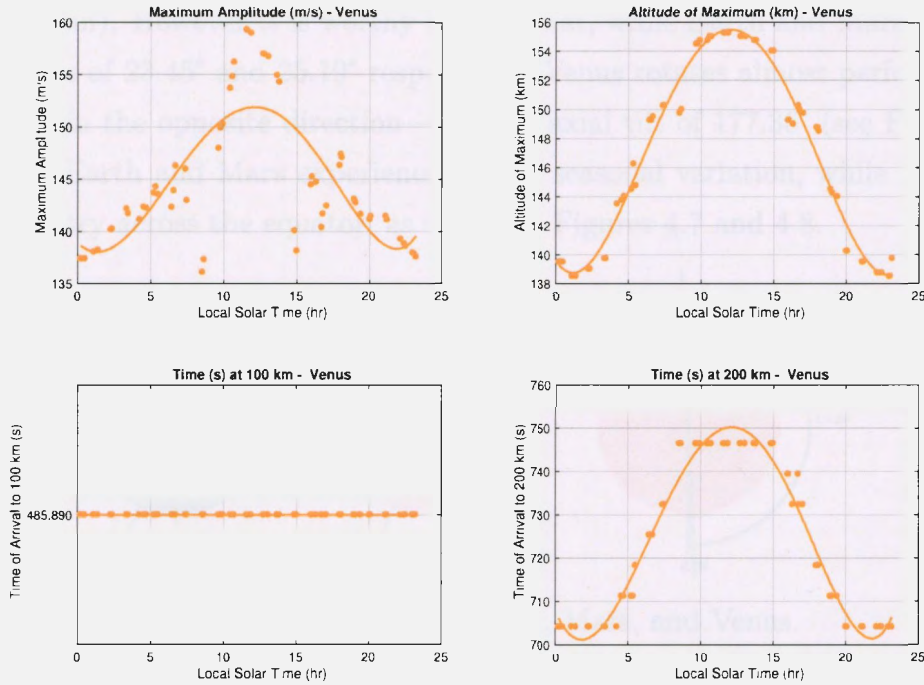


Figure 4.5: Results of the time-of-day sweep for Venus.

Table 4.2: Results of the time-of-day sweep.

Planet	Amplitude			Time to 100 km		
	Max.	Min.	Diff.	Max.	Min.	Diff.
Earth	44.573	44.270	0.68%	464.065	455.328	1.9%
Mars	2.642	2.517	4.8%	690.443	662.905	4.1%
Venus	159.292	136.083	15.7%	485.890	485.890	0.0%

4.1.2 Geospatial

The atmospheric profile of a planet varies significantly between different points on the globe. Temperatures near the equator (0° latitude) are generally warmer than temperatures near the poles ($\pm 90^\circ$ latitude), and the tilt of the planet toward or away from the sun affects temperature and composition as well. During northern hemisphere summer the southern hemisphere experiences winter and vice-versa, leading to temperatures that are warmer on the side experiencing summer (i.e., tilted

toward the sun). However it is worthy to note that, while Earth and Mars have similar axial tilts of 23.45° and 25.19° respectively, Venus rotates almost perfectly on its axis—albeit in the opposite direction—with an axial tilt of 177.36° (see Figure 4.6). As a result, Earth and Mars experience similar seasonal variation, while Venus sees more symmetry across the equator, as shown in Figures 4.7 and 4.8.

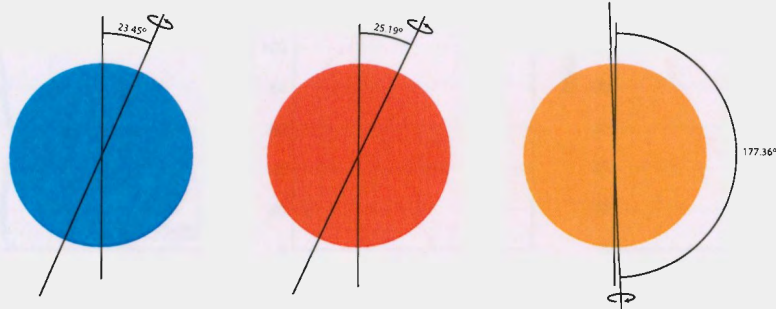


Figure 4.6: Axial tilt of Earth, Mars, and Venus.

Description

In order to explore variation in wave amplitude and travel time with latitude and longitude, a batch of model runs was executed at intervals of 10° latitude, 10° longitude, and 250 meter altitude to a maximum altitude of 500 kilometers—well into the exosphere for all three planets. The constant input parameters of this run set are given in Table 4.3.

Table 4.3: Model input parameters for the geospatial run set.

Parameter	Value	Unit
τ	60	s
t_{center}	240	s
σ	60	s
Amplitude	1×10^{-3}	m/s
Month	2	-
Latitude	-90–90	deg
Longitude	-180–180	deg
LST	12:00	hr
F10.7 (1AU)	150.0	sfu

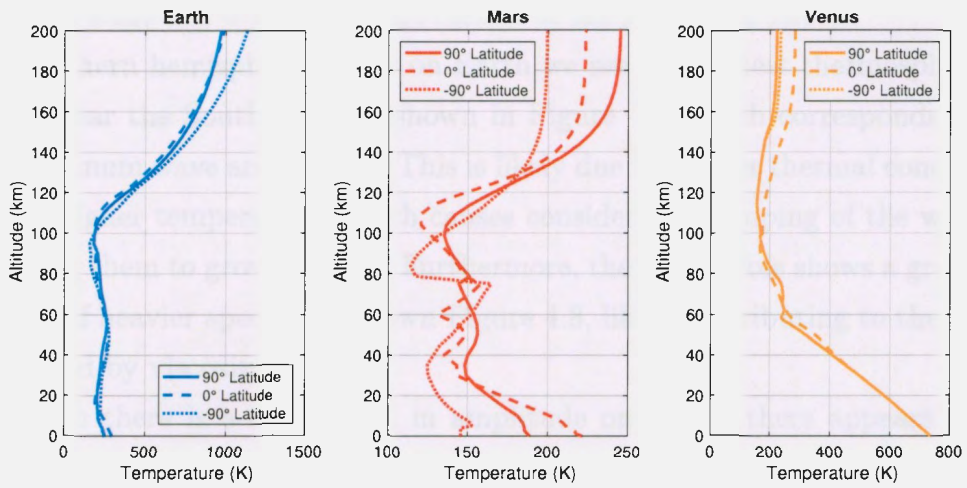


Figure 4.7: Temperature profiles at the equators and poles during the second month.

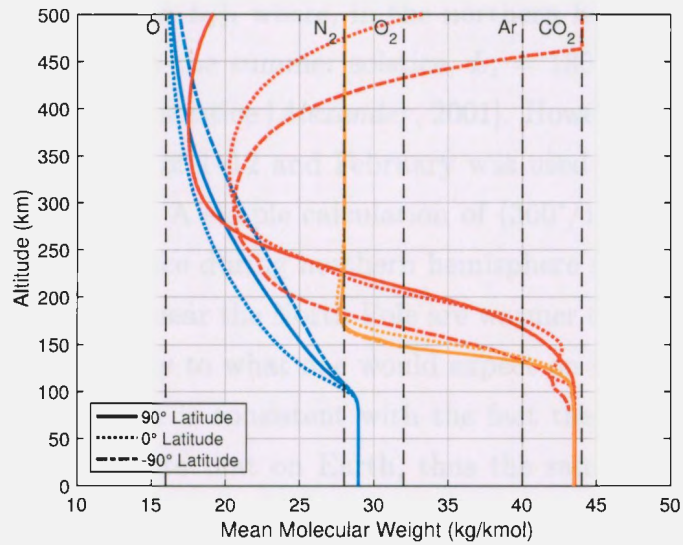


Figure 4.8: Variation of composition at the equators and poles during the second month.

Model Results

Figures 4.9, 4.10, and 4.11 depict the results of the geospatial sweep.

For northern hemisphere winter on Earth we see the highest thermospheric temperatures near the South Pole, as shown in Figure 4.7, which corresponds with the lowest maximum wave amplitudes. This is likely due to greater thermal conduction in regions of higher temperature, which causes considerable damping of the waves thus not allowing them to grow as large. Furthermore, the South Pole shows a greater concentration of heavier species, as shown Figure 4.8, likely contributing to the damping of infrasound by viscosity.

Although there is a clear trend in amplitude on Earth, there appears to be no correlation between geography and wave propagation time. Figure 4.9 shows no obvious distinction or trend, with only ~ 0.3 seconds separating the maximum and minimum arrival times. The “noise” in the results is likely due to small variations in the atmospheric background at low altitudes.

While Mars sees similar seasonal variation to Earth, its “months” are divided differently. The Martian seasons are defined based on the celestial longitude angle of the sun from Mars (denoted L_s), where, in the northern hemisphere, $L_s = 0^\circ$ is the spring equinox, $L_s = 90^\circ$ is the summer solstice, $L_s = 180^\circ$ is the autumn equinox, and $L_s = 270^\circ$ is the winter solstice [Alexander, 2001]. However, MarsGRAM receives an Earth-like month input of 1–12 and February was used as the input for this run set, as shown in Table 4.3. A simple calculation of $(360^\circ/12 \times 2 = 60^\circ)$ shows that Martian February takes place during northern hemisphere spring, which agrees with the fact that temperatures near the North Pole are warmer than those near the South Pole in Figure 4.7 – contrary to what one would expect on Earth in February.

The difference in season is consistent with the fact that the global variation on Mars seems roughly opposite that on Earth, thus the same damping effects are at work albeit at different scales. For example, the Martian thermosphere experiences a much greater change in composition from season to season, thereby likely decreasing viscous damping near the North Pole due to a much lower concentration of CO_2 (a particularly heavy molecule) than found at the equator.

One significant contrast between the results for Earth and Mars is the difference in time of arrival for the Martian waves. While Earth had no distinguishable correlations, Mars shows a clear indication of waves moving slower near the equator and, to a lesser extent, near the North Pole than at southern latitudes. Although these results disagree with what one would expect due to the speed of sound—a warmer atmosphere, such as near the North Pole, should see faster wave propagation—they are likely the result of dissipation. Because the Martian exobase is above 200 km, the waves in the north are likely dissipating before they reach that altitude, and the front of the wave never actually makes it that high; later phase fronts may achieve an altitude of 200 km and register a time of arrival with the model, however this leads to a disconnect in the results.

The Venusian profiles of temperature and composition show little global variation, so it is surprising that there is such a great difference between the highest and lowest maximums—the greatest for all three planets, in fact, as shown in Table 4.4. Venusian amplitude maximums are located near the lower temperatures, so it is likely that thermal conduction plays a significant role in damping propagating waves, especially due to the fact that there is very little variation in composition between the equator and the poles. The extreme difference in amplitudes could simply be due to an extreme difference in conduction, as the temperatures in Venus' lower and middle atmosphere are much higher than on the other two planets. Additionally, as with the diurnal sweep discussed previously, the Venusian waves' time of propagation to 100 km has no sensitivity to the background atmosphere whatsoever due to the thick cloud layer that causes the atmosphere to maintain a uniform surface temperature. Above the clouds, however, there is distinct variation, with waves near the poles traveling faster than those at the equator; this is most likely due to the same phenomenon of wave dissipation before 200 km as is seen in the Martian results, as Venus' exobase is at roughly the same altitude as Mars'.

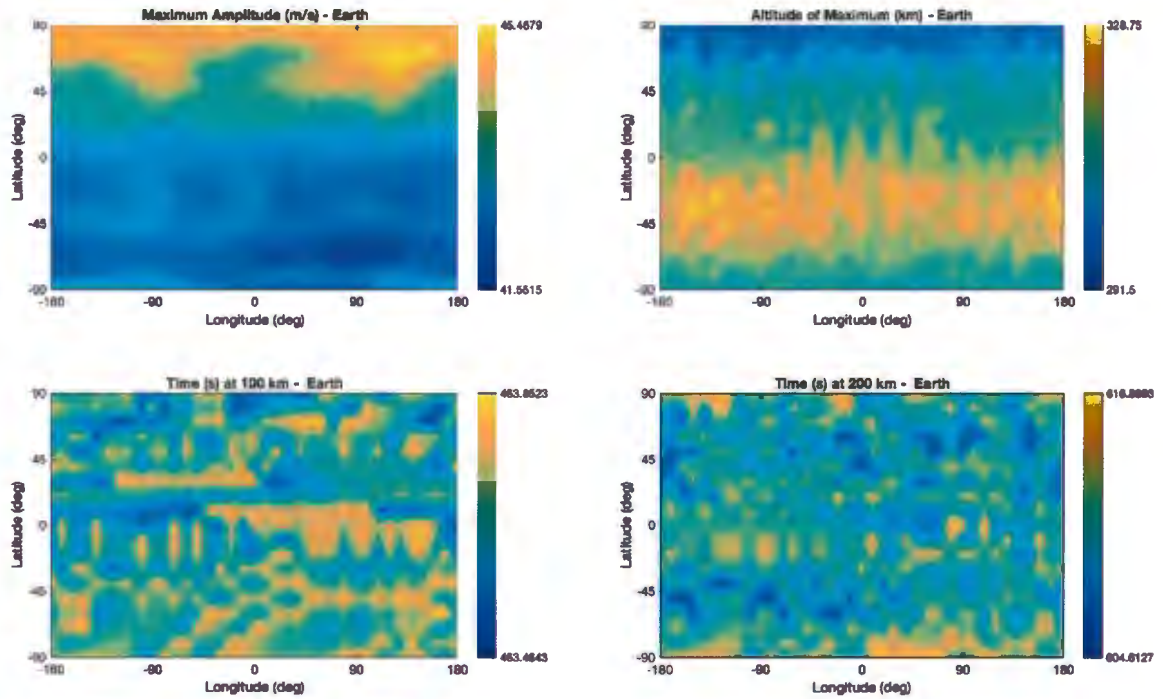


Figure 4.9: Results of the latitude and longitude sweep for Earth.

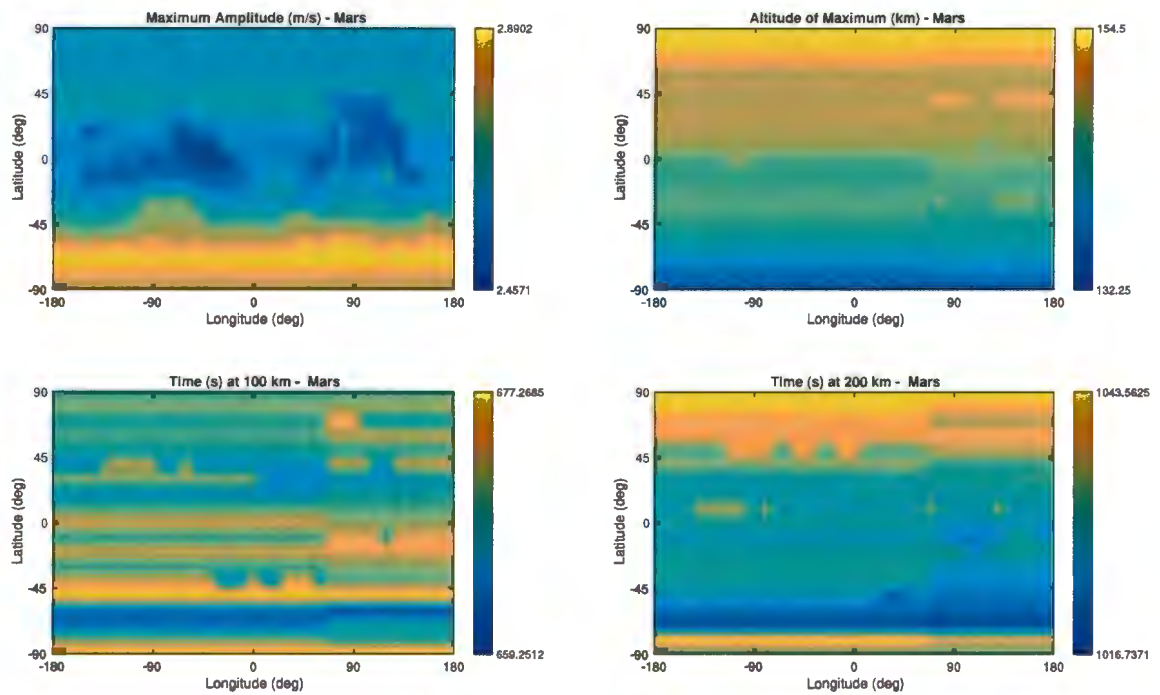


Figure 4.10: Results of the latitude and longitude sweep for Mars.

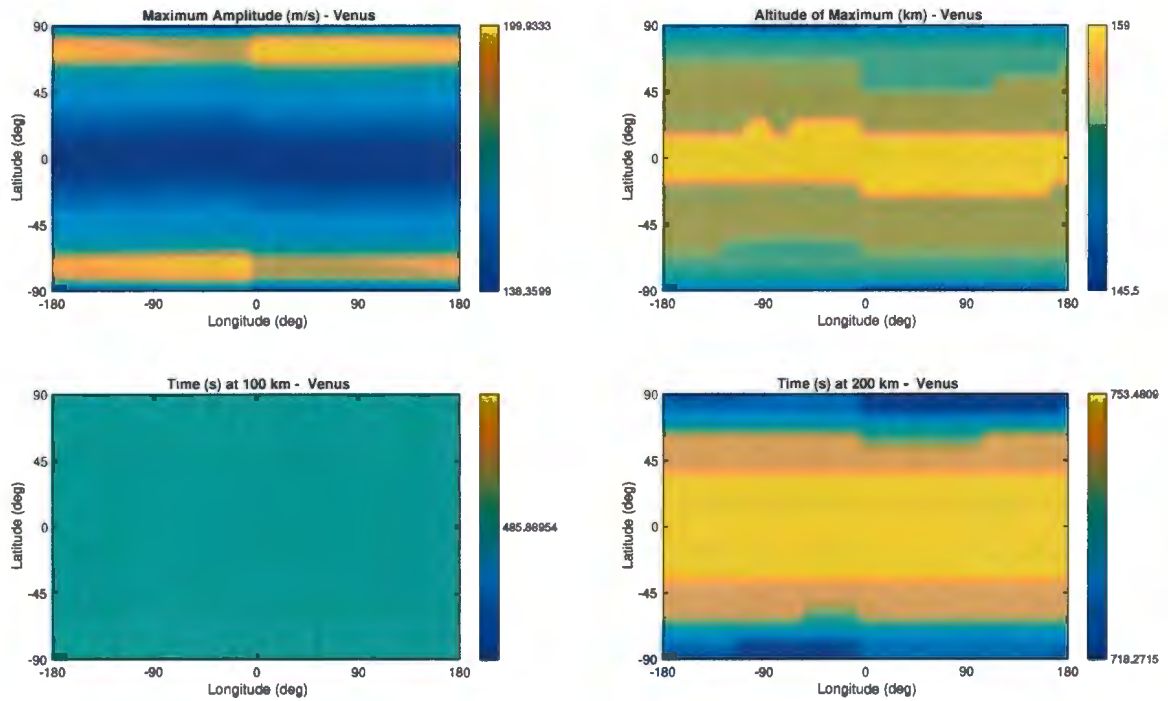


Figure 4.11: Results of the latitude and longitude sweep for Venus.

Table 4.4: Results of the latitude and longitude sweep.

Planet	Amplitude			Time to 100 km		
	Max.	Min.	Diff.	Max.	Min.	Diff.
Earth	45.468	41.552	9.0%	463.852	453.464	2.3%
Mars	2.890	2.457	16.2%	677.269	659.251	2.7%
Venus	199.933	138.360	36.4%	485.890	485.890	0.0%

4.1.3 Solar Effects

As discussed in Chapter 1, the thermosphere is incredibly sensitive to solar conditions due to the nature of its constituents. One significant measurement of solar flux is F10.7 index, or 10.7cm radio emissions, measured in solar flux units (sfu). These emissions originate in the high chromosphere and low corona of the sun, and have historically shown strong correlation with sunspot numbers and space weather events. At a distance of 1AU, the Earth still experiences strong effects due to variations in F10.7 emissions, such as the effect on thermospheric temperature shown in Figure 4.13 and the effect on composition shown in Figure 4.14—in fact, Mars shows an even greater sensitivity, and is one and a half times farther from the sun than the Earth. Because the temperature of the thermosphere is affected by solar activity, it is reasonable to consider that space weather events and off-nominal F10.7 emissions will have an indirect effect on the propagation and dissipation of atmospheric acoustic waves.

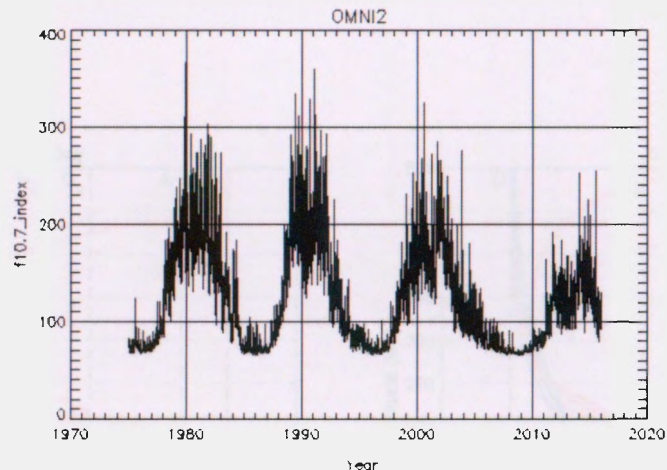


Figure 4.12: Historical values for F10.7 emissions at 1 AU show high, low, and nominal values. Obtained from *NASA Goddard Spaceflight Center* [2016].

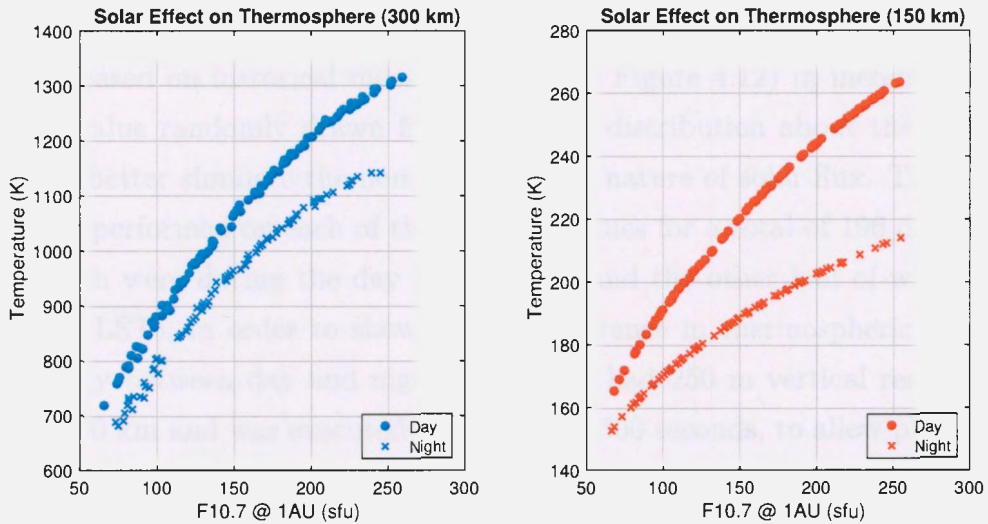


Figure 4.13: Variation of thermospheric temperature on Earth and Mars with solar activity. VenusGRAM 2005 does not account for solar effects, so Venus is excluded from this particular investigation.

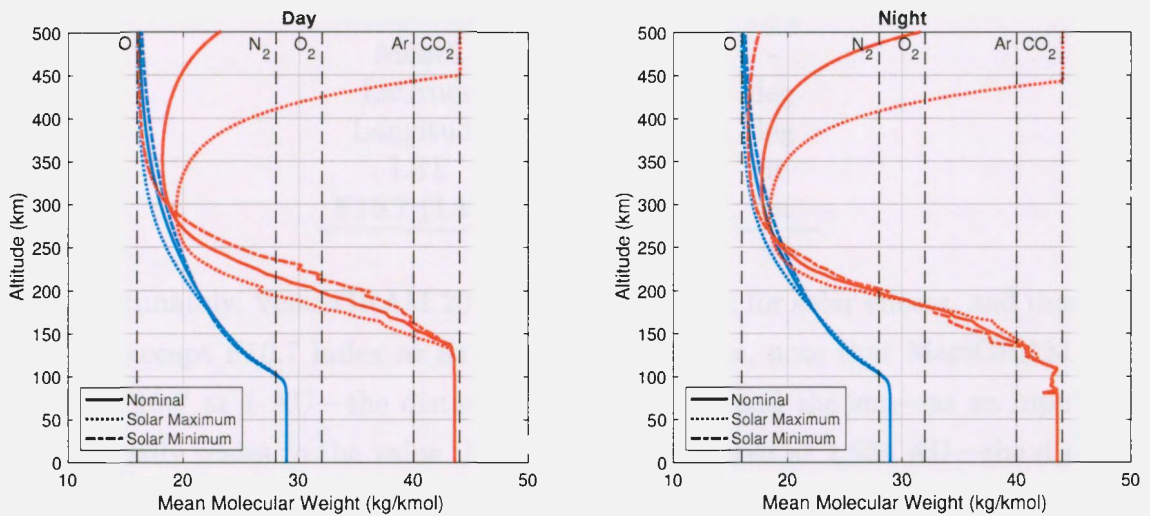


Figure 4.14: Variation of composition on Earth and Mars at nominal, maximum, and minimum solar activity. Venus is excluded.

Description

A batch of runs was performed with values of F10.7 emissions varied from 75.0 to 250.0 sfu (based on historical measurements, see Figure 4.12) in increments of five, with each value randomly drawn from a normal distribution about the input value in order to better simulate the non-deterministic nature of solar flux. Three random draws were performed on each of the centered values for a total of 196 data points—half of which were during the day (12:00 LST) and the other half of which were at night (0:00 LST), in order to showcase the difference in thermospheric response to solar activity between day and night. Each run had 250 m vertical resolution to a height of 500 km and was executed to a time of 1500 seconds, to allow plenty of time and space for the wave to fully grow and dissipate. A full listing of input parameters is provided by Table 4.5.

Table 4.5: Model input parameters for the solar sensitivity run set.

Parameter	Value	Unit
τ	60	s
t_{center}	240	s
σ	60	s
Amplitude	1×10^{-3}	m/s
Month	2	-
Latitude	44.980	deg
Longitude	-93.265	deg
LST	0:00 & 12:00	hr
F10.7 (1AU)	75.0–250.0	sfu

Unfortunately, VenusGRAM 2005 does not account for solar effects, and therefore does not accept F10.7 index as an input. Furthermore, note that MarsGRAM 2010 receives F10.7 at 1 AU—the distance between Earth and the sun—as an input and automatically scales to the value that would be measured at 1.524 AU—the distance between Mars and the sun.

Model Results

Figures 4.15 and 4.16 depict the results of the solar activity sweep.

On Earth the amplitude tracked opposite to increasing temperature, such that the lowest solar activity profiles produced the highest amplitudes in the thermosphere. This is likely due to greater thermal conduction due to higher temperature. For previous results (i.e., the diurnal sweep) we saw higher amplitude with higher temperatures, however the difference in temperatures for that set was not nearly as great as the difference due to solar activity.

In contrast, Mars amplitude trends followed temperature, with daytime, high solar activity profiles producing the highest amplitudes in the thermosphere, as well as a greater difference between day and night. Furthermore, we see a clear distinction in wave travel time between day and night (though it appears to be independent of F10.7), while Earth shows no correlation between travel time and time of day or solar activity at 100 km altitude—differences appear to just be noise; however there is a noticeable trend at 200 km altitude. There is one interesting artifact in the Mars data: an apparent disconnect in the time of arrival to 200 km during the night. This is likely due to the fact that the waves with the lowest amplitudes—low F10.7 and during the night—actually begin to dissipate before 200 km, and therefore the model is detecting a different phase front; this phenomenon appeared in the geospatial sweep as well.

While both planets show a similar difference in temperature with solar activity (Figure 4.13), the composition on Mars is much more sensitive than that of Earth, as shown in Figure 4.14. The carbon dioxide in Mars' thermosphere and exosphere varies significantly with greater solar flux, and therefore more greatly affects the propagation of atmospheric infrasound, as the speed of sound c_s also depends on composition.

Table 4.6: Results of the solar activity sweep.

Planet	Amplitude			Time to 100 km		
	Max.	Min.	Diff.	Max.	Min.	Diff.
Earth	44.688	43.851	1.9%	465.140	455.266	2.2%
Mars	2.651	2.510	5.5%	693.482	665.671	4.1%

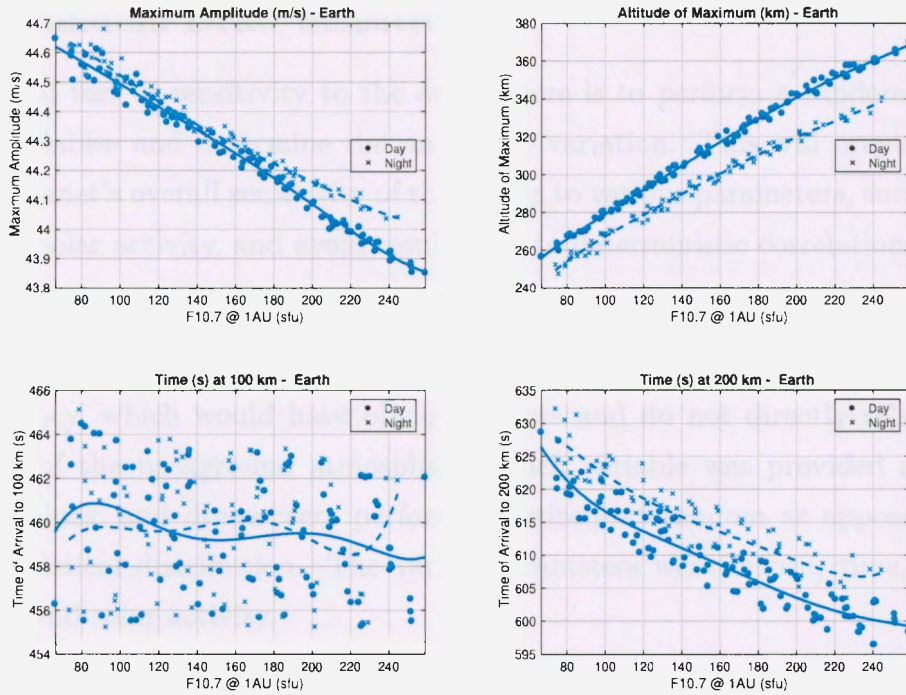


Figure 4.15: Results of the solar activity sweep for Earth.

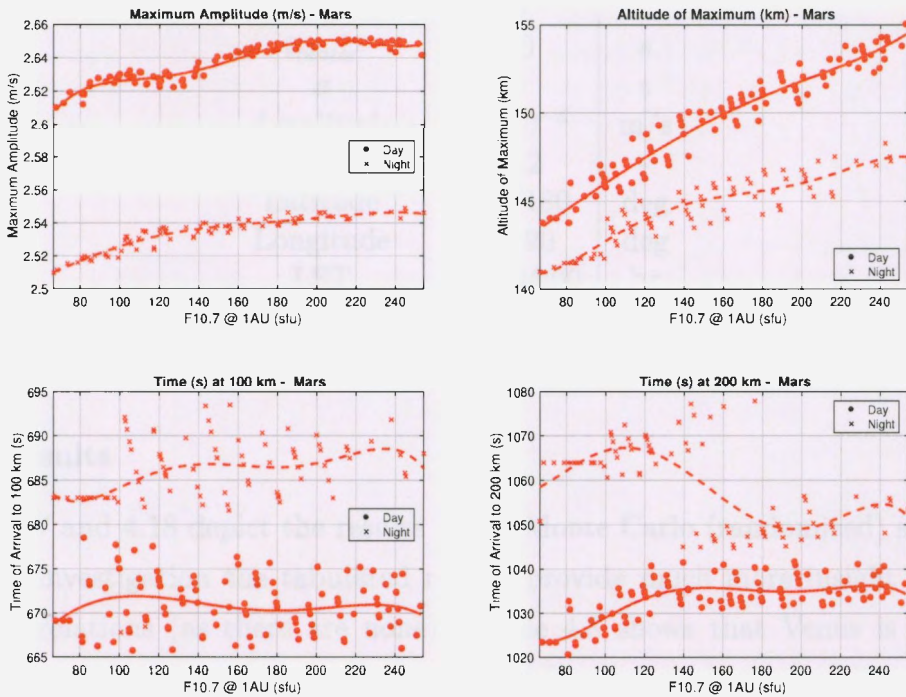


Figure 4.16: Results of the solar activity sweep for Mars.

4.1.4 Random Draw Sensitivity

The final test of sensitivity to the atmosphere is to perform a random draw set over all variables and determine the maximum variation. This will provide insight into each planet's overall sensitivity of the profile to various parameters, such as time, space, and solar activity, and avoid results due to deterministic correlations.

Description

A set of 250 runs is performed with random draws on all variables except for amplitude and frequency, which would have obvious effects and do not directly relate to the sensitivity of the background atmosphere. Each variable was provided a possible range of values, and draws were performed entirely at random as opposed to any sort of statistical distribution. The varied parameters were month, time, latitude, longitude, and solar activity.

Table 4.7: Model input parameters for the random draw set.

Parameter	Value	Unit
τ	60	s
t_{center}	240	s
σ	60	s
Amplitude	1×10^{-3}	m/s
Month	1–12	-
Latitude	-180–180	deg
Longitude	-90–90	deg
LST	0:00–24:00	hr
F10.7 (1AU)	75–250	sfu

Model Results

Figures 4.17 and 4.18 depict the results of the Monte Carlo (randomized) set.

In this investigation the tabulated results provide much more insight than any plotted correlations (as there are none). Table 4.8 shows that Venus is the most sensitive to changes in atmospheric parameters for the maximum amplitude a wave might achieve, with Mars second and Earth last. This is not surprising based on the

results from the previous several studies; the heavy CO₂ in the atmospheres of Mars and Venus can have a large impact with little change, whereas Earth's profiles tended to remain fairly consistent regardless of conditions.

For time of propagation we see Mars on the top with Venus second and Earth third. Again, this is not surprising, as we saw very little correlation in the time of arrival plots for Earth. Though it may be worth making the comment that, because Earth's exobase is higher than that on Mars and Venus, the time of arrival may not be comparatively sensitive for the same altitudes. This is something to investigate further in the future. Furthermore, the seemingly sporadic nature of the Venusian time of propagation results in Figure 4.18 is likely due to the fact that Venus' atmosphere does not vary below 100 km, and thus this histogram is only representing variation present between 100 and 150 km. In contrast, the other two planets see greater variation at low altitudes, leading to more diverse data.

Table 4.8: Results of the random draw set.

Planet	Amplitude			Time to 150 km		
	Max.	Min.	Diff.	Max.	Min.	Diff.
Earth	45.309	41.292	11.5%	556.430	535.762	3.8%
Mars	2.855	2.292	21.9%	917.399	853.438	7.2%
Venus	199.685	127.248	44.3%	676.020	640.811	5.4%

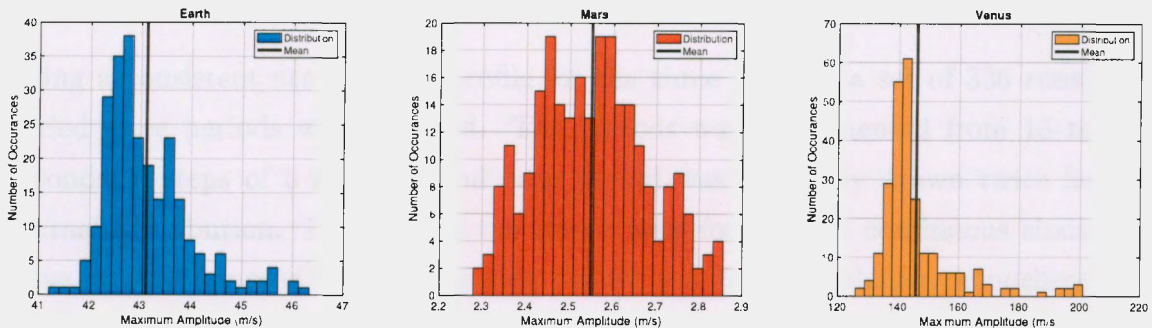


Figure 4.17: Distribution of maximum amplitude over a series of 250 random draws.

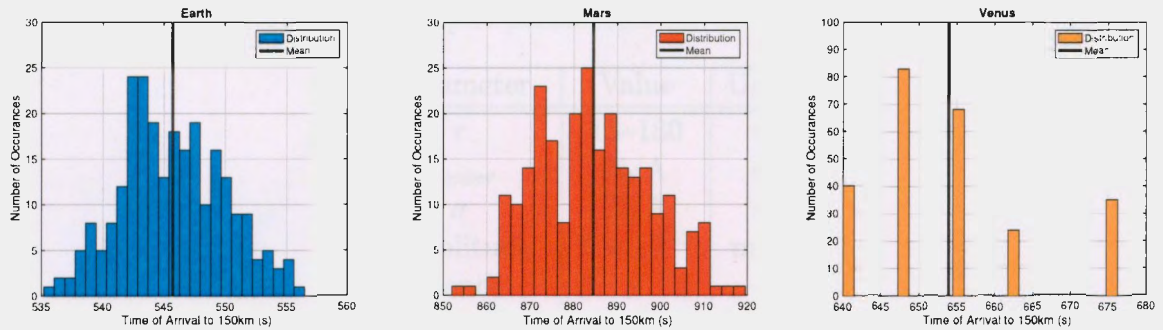


Figure 4.18: Distribution of time of arrival to 150 km over a series of 250 random draws.

4.2 Variation of the Wave

4.2.1 Frequency Sweep

While the majority of waves considered in this thesis have had a period of 60 seconds (which is a reasonable period for an infrasonic wave), it is important to investigate the propagation and dissipation of a larger part of the infrasonic spectrum. Waves generated by the wide variety of natural and artificial sources have a wide variety of source frequencies (and amplitudes, discussed next), and, as a result, grow to different amplitudes in the upper atmosphere.

Description

Using a consistent atmospheric profile for the three planets, a set of 336 runs with varied wave periods was executed. The periods were incremented from 15 to 180 seconds in steps of 5 seconds, and each period was randomly drawn twice from a normal distribution. For this set the waves were forced as a continuous sinusoidal wave form as opposed to a propagating packet in order to produce a monochromatic wave.

Model Results

Figure 4.19 depicts the results of the frequency sweep.

Table 4.9: Model input parameters for the frequency sweep.

Parameter	Value	Unit
τ	15–180	s
t_{center}	N/A	s
σ	N/A	s
Amplitude	1×10^{-3}	m/s
Month	2	-
Latitude	44.980	deg
Longitude	-93.265	deg
LST	12:00	hr
F10.7 (1AU)	150.0	sfu

Each planet shows a nearly linear trend where larger period waves achieve greater amplitudes. This is expected due to the fact that a longer period results in a longer wavelength, and larger scale waves are less easily diffused. Using a linear best fit function in MATLAB[®], an equation of best fit was determined for each planet. This fit could be used to reasonably extrapolate values outside of the simulated domain in order to determine a wave’s maximum amplitude. The relations are:

$$a_{max} = 1.087\tau - 11.747 \quad \text{for Earth}$$

$$a_{max} = 0.060\tau - 0.545 \quad \text{for Mars}$$

$$a_{max} = 2.533\tau + 1.403 \quad \text{for Venus}$$

where a_{max} is the maximum amplitude and τ is the initial wave period. There is a small amount of error associated with these fits, as the function should cross through the origin (i.e., the zeroth-order term should be zero). This error is mostly representative of limitations due to model resolution—there are no data points at extremely low periods (i.e., 1–5 s)—and the fact that a linear function does not perfectly fit the data (though the trend is clearly linear). Nonetheless, these relations provide a reasonable fit, which is clearly shown by Figure 4.19.

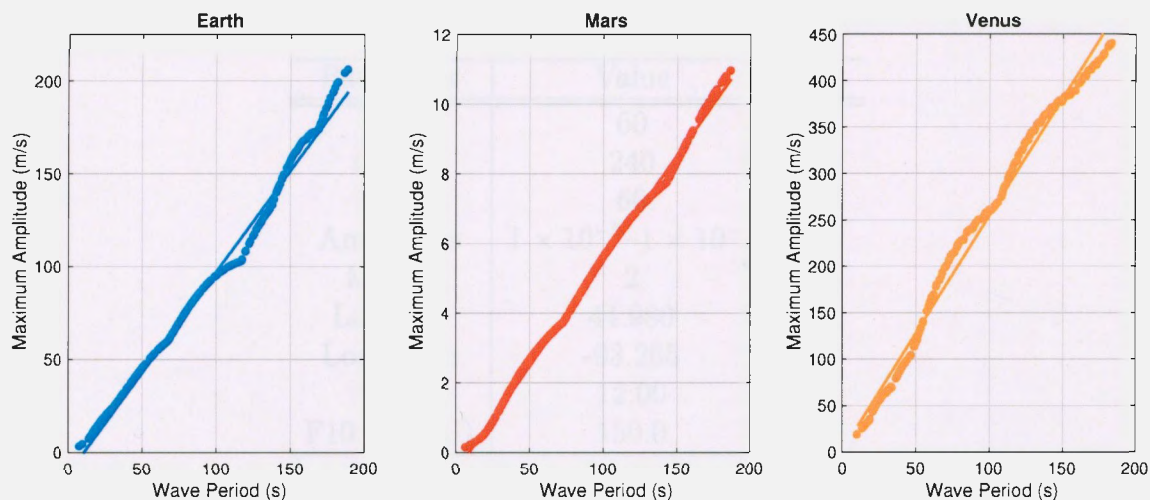


Figure 4.19: Maximum wave amplitude on Earth, Mars, and Venus for a wide span of wave periods.

4.2.2 Amplitude Sweep

In addition to frequency, source amplitude is the other major parameter that does not come from the background atmosphere itself. Because potential sources of infrasound span a wide range of amplitudes (i.e., earthquakes of different magnitudes) it is essential to understand the relationship between initial and maximum amplitude if detection is to be possible.

Description

A set of runs spanning amplitudes between 1×10^{-5} and 1×10^{-1} was executed in order to show the correlation between initial and maximum wave amplitude. This range was selected based on what the model could reasonably support; note that for Venus the model failed considerably sooner than for Earth and Mars due to the relative size of the waves.

Table 4.10: Model input parameters for the amplitude sweep.

Parameter	Value	Unit
τ	60	s
t_{center}	240	s
σ	60	s
Amplitude	$1 \times 10^{-5} - 1 \times 10^{-1}$	m/s
Month	2	-
Latitude	44.980	deg
Longitude	-93.265	deg
LST	12:00	hr
F10.7 (1AU)	150.0	sfu

Model Results

Figure 4.20 shows the correlation between initial and maximum amplitude on Earth, Mars, and Venus for a uniform atmospheric profile.

Interestingly, all three planets seem to show slightly different correlations between initial and maximum amplitude. Using a best fit polynomial function in MATLAB[®], an equation of best fit was determined for each planet. This fit could be used to reasonably extrapolate values outside of the simulated domain in order to determine a wave's maximum amplitude. The relations are:

$$a_{max} = (1.56 \times 10^6)a_0^3 - (4.13 \times 10^5)a_0^2 + (3.70 \times 10^4)a_0 + 0.585 \quad \text{for Earth}$$

$$a_{max} = (4.34 \times 10^3)a_0^3 + (1.10 \times 10^3)a_0^2 + (2.02 \times 10^3)a_0 + 1.055 \quad \text{for Mars}$$

$$a_{max} = (3.15 \times 10^{10})a_0^3 - (1.80 \times 10^8)a_0^2 + (3.10 \times 10^5)a_0 - 2.505 \quad \text{for Venus}$$

where a_{max} is the maximum amplitude and a_0 is the source amplitude. Like with the frequency sweep, the presence of a zeroth order term indicates a small amount of error with the fit.

The results are the most interesting for the Earth, which sees a transition from a linear increase at low source amplitudes to a nonlinear increase at higher amplitudes, and finally saturates at very large amplitudes.

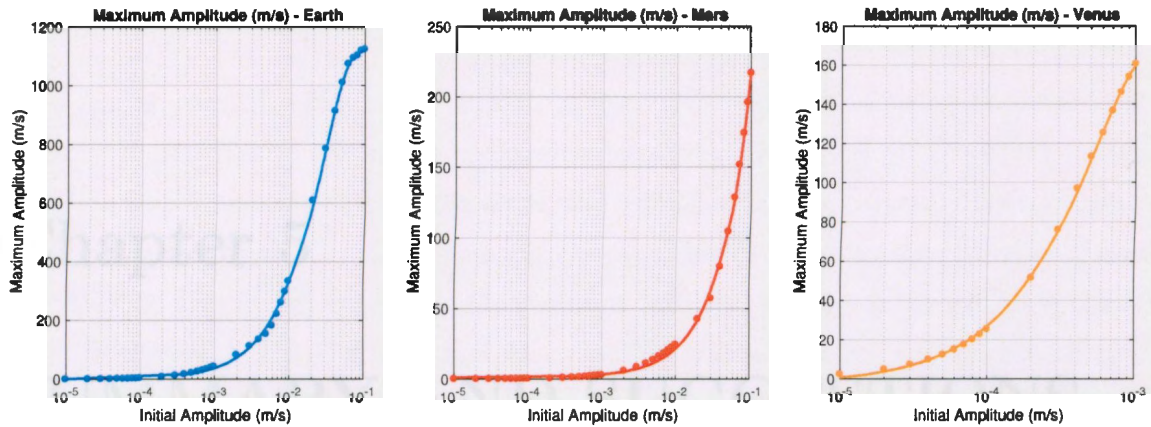


Figure 4.20: Maximum wave amplitude on Earth, Mars, and Venus for a wide span of source amplitudes.

4.3 Chapter Summary

In order to explore the propagation and dissipation of atmospheric infrasound on terrestrial planets, several parameter sweeps were performed, as discussed in this chapter. Variations were made to the ambient atmosphere as well as the wave forcing in order to both exercise the full capability of the model and perform a thorough comparative investigation of the characteristics of infrasound on Earth, Mars, and Venus. This chapter has outlined, in detail, the investigations performed, their approach, and their results.

Chapter 5

SUMMARY AND SUGGESTIONS FOR FUTURE WORK

Throughout Chapter 4 we saw the following general trends: infrasound on Earth shows the greatest amplitudes under conditions with lower temperatures, while Mars and Venus tended toward the opposite. As previously stated, this is likely due to the innate dependence of acoustic waves on two main variables—temperature and composition—and the fact that these have different levels of sensitivity between the three planets. On Earth the profile did not appear very sensitive to changes in time, space, or solar conditions, while Mars and Venus saw greater changes over the sweeps. The common factor between these two planets is their carbon dioxide atmosphere, which is significantly heavier than Earth's nitrogen and oxygen atmosphere and more susceptible to variations as a result. When energy is imparted on carbon dioxide, such as by the sun, it rises and significantly disrupts the chemistry of the thermosphere and exosphere—the regions of the atmosphere that play the greatest role in the growth and dissipation of propagating waves.

5.1 Wave Detectability

One major goal of infrasound research is detectability, namely using detectable infrasonic signatures to identify and characterize earthquakes and other seismic events. While acoustic waves of varying spectra and amplitudes have certainly been detected on Earth, there have been no measurements yet taken of infrasound on Mars or Venus. The GOCE satellite discussed by *Garcia et al.* [2013] orbits in low Earth orbit (LEO) at an altitude of 270 km, and is able to detect waves with velocities of ~ 10 m/s. Furthermore, a report published by *Stevenson et al.* [2015] suggests the deployment of a balloon in the Venusian atmosphere above the cloud layer (~ 50 – 55 km) in order to detect seismic events via propagating infrasound. At this altitude, we believe that waves greater than 3 – 5 m/s would likely be detectable, which, from the results presented in Chapter 4, are amplitudes that are reasonable. While there has been some thought within the aeronomy community regarding executing such an experiment, there is little established precedent from which to determine a detectability threshold. For the purposes of this thesis, we hypothesize a threshold compressional velocity of approximately 1–2% the speed of sound at thermospheric altitudes.

Based on the results presented in this thesis, Martian waves with source amplitudes around 0.01 m/s or larger for a sixty-second period are able to attain amplitudes exceeding 20 m/s, and are therefore likely to be detectable at altitudes above 120 km and possibly at lower altitudes as well. However, smaller waves may also be detectable, as the hypothesized threshold of detectability in the Martian thermosphere is only between 2 – 3 m/s. On Earth, source amplitudes as small as 10^{-4} produce detectable waves in the one-dimensional model, which indicates that, for even larger source amplitudes, waves with compressional velocities on the order of 100 – 200 m/s or greater are likely to exist. For most large sources with amplitudes exceeding 5×10^{-4} m/s—depending on atmospheric conditions—a sixty-second wave would be detectable in the middle and upper-atmosphere, and a wave with a period greater than 100 seconds would also be detectable even for amplitudes a full order of magnitude smaller. Finally, Venusian waves with source amplitudes greater than 10^{-4} m/s and periods of roughly tens of seconds generated by large sources are readily detectable. Venus'

dense atmosphere below 100 km causes significant growth before the waves reach the thermosphere, at which point the speed of sound, and, thus, the detectability threshold, has dropped significantly. Figure 5.1 shows the propagation over time of a wave on each planet that attains what is believed to be a detectable amplitude.

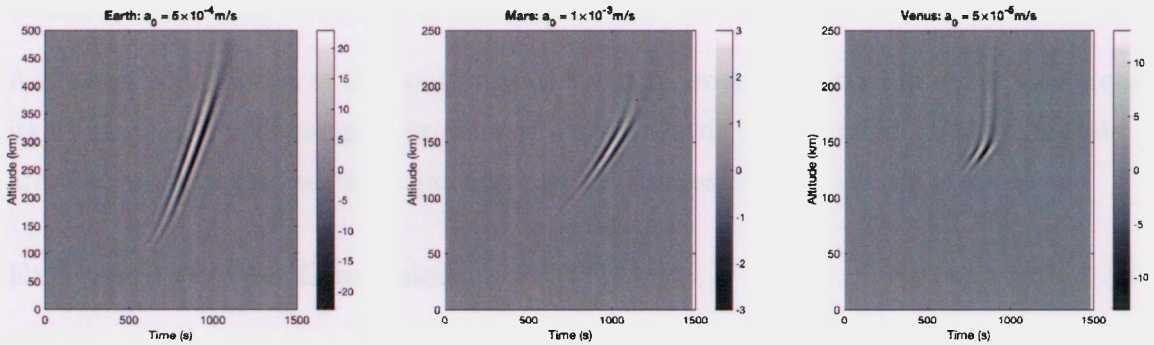


Figure 5.1: Propagation of a sixty-second wave on each of the planets at night during nominal solar conditions, with source amplitudes selected to produce a wave around the hypothesized lower limit of detectability.

5.2 Potential Future Investigations

There are many possible studies that could utilize this robust acoustics model. One such extension for the future is the implementation of realistic source forcings, such as those from earthquakes, volcanos, and explosions. After initial investigation, it would be useful to determine how real waves are forced and would propagate through planetary atmospheres. This could be done via an analytical forcing function, similar to those used by *Zettergren and Snively* [2015]. The ability to detect seismic events on other planets using orbital sensors has the potential to provide valuable insight into the geology and seismology of terrestrial worlds.

This model could also be coupled with others, for example to force waves via a seismic forcing model, or explore perturbations of ions and electrons in the ionosphere. There has been some work done in adding the perturbation of electrons to the model, however there is little known about the ionospheres of Mars and Venus, so from a comparative aeronomy perspective this feature is not feasible to include currently.

Any of these extensions would provide valuable insight into the propagation of acoustic waves on other worlds, and enhance our understanding of other planetary atmospheres.

5.2.1 Further Model Development

A natural progression of this work would be to improve the model in order to increase its utility for a wider range of problems. Two methods for extension to two dimensions are discussed in this section that account for the realistic geometry of sources.

Extension to Two Dimensions

The two-dimensional system of nonlinear Euler equations with gravity is given by [e.g., *LeVeque*, 2002, pp. 431]:

$$\frac{\partial}{\partial t} \begin{bmatrix} \rho \\ \rho v_x \\ \rho v_z \\ E \end{bmatrix} + \frac{\partial}{\partial x} \begin{bmatrix} \rho v_x \\ \rho v_x^2 + p \\ \rho v_x v_z \\ v_x(E + p) \end{bmatrix} + \frac{\partial}{\partial z} \begin{bmatrix} \rho v_z \\ \rho v_x v_z \\ \rho v_z^2 + p \\ v_z(E + p) \end{bmatrix} = \begin{bmatrix} 0 \\ 0 \\ -\rho g \\ -\rho v_z g \end{bmatrix} \quad (5.1)$$

This system may be implemented by utilizing a two-dimensional advection method, some of which are discussed by *Potter* [1973, pp. 72–75]. A two-dimensional model would provide greater insight into the propagation of acoustic waves from more realistic sources, but would be significantly more computationally intensive than the one-dimensional model.

Spherical Acoustics

Rather than implementing a full two-dimensional solution, which adds significant computation time due to the additional terms and equation, one strategy involves utilizing symmetry in order to reduce a two- or three-dimensional problem into one and utilize standard one-dimensional numerical methods to obtain the solution. *LeVeque* [2002, pp. 433–434] discusses the transformation of the system of one-dimensional

Euler equations, given by Equations (2.5), (2.6), and (2.7) into polar or spherical coordinates. For example, by assuming no velocity or variation in the azimuthal direction, the system of Euler equations with cylindrical radial symmetry becomes:

$$\frac{\partial \rho}{\partial t} + \frac{\partial(\rho v_r)}{\partial r} = -\frac{1}{r}(\rho v_r) \quad (5.2)$$

$$\frac{\partial(\rho v_r)}{\partial t} + \frac{\partial(\rho v_r^2 + p)}{\partial r} = -\frac{1}{r}(\rho v_r^2) \quad (5.3)$$

$$\frac{\partial E}{\partial t} + \frac{\partial((E + p)v_r)}{\partial r} = -\frac{1}{r}((E + p)v_r) \quad (5.4)$$

where r is the radial distance and v_r is the radial velocity. Note that this system utilizes the same equation of state given by Equation (2.8). This system would be fairly easy to implement in the future, and would provide insight into how waves attenuate as they move away from their source, due to the dependence on $1/r$. Note that a two- or three-dimensional simulation is still required for realistic source geometries, but that many real sources can be approximated as planar, cylindrical, or spherical for one-dimensional vertical propagation.

5.3 Conclusions

This thesis has presented the development and validation of a fully nonlinear compressible atmospheric acoustics model valid for different planetary atmospheres. Using a two-step Lax-Wendroff method to solve the system of Euler advection equations with gravity and an implicit backward Euler method to solve for time-split diffusion equations representing viscosity and thermal conduction, this model is validated for the simulation of propagating infrasonic acoustic waves. In this investigation we explore the three major terrestrial planets in our solar system—Earth, Mars, and Venus. Following a detailed analysis of comparative aeronomy between these worlds, several different acoustic waves were launched in each of the three atmospheres to validate the model and examine differences in propagation and dissipation. Validation was performed for the following major quantitative parameters: speed, wavelength, and

attenuation; all were found to perform as expected on each of the three worlds.

Throughout this study we have been able to make several conclusions about the propagation and dissipation, due to classical viscous processes, of infrasonic—periods greater than ten seconds—atmospheric acoustic waves on Earth, Mars, and Venus. As expected, Martian acoustic waves travel much slower and dissipate much more rapidly than their counterparts on Earth or Venus, while Venusian acoustic waves possess the opposite characteristics, particularly at low altitudes. While Mars' profile is quasi-isothermal, thus inducing little change throughout propagation, the temperature profiles of Earth and Venus undergo several changes, leading to varying wave speeds with altitude. The main characteristic of Earth's atmosphere is its extreme thermospheric heating above 100 km, where waves accelerate due to higher speed of sound. The opposite occurs on Venus, with a constant cooling, which occurs above tropopause, causing waves to slow down to nearly Martian acoustic speeds.

Chapter 4 presented parametric sweeps, which highlight key atmospheric parameters that support the greatest growth of infrasonic acoustic waves in the atmospheres of Earth, Mars, and Venus. We have found that, on Earth, lower temperatures facilitate greater amplitudes at high altitudes, whereas Mars and Venus see the opposite trend. Overall estimates of detectability indicate that vertically propagating infrasonic acoustic waves are easily detectable in the upper atmospheres of Earth and Venus, and that large, strong waves are potentially detectable in the atmosphere of Mars as well. Because seismic events on terrestrial planets are able to generate infrasound, these findings lend credibility to the proposal that earthquakes and similar large events may be detectable from orbit using infrasonic sensors.

Bibliography

- Alexander, M. (2001), Mars transportation environment definition document, *Tech. Rep. NASA/TM-2001-210935*, National Aeronautics and Space Administration.
- Balachandran, N. K. (1979), Infrasonic signals from thunder, *Journal of Geophysical Research*, *84*(C4), 1735–1745.
- Bass, H. E., and J. P. Chambers (2001), Absorption of sound in the martian atmosphere, *Journal of the Acoustical Society of America*, *106*(6), 3069–3071.
- Beddard, A. J., and T. M. Georges (2000), Atmospheric infrasound, *Acoustics Australia*, *28*(2), 47–52.
- Besset, C., and E. Blanc (1994), Propagation of vertical shock waves in the atmosphere, *Journal of the Acoustical Society of America*, *95*(4), 1830–1839.
- Blackstock, D. T. (2000), *Fundamentals of Physical Acoustics*, Wiley-Interscience.
- Blanc, E. (1985), Observations in the upper atmosphere of infrasonic waves from natural or artificial sources: A summary, *Annales Geophysicae*, *3*(6), 673–687.
- Borucki, W. J. (1982), Comparison of venusian lightning observations, *Icarus*, *52*(2), 354–364.
- Borucki, W. J., R. L. McKenzie, C. P. McKay, N. D. Duong, and D. S. Boac (1985), Spectra of simulated lightning on venus, jupiter, and titan, *Icarus*, *64*(2), 221–232.

- Bougher, S. W., R. G. Roble, and T. Fuller-Rowell (2002), Simulations of the upper atmospheres of the terrestrial planets, in *Atmospheres in the Solar System: Comparative Aeronomy, Geophysical Monograph Series*, vol. 130, edited by M. Mendillo, A. F. Nagy, and J. H. Waite, pp. 261–288, AGU.
- Bougher, S. W., P.-L. Blelly, M. Combi, J. L. Fox, I. Mueller-Wodarg, A. Ridley, and R. G. Roble (2008), Neutral upper atmosphere and ionosphere modeling, in *Comparative Aeronomy, Space Science Series of ISSI*, vol. 29, edited by A. F. Nagy, A. Balogh, T. E. Cravens, M. Mendillo, and I. Mueller-Wodarg, pp. 107–141, Springer.
- Bullock, M. A., and D. H. Grinspoon (2013), The atmosphere and climate of venus, in *Comparative Climatology of Terrestrial Planets*, edited by S. J. Mackwell, A. A. Simon-Miller, J. W. Harder, and M. A. Bullock, The University of Arizona Space Science Series, pp. 19–54, The University of Arizona Press.
- Coffey, J. (2008), Mars dust storms, *Universe Today*.
- de Larquier, S. (2010), Finite-difference time-domain modeling of infrasound from pulsating auroras and comparison with recent observations, Master’s thesis, The Pennsylvania State University.
- Drob, D. P., J. M. Picone, and M. Garcés (2003), Global morphology of infrasound propagation, *Journal of Geophysical Research*, 108(D21), 4680.
- Farges, T., and E. Blanc (2010), Characteristics of infrasound from lightning and sprites near thunderstorm areas, *Journal of Geophysical Research*, 115(A00E31).
- Farrelly, F. A., A. Petri, L. Pitolli, and G. Pontuale (2004), In situ acoustic-based analysis system for physical and chemical properties of the lower martian atmosphere, *Planetary and Space Science*, 52(1), 125–131.
- Fischer, G., D. A. Gurnett, and Y. Yair (2011), Extraterrestrial lightning and its past and future investigation, in *Lightning: Properties, Formation and Types*, edited

- by M. D. Wood, *Earth Sciences in the 21st Century*, pp. 19–38, Nova Science Publishers.
- Fjeldbo, G., A. J. Kliore, and V. R. Eshleman (1971), The neutral atmosphere of venus as studied with the mariner v radio occultation experiments, *The Astronomical Journal*, 76(2), 123–140.
- Forbes, J. M. (2002), Wave coupling in terrestrial planetary atmospheres, in *Atmospheres in the Solar System: Comparative Aeronomy, Geophysical Monograph Series*, vol. 130, edited by M. Mendillo, A. F. Nagy, and J. H. Waite, pp. 171–190, AGU.
- Foster, A., and F. Nimmo (1996), Comparisons between the rift systems of east africa, earth and beta regio, venus, *Earth and Planetary Science Letters*, 143(1), 183–195.
- Fritts, D. C., and M. J. Alexander (2003), Gravity wave dynamics and effects in the middle atmosphere, *Reviews of Geophysics*, 41(1), 1003.
- Garcés, M. A., R. A. Hansen, and K. G. Lindquist (1998), Traveltimes for infrasonic waves propagating in a stratified atmosphere, *Geophysical Journal International*, 135(1), 255–263.
- Garcia, R., P. Lognonné, and X. Bonnin (2005), Detecting atmospheric perturbations produced by venus quakes, *Geophysical Research Letters*, 32(L16205).
- Garcia, R. F., P. Drossart, G. Piccioni, M. López-Valverde, and G. Occhipinti (2009), Gravity waves in the upper atmosphere of venus revealed by co2 nonlocal thermodynamic equilibrium emissions, *Journal of Geophysical Research*, 114(E00B32).
- Garcia, R. F., S. Bruinsma, P. Lognonné, E. Doornbos, and F. Cachoux (2013), Gocc: The first seismometer in orbit around the earth, *Geophysical Research Letters*, 40(5), 1015–1020.
- González-Galindo, F., F. Forget, M. A. I. Coll, and M. Á. López-Valverde (2008), The martian upper atmosphere, in *Lecture Notes and Essays in Astrophysics I*, edited by A. Ulla, pp. 151–162, CreateSpace Independent Publishing Platform.

- Gossard, E. E., and W. H. Hooke (1975), *Waves in the Atmosphere*, Elsevier Scientific.
- Hanford, A. D., and L. N. Long (2009), The direct simulation of acoustics on earth, mars, and titan, *Journal of the Acoustical Society of America*, *125*(2), 640–650.
- Heale, C. J., and J. B. Snively (2015), Gravity wave propagation through a vertically and horizontally inhomogeneous background wind, *Journal of Geophysical Research*, *120*(12), 5931–5950.
- Hickey, M. P., G. Schubert, and R. L. Walterscheid (2001), Acoustic wave heating of the thermosphere, *Journal of Geophysical Research*, *106*(A10), 21,543–21,548.
- Hoffman, J. D. (2001), *Numerical Methods for Engineers and Scientists*, 2 ed., Marcel Dekker, Inc.
- Holton, J. R., P. H. Haynes, M. E. McIntyre, A. R. Douglass, R. B. Rood, and L. Pfister (1995), Stratosphere-troposphere exchange, *Reviews of Geophysics*, *33*(4), 403–439.
- Jacobson, M. Z. (2005), *Fundamentals of Atmospheric Modeling*, 2 ed., Cambridge University Press.
- Johnson, J. B. (2003), Generation and propagation of infrasonic airwaves from volcanic explosions, *Journal of Volcanology and Geothermal Research*, *121*(1), 1–14.
- Justh, H. L., and K. L. Burns (2013), Mars-GRAM 2010: Additions and Resulting Improvements, presented at 10th International Planetary Probe Workshop (IPPW-10); San Jose, CA United States; 17–21 June.
- Justh, H. L., C. Justus, and V. W. Keller (2006), Global reference atmospheric models, including thermospheres, for mars, venus, and earth, presented at AIAA/AAS Astrodynamics Specialist Conference and Exhibit; Keystone, CO United States; 21–24 August 2006.
- Kalkofen, W., P. Rossi, G. Bodo, and S. Massaglia (1994), Propagation of acoustic waves in a stratified atmosphere I, *Astronomy and Astrophysics*, *284*, 976–984.

- Kinsler, L. E., A. R. Frey, A. B. Coppens, and J. V. Sanders (2000), *Fundamentals of Acoustics*, 4 ed., John Wiley and Sons, Inc.
- Knabe, W. E. (1969), Theoretical study of the generation of infrasonic waves in the atmosphere., *Tech. Rep. AD0702162*, Mount Auburn Research Associates, Inc.
- Landau, L. D., and E. M. Lifshitz (1987), *Fluid Mechanics*, 2 ed., Pergamon Press.
- Langston, C. A. (2004), Seismic ground motions from a bolide shock wave, *Journal of Geophysical Research*, 109(B12309).
- Leighton, T., and A. Petculescu (2008), Sounds in space: The potential uses for acoustics in the exploration of other worlds, *Hydroacoustics*, 11, 225–239.
- Leslie, F. W., and C. G. Justus (2011), The NASA Marshall Space Flight Center Earth Global Reference Atmospheric Model - 2010 Version, *Tech. Rep. NASA/TM-2011-216467*, National Aeronautics and Space Administration.
- LeVeque, R. J. (2002), *Finite Volume Methods for Hyperbolic Problems*, Cambridge Texts in Applied Mathematics, Cambridge University Press.
- LeVeque, R. J. (2007), *Finite Difference Methods for Ordinary and Partial Differential Equations*, Society for Industrial and Applied Mathematics.
- Li, J. Z., Z. Q. Bai, W. S. Chen, Y. Q. Xia, Y. R. Liu, and Z. Q. Ren (2003), Strong earthquakes can be predicted: a multidisciplinary method for strong earthquake prediction, *Natural Hazards and Earth System Science*, 3(6), 703–712.
- Lin, T.-L., and C. A. Langston (2007), Infrasound from thunder: A natural seismic source, *Geophysical Research Letters*, 34(L14304).
- Lissauer, J. J., and I. de Pater (2013), *Fundamental Planetary Science*, Cambridge University Press.
- Lorenz, R. D. (2012), Planetary seismology - expectations for lander and wind noise with application to venus, *Planetary and Space Science*, 62(1), 86–96.

- Medvedev, A. S., and E. Yigit (2012), Thermal effects of internal gravity waves in the martian upper atmosphere, *Geophysical Research Letters*, 39(L05201).
- Mueller-Wodarg, I. C. F., D. F. Strobel, J. I. Moses, J. H. Waite, J. Crovisier, R. V. Yelle, S. W. Bougher, and R. G. Roble (2008), Neutral atmospheres, *Space Science Reviews*, 139(1-4), 191–234.
- Mutschlecner, J. P., and R. W. Whitaker (2005), Infrasound from earthquakes, *Journal of Geophysical Research*, 110(D01108).
- NASA Goddard Spaceflight Center (2016), OMNIWeb - Space Physics Data Facility, <http://omniweb.gsfc.nasa.gov/form/dx1.html>.
- National Aeronautics and Space Administration (1972), Earth in Full View, https://www.nasa.gov/mission_pages/apollo/images.html.
- National Aeronautics and Space Administration (2003), NASA's Hubble Space Telescope Close-up of the Red Planet, Mars, https://www.nasa.gov/mission_pages/hubble/multimedia/index.html.
- National Space Science Data Center (1979), Pioneering Venus, <http://solarsystem.nasa.gov/galleries/pioneering-venus>.
- Nave, C. R. (2008), The Environment of Venus - Hyperphysics, <http://hyperphysics.phy-astr.gsu.edu/hbase/Solar/venusenv.html>.
- Pasko, V. P. (2009), Mechanism of lightning-associated infrasonic pulses from thunderclouds, *Journal of Geophysical Research*, 114(D08205).
- Pätzold, M., B. Häusler, M. K. Bird, S. Tellmann, R. Mattei, S. W. Asmar, V. Dehant, W. Eidel, T. Imamura, R. A. Simpson, et al. (2007), The structure of venus' middle atmosphere and ionosphere, *Nature*, 450(7170), 657–660.
- Petculescu, A., and R. M. Lueptow (2006), Atmospheric acoustics of titan, mars, venus, and earth, *Icarus*, 186(2), 413–419.

- Pickhershgill, A. O., and G. E. Hunt (1981), An examination of the formation of linear lee waves generated by giant martian volcanoes, *Journal of Atmospheric Sciences*, *38*, 40–51.
- Picone, J. M., A. E. Hedin, D. P. Drob, and A. C. Aikin (2002), NRLMSISE-00 empirical model of the atmosphere: Statistical comparisons and scientific issues, *Journal of Geophysical Research*, *107*(A12), 1468.
- Potter, D. E. (1973), *Computational Physics*, John Wiley and Sons, Inc.
- Prinn, R. G., and B. Fegley (1987), The atmospheres of venus, earth, and mars—a critical comparison, *Annual Review of Earth and Planetary Sciences*, *15*, 171–212.
- Russell, C. T., R. N. Clayton, P. R. Buseck, X. Hua, K. A. Holsapple, L. W. Esposito, T. J. Aherns, and J. Hecht (1993), Planetary lightning, *Annual Review of Earth and Planetary Sciences*, *21*, 43–87.
- Salby, M. L. (1996), *Fundamentals of Atmospheric Physics*, International Geophysics Series, Academic Press.
- Schecter, D. A. (2012), In search of discernible infrasound emitted by numerically simulated tornadoes, *Dynamics of Atmospheres and Oceans*, *57*, 27–44.
- Schlatter, T. W. (2009), Atmospheric composition and vertical structure, *Tech. Rep. eae31MS*, National Oceanic and Atmospheric Administration, Boulder, CO.
- Schroeder, L. B., C. J. Heale, and J. B. Snively (2013), Adaptation and Validation of an Atmospheric Model to Simulate Acoustic and Gravity Waves in the Martian MLT, poster presented at CEDAR (Coupling, Energetics, and Dynamics of Atmospheric Regions) Workshop; Boulder, CO United States.
- Snively, J. B. (2003), Tropospheric forcing as a source of quasi-monochromatic short-period gravity waves observed in the upper mesosphere and lower thermosphere, Master's thesis, The Pennsylvania State University.

- Snively, J. B. (2014), EP 711: Computational Atmospheric Dynamics, course lecture at Embry-Riddle Aeronautical University, Fall 2014; Daytona Beach, FL United States.
- Snively, J. B., and V. P. Pasko (2008), Excitation of ducted gravity waves in the lower thermosphere by tropospheric sources, *Journal of Geophysical Research*, *113*(A06303).
- Song, Y., Y. Zhang, C. Zhou, and Z. Zhao (2014), Acoustic ray tracing in the atmosphere: with gravitational effect and attenuation considered, *Annals of Geophysics*, *57*(5), A0542.
- Stevenson, D. J., J. A. Cutts, D. Mimoun, S. Arrowsmith, W. B. Banerdt, P. Blom, E. Brageot, Q. Brissaud, G. Chin, P. Gao, et al. (2015), Probing the interior structure of venus, *Tech. rep.*, Keck Institute for Space Studies.
- Strobel, D. F. (2002), Aeronomic systems on planets, moons, and comets, in *Atmospheres in the Solar System: Comparative Aeronomy, Geophysical Monograph Series*, vol. 130, edited by M. Mendillo, A. F. Nagy, and J. H. Waite, pp. 7–22, AGU.
- Tanaka, T., T. Ichinose, T. Okuzawa, T. Shibata, Y. Sato, C. Nagasawa, and T. Ogawa (1984), Hf-doppler observations of acoustic waves excited by the urakawa-oki earthquake on 21 march 1982, *Journal of Atmospheric and Terrestrial Physics*, *46*(3), 233–245.
- Taylor, F. W. (2010), *Planetary Atmospheres*, Oxford University Press.
- Tratt, D. M., M. H. Hecht, D. C. Catling, E. C. Samulon, and P. H. Smith (2003), In situ measurement of dust devil dynamics: Toward a strategy for mars, *Journal of Geophysical Research*, *108*(E11), 5116.
- Walterscheid, R. L., and M. P. Hickey (2005), Acoustic waves generated by gusty flow over hilly terrain, *Journal of Geophysical Research*, *110*(A10307).

- Walterscheid, R. L., G. Schubert, and D. G. Brinkman (2003), Acoustic waves in the upper mesosphere and lower thermosphere generated by deep tropical convection, *Journal of Geophysical Research*, *108*(A11), 1392.
- Williams, J.-P. (2001), Acoustic environment of the martian surface, *Journal of Geophysical Research*, *106*(E3), 5033–5041.
- Williams, M. (2016), How long is a day on the other planets of the solar system?, *Universe Today*.
- Zettergren, M., and J. Semeter (2012), Ionospheric plasma transport and loss in auroral downward current regions, *Journal of Geophysical Research*, *117*(A06306).
- Zettergren, M. D., and J. B. Snively (2015), Ionospheric response to infrasonic-acoustic waves generated by natural hazard events, *Journal of Geophysical Research*, *120*(9), 8002–8024.

Appendix A

SIMULATION STRUCTURE

A.1 Building the Model

For a Linux bash shell or Macintosh operating system, the model may be built by simply executing the build script from the top-level directory, as shown in Figure A.1. This script unzips the GRAM data files, executes a makefile for the Fortran model as well as each of the empirical models, and then appends the run alias to the user's environment. For easy recompilation, the build script may be specified at the command line to build only one of the specific models or re-configure the environment without recompilation of the entire model.

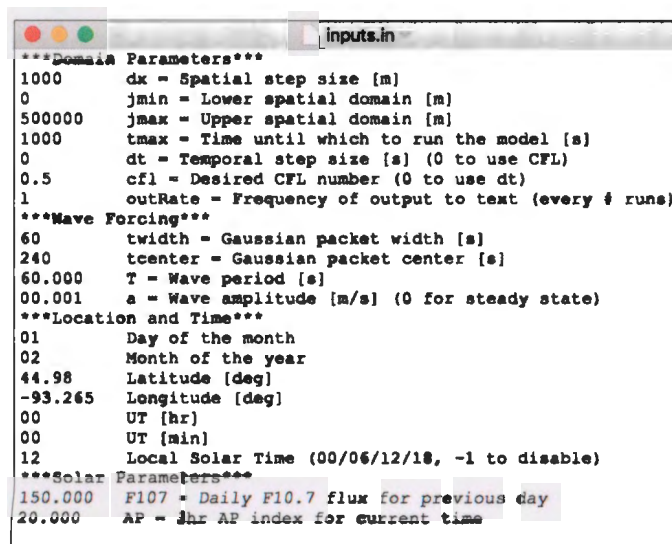
```
$ ./build
Building Model...
gfortran -fw -x86_64-linux-gnu-gcc -fcommon -ftricky -fno-automatic
  building MIPS
gfortran -fw model_MIPS_driver.f90 -x86_64-linux-gnu-gcc -fcommon -ftricky -fno-automatic
  building EarthGRAM
gfortran -fw model_EarthGRAM_driver.f90 -x86_64-linux-gnu-gcc -fcommon -ftricky -fno-automatic -I../lib -I../model_EarthGRAM/Inlets_E10_I100 -fw model_EarthGRAM/program
b1_E10.f90 -fw model_EarthGRAM/MARSsubs_E10.f90 -fw model_EarthGRAM/Inlets_E10_I100 -fw model_EarthGRAM/RET07.f90 -fw model_EarthGRAM/ing
d_In_E10.f90 -fw model_EarthGRAM/program_E10.f90 -fw model_EarthGRAM/specare.f90 -fw model_EarthGRAM/RTS_Libs_E20.f90 -fw model_EarthGRAM/is
code_L10.f90 -fw model_EarthGRAM/Inlets_E10_I100 -fw EarthGRAM
  building MarsGRAM
gfortran -fw model_MarsGRAM_driver.f90 -x86_64-linux-gnu-gcc -fcommon -ftricky -fno-automatic -I../lib -I../model_MarsGRAM/Inlets_M10_I100 -fw model_MarsGRAM/program
b1_M10.f90 -fw model_MarsGRAM/setup_MARS.f90 -fw model_MarsGRAM/TLSubs_M10.f90 -fw model_MarsGRAM
  building VenusGRAM
gfortran -fw model_VenusGRAM_driver.f90 -x86_64-linux-gnu-gcc -fcommon -ftricky -fno-automatic -I../lib -I../model_VenusGRAM/Venussubs_V15.f90 -fw model_VenusGRAM/Inlets_V15_I100 -fw model_VenusGRAM
  *** BUILD COMPLETED SUCCESSFULLY ***
$
```

Figure A.1: Command line output from building the model.

A.2 Running the Model

A.2.1 Input File

The model is primarily driven by a text input file that allows the user to specify key parameters of the run, shown in Figure A.2.



```
***Domain Parameters***
1000    dx = Spatial step size [m]
0      jmin = Lower spatial domain [m]
500000 jmax = Upper spatial domain [m]
1000   tmax = Time until which to run the model [s]
0      dt = Temporal step size [s] (0 to use CFL)
0.5    cfl = Desired CFL number (0 to use dt)
1      outRate = Frequency of output to text (every # runs)
***Wave Forcing***
60     twidth = Gaussian packet width [s]
240    tcenter = Gaussian packet center [s]
60.000 T = Wave period [s]
00.001 a = Wave amplitude [m/s] (0 for steady state)
***Location and Time***
01     Day of the month
02     Month of the year
44.98  Latitude [deg]
-93.265 Longitude [deg]
00     UT [hr]
00     UT [min]
12     Local Solar Time (00/06/12/18, -1 to disable)
***Solar Parameters***
150.000 F10.7 = Daily F10.7 flux for previous day
20.000  AP = Jhr AP index for current time
```

Figure A.2: Model input file.

A.2.2 Python Wrapper

A Python wrapper was developed to provide maximum flexibility to the user of the model. This wrapper accepts several runtime inputs at the command line in order to control the model execution, and then proceeds to (1) perform random draws on variables (if desired), (2) call the appropriate empirical model to generate a profile, (3) call the acoustics model, and (4) store the output files in a user-specified output directory.

The greatest benefit of the Python wrapper is the ability to specify a batch run queue, which directs the model to automatically run any number of scenarios one after the other based on a comma-delimited queue file (as shown in Figure A.3). In the queue file the user may specify amplitude, period, month, latitude, longitude, hour

	A	B	C	D	E	F	G	H	I	J	K	L	M	N	O	P	Q
1	amp	ampsD	per	perSD	month	monthSD	lat	latSD	lon	lonSD	hour	hoursD	LST	F107	F107SD	AP	APSD
2	1.00E-03	0	60	0	1	0	44.98	0	-93.265	0	0	0	0	150	0	20	0
3	1.00E-03	0	60	0	2	0	44.98	0	-93.265	0	0	0	0	150	0	20	0
4	1.00E-03	0	60	0	3	0	44.98	0	-93.265	0	0	0	0	150	0	20	0
5	1.00E-03	0	60	0	4	0	44.98	0	-93.265	0	0	0	0	150	0	20	0
6	1.00E-03	0	60	0	5	0	44.98	0	-93.265	0	0	0	0	150	0	20	0
7	1.00E-03	0	60	0	6	0	44.98	0	-93.265	0	0	0	0	150	0	20	0
8	1.00E-03	0	60	0	7	0	44.98	0	-93.265	0	0	0	0	150	0	20	0
9	1.00E-03	0	60	0	8	0	44.98	0	-93.265	0	0	0	0	150	0	20	0
10	1.00E-03	0	60	0	9	0	44.98	0	-93.265	0	0	0	0	150	0	20	0
11	1.00E-03	0	60	0	10	0	44.98	0	-93.265	0	0	0	0	150	0	20	0
12	1.00E-03	0	60	0	11	0	44.98	0	-93.265	0	0	0	0	150	0	20	0
13	1.00E-03	0	60	0	12	0	44.98	0	-93.265	0	0	0	0	150	0	20	0
14	1.00E-03	0	60	0	1	0	44.98	0	-93.265	0	0	0	6	150	0	20	0
15	1.00E-03	0	60	0	2	0	44.98	0	-93.265	0	0	0	6	150	0	20	0
16	1.00E-03	0	60	0	3	0	44.98	0	-93.265	0	0	0	6	150	0	20	0
17	1.00E-03	0	60	0	4	0	44.98	0	-93.265	0	0	0	6	150	0	20	0
18	1.00E-03	0	60	0	5	0	44.98	0	-93.265	0	0	0	6	150	0	20	0
19	1.00E-03	0	60	0	6	0	44.98	0	-93.265	0	0	0	6	150	0	20	0
20	1.00E-03	0	60	0	7	0	44.98	0	-93.265	0	0	0	6	150	0	20	0
21	1.00E-03	0	60	0	8	0	44.98	0	-93.265	0	0	0	6	150	0	20	0
22	1.00E-03	0	60	0	9	0	44.98	0	-93.265	0	0	0	6	150	0	20	0
23	1.00E-03	0	60	0	10	0	44.98	0	-93.265	0	0	0	6	150	0	20	0
24	1.00E-03	0	60	0	11	0	44.98	0	-93.265	0	0	0	6	150	0	20	0
25	1.00E-03	0	60	0	12	0	44.98	0	-93.265	0	0	0	6	150	0	20	0

Figure A.3: Example queue.csv file, which sets up a batch of 24 runs varying month and Local Standard Time. This batch does not specify any random draws.

in UT or LST, F10.7, and solar AP index, as well as a standard deviation for each of the variables. If a standard deviation is given, the parameter is randomly drawn from a normal distribution with the specified value at the center and the indicated standard deviation.

The available command line arguments are as follows:

- -p<e/m/v> OR --planet=<earth/mars/venus>
- -i for isothermal instead of empirical profile
- -o to specify output directory name
- -e for explicit Euler method instead of implicit
- -q (quiet) to disable screen output
- -w for continuous wave instead of packet
- -f to specify queue file (queue.csv is default)

- -r n:m for batch runs n through m
- --noMATLAB to disable automatic data export to a MATLAB[®] structure
- --profile to only generate profiles and skip the acoustic runs
- --msis to use NRLMSISE-00 instead of EarthGRAM2010
- --horiz to enable horizontal wave propagation at a specific altitude

Example runs are shown in Figures A.4 and A.5.

A.3 Model Source

A.3.1 Fortran Model

The primary source code of the one-dimensional atmospheric acoustics model is contained within two Fortran files. The first reads the inputs and atmospheric profiles, performs the advection and diffusion calculations, and outputs results to text files (and the screen, if desired). The second Fortran file contains a tridiagonal matrix solver subroutine used to calculate implicit diffusion.

A.3.2 Empirical Models

In order to obtain accurate atmospheric profiles, the Fortran model reads data output by an empirical atmosphere model. For this thesis the Global Reference Atmospheric Model (GRAM) [*Justh et al.*, 2006] packages by the NASA Marshall Spaceflight Center are utilized; these are EarthGRAM 2010, MarsGRAM 2010, and VenusGRAM 2005. The models have undergone slight modifications in order to support the specific format of input and output required by the Fortran model. These models have been obtained from NASA for the purpose of this research, and may not be re-distributed without specific authorization. The Naval Research Laboratory Mass Spectrometer Incoherent Scatter Radar Extended 2000 (NRLMSISE-00) model [*Picone et al.*, 2002] is optionally available as a substitute for EarthGRAM.

```

$ run -pe r4:5 -f queueGlobe.csv -o Example -q
----- PLANETARY ATMOSPHERIC ACOUSTICS MODEL -----
- Empirical profile ENABLED
- Wave Packet ENABLED
- Implicit Euler diffusion scheme ENABLED
- Data will be output to Output/Example
- Terminal Output DISABLED
- Planet: EARTH

Running the model 2 times...

Running EarthGRAM 2010...
Finished generating profile. Performing calculations...
Completed Run 4 in 5.01 s
Average Run Time: 5.01 s

Running EarthGRAM 2010...
Finished generating profile. Performing calculations...
Completed Run 5 in 5.01 s
Average Run Time: 4.99 s

-----
Completed 2 runs.
Output located in 'Output/Example/Earth'
$
    
```

Figure A.4: Example model run, in which runs 4 and 5 from the *queueGlobe.csv* batch file are executed on Earth and output to a directory called *Example*. In this example terminal output is disabled with the *-q* flag.

```

$ run -m -w
----- PLANETARY ATMOSPHERIC ACOUSTICS MODEL -----
- Empirical profile ENABLED
- Wave Packet DISABLED ...continuous forcing selected
- Implicit Euler diffusion scheme ENABLED
- Planet: MARS

Running the model 1 times...

Running MarsGRAM 2010...
Finished generating profile. Performing calculations...

r= 1 n= 1 t= 1.99009 cfl= 0.500 planet= Mars
r= 1 n= 5 t= 9.95045 cfl= 0.500 planet= Mars
r= 1 n= 10 t= 19.90091 cfl= 0.500 planet= Mars
Completed Run 1 in 0.56 s
Average Run Time: 0.56 s

-----
Completed 1 runs.
Output located in 'Output/Mars'
$
    
```

Figure A.5: Example model run, in which a wave is continuously forced for twenty seconds on Mars.

A.4 Output

The model outputs to text, which is read by a MATLAB[®] script *LoadOutput* and converted to a .mat data file, which can be re-loaded at any time without having to parse the text output file(s). This is especially useful for large run batches. Several MATLAB[®] scripts have been developed in order to plot model output as well as profiles from the GRAM empirical models.

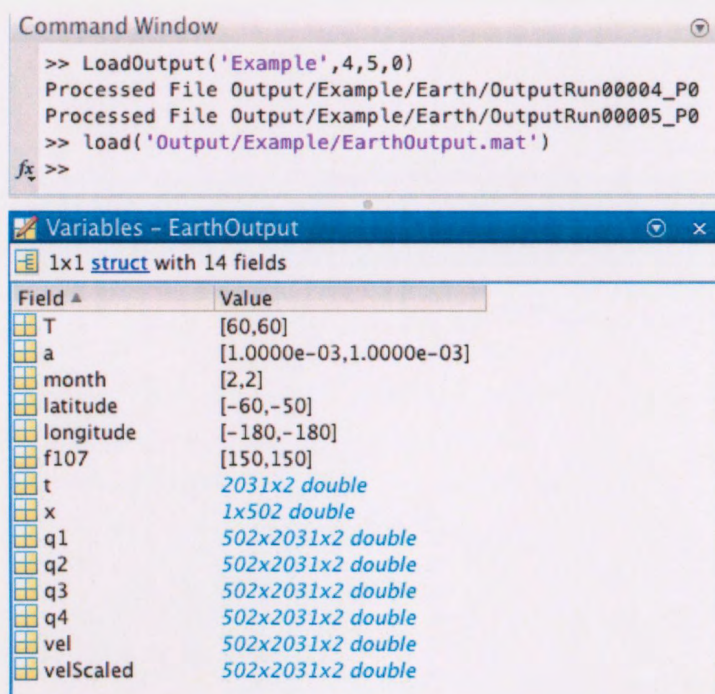


Figure A.6: MATLAB[®] function loading data from the runs generated in Figure A.4. The output directory is specified along with the first and last runs and planet: 0 for Earth, 1 for Mars, and 2 for Venus.

The profile is loaded by the *LoadProfile* function and stored in a separate structure. In addition to loading, the *LoadProfile* function calculates many derived quantities (e.g., viscosity, speed of sound, molecular weight, etc.) from the profile output and stores them in the structure as well. Like with the model output, these are output to a .mat file for each planet.